Theoretical Understanding and Material Design towards Next-generation Data Storage Devices

ZHAOQIANG BAI

(B.Sc., Chongqing University)

A THESIS SUBMITTED

FOR THE DEGREE OF DOCTOR OF PHILOSOPHY

DEPARTMENT OF PHYSICS

NATIONAL UNIVERSITY OF SINGAPORE

2014

DECLARATION

I hereby declare that this thesis is my original work and it has been written by me in its entirety. I have duly acknowledged all the sources of information which have been used in the thesis.

This thesis has also not been submitted for any degree in any university previously.

Bai Zhaoqiang

12 August 2014

Acknowledgements

I owe my deepest gratitude to my supervisors, **Prof. Feng Yuan Ping** and **Dr. Han Guchang**, for their professional guidance and advice, unwavering support and patience, and the everlasting encouragement throughout the past years. The wisdom they shared with me is precious treasure which will keep me on track in both my future research career and daily life.

My special thanks go to two of my senior labmates in the Computational Condensed Matter Physics (CCMP) Lab, Dr. Shen Lei and Dr. Cai Yongqing, for their sustained and substantial help ever since the first day I joined the group. The countless number of discussion with them was incomparably instructive, inspiring and fruitful, which sparked many new ideas of my Ph.D work.

I would like to thank Prof. Kristian S. Thygesen and Dr. Troels Markussen for hosting me during my eight-month visit in Technical University of Denmark. From them I learnt not only research skills but also what scientific spirit is.

I express a great thanks to Dr. Sha Zhendong for his step-by-step instruction in many technical issues of the computational softwares and scripts in the early stage of my Ph.D. candidature. It is also a pleasure for me to thank other group members in the CCMP Lab, Dr. Zhou Miao, Dr. Yang Ming, Dr. Zeng Minggang, Dr. Xu Bo, Mr. Wu Qingyun, Ms. Li Suchun, Ms. Chintalapoti Sandhya, Dr. Qin Xian, Ms. Linghu Jiajun, Prof. Li

Dechun, Mr. Zhou Jun, and Ms. Zhang Meini for the enjoyable time we spent together.

I acknowledge National University of Singapore for the research scholarship. Without the financial support I would never have to chance to carry out my PhD research and accomplish this thesis.

Last but not least, I express my deep appreciation to my parents and my sister for their support and love.

Zhaoqiang Bai

Table of Contents

Summary

Magnetic data storage has been an active and productive research field for several decades. Targeted on the everlasting persuit of higher storage capacity, longer data retention, and lower energy consumption, it spans both computational and experimental efforts. The theoretical understanding of the underlying physical mechanism, i.e., the giant magnetoresistance and tunneling magnetoresistance effects, by means of first-principles calculation, stands among the essential issues which provides guidance and insights into the device optimization in practice. In addition, the computational screening and design of novel materials and heterostructures as the building blocks of data storage devices has proved to be a highly efficient and economic way. In this thesis, first-principles approaches based on various computational techniques were employed to illustrate and discuss the subject of magnetic data storage, to explore and unveil the physics dominating the device performance, and to find novel and practical methodologies of designing promising functional elements for the next-generation data storage devices.

The current-perpendicular-to-plane giant magnetoresistance (CPP-GMR) devices hold the promise for substituting the magnetic tunnel junctions (MTJs) as the next-generation hard disk drive (HDD) read sensors. Our first proposal in this thesis is an all-Heusler trilayer architecture which could be used as a rational design scheme for achieving high

spin-filter efficiency in the CPP-GMR devices. Quantum transport calculation showed remarkable improvement in the magnetotransport performance over the conventional Heusler-compound/transition-metal/Heusler-compound design by employing an all-Heulser $Co_2CrSi/Cu_2CrAl/Co_2CrSi$ GMR stack. Subsequently, the underlying physics was unveiled via a more comprehensive electronic-structure and spin-transport study. The intrinsically matched energy bands and Fermi surfaces between the all-Heusler electrode-spacer pair gives rise to small interfacial resistances of parallel conduction electrons and hence enhances the MR ratio.

In parallel to GMR, the tunneling magnetoresistance effect (TMR) may be of greater importance in view of its mainstream status in the present magnetic recording devices and the bright prospects for the next-generation memory techniques. From historical point of view, every crucial progress in the theoretical understanding of the TMR effects boosted the improvement of the TMR devices. However, there exists a long-standing problem that, albeit continuous optimization of the fabrication process and technique, the magnetoresistance ratio obtained in experiments is always much lower than the theoretical predictions. Our theoretical investigation attributed this discrepancy to the boron-diffusion induced crystal symmetry reduction of the MgO tunneling barrier, which is inevitable in the current experimental fabrication process. We also found that the MR performance is highly sensitive to the interface quality, and boron residuals at the electrode/barrier interface due to inadequate annealing further decreases the MR value. The new physics we proposed here not only contributes to the theoretical understanding the TMR effects but also provides some hints to the experiment community for the enhancement of MR ratio.

In addition to the theoretical study of the TMR effect, this thesis also sheds some light on

its possible application in a cutting-edge nonvolatile memory, that is, the spin-transfer-torque magnetic random access memory (STT-MRAM). In particular, we carried out first-principles calculation to predict and design ferromagnetic materials/heterostructures for the construction of high-performance perpendicular magnetic tunnel junctions (p-MTJs), which are incorporated in STT-MRAMs as storage bits. A crucial step towards the goal is to identify ferromagnetic materials with perpendicular easy axes to serve as the p-MTJ electrodes. We address this problem by evaluating the suitability of the recently emerged binary compound series $Mn_{3-x}Ga$ ($0 \leq x \leq 1$). Our calculation showed that, due to the symmetry selective filtering effect, only $Mn_{3-x}Ga$ with low Mn concentration ($x \to 1$) are eligible in view of magnetoresistance performance.

On the way to search for high-performance p-MTJ building blocks, we also explored the heterostructure containing half-metallic Heusler compounds in junction with the MgO barrier. The Co_2FeAl (CFA) /MgO interface was chosen as a prototype, of which the thermodynamic stability, magnetocrystalline anisotropy, magnetoelectric effect and magnetotransport performance were systematically investigated. It was found that the geometry of the interface is extremely robust with only one possible interfacial configuration, i.e., the oxygen-top FeAl termination, protected by the thermodynamic equilibrium limit. Further investigation revealed that the interface possesses a perpendicular easy axis, and moreover, its magnetocrystalline anisotropy can be efficiently tuned by external electric field. In addition, the intrinsic half-metallic feature of CFA also promises good magnetoresistance performance of the whole junction. Our finding suggested the CFA/MgO/CFA p-MTJ as a promising building block for the next-generation nonvolatile memories with high recording stability and low power consumption.

Publications

BOOK CHAPTER:

[1] L. Shen, M. G. Zeng, Q. Y. Wu, **Z. Q. Bai**, and Y. P. Feng, "Graphene spintronics: spin generation and manipulation in graphene", in Graphene optoelectronics. Synthesis, characterization, properties and applications, edited by Abd. Rashid bin Mohd Yussof, WILEY-VCH Verlag (2013).

Review ARTICLE:

[1] **Z. Q. Bai**, L. Shen, G. C. Han, and Y. P. Feng, "Data storage: Review of Heusler compounds", SPIN **2**, 1230006 (2013).

RESEARCH PAPERS:

[1] **Z. Q. Bai**, Y. Q. Cai, L. Shen, M. Yang, V. Ko, G. C. Han, and Y. P. Feng, "Magnetic and transport properties of $Mn_{3-x}Ga$/MgO/$Mn_{3-x}Ga$ magnetic tunnel junctions: A first-principles study", Appl. Phys. Lett. **100**, 022408 (2012). (Also highlighted by the January 23, 2012 issue of Virtual Journal of Nanoscale Science & Technology).

[2] L. Shen, T. J. Zhou, **Z. Q. Bai**, M. G. Zeng, J. Q. Goh, Z.-M. Yuan, G. C. Han, B. Liu, and Y. P. Feng, "Systematic study of ferroelectric, interfacial, oxidative, and doping

effects on conductance of Pt/$BaTiO_3$/Pt ferroelectic tunnel junctions", Phys. Rev. B **85**, 064105 (2012).

[3] **Z. Q. Bai**, Y. H. Lu, L. Shen, V. Ko, G. C. Han, and Y. P. Feng, "Transport properties of high-performance all-Heusler $Co_2CrSi/Cu_2CrAl/Co_2CrSi$ giant magnetoresistance device", J. Appl. Phys. **111**, 093911 (2012).

[4] Y. Q. Cai, **Z. Q. Bai**, M. Yang, and Y. P. Feng, "Effect of interfacial strain on spin injection and spin polarization of $Co_2CrAl/NaNbO_3/Co_2CrAl$ magnetic tunneling junction", Europhys. Lett. **99**, 37001 (2012).

[5] D. C. Li, M. Yang, S. Z. Zhao, Y. Q. Cai, Y. H. Lu, **Z. Q. Bai**, and Y. P. Feng, "First-principles study of the effect of Bi-Ga heteroantisites in GaAs:Bi alloy", Comp. Mater. Sci. **63**, 178 (2012).

[6] **Z. Q. Bai**, L. Shen, Q. Y. Wu, M. G. Zeng, J.-S. Wang, G. C. Han, and Y. P. Feng, "Boron diffusion induced symmetry reduction and scattering in CoFeB/MgO/CoFeB magnetic tunnel junctions", Phys. Rev. B **87**, 014114 (2013).

[7] **Z. Q. Bai**, Y. Q. Cai, G. C. Han, and Y. P. Feng, "High-performance giant-magnetoresistance junctions based on the all-Heusler architecture with matched energy bands and Fermi surfaces", Appl. Phys. Lett. **102**, 152403 (2013).

[8] Y. Q. Cai, **Z. Q. Bai**, S. Chintalapati, Q. F. Zeng, and Y. P. Feng, "Transition metal atoms pathways on rutile TiO2 (110) surface: Distribution of Ti^{3+} states and evidence of enhanced peripheral charge accumulation", J. Chem. Phys. **138**, 154711 (2013).

[9] M. Zhou, Z. Liu, Z. F. Wang, **Z. Q. Bai**, Y. P. Feng, M. X. Lagally, and F. Liu, "Strain engineered surface transport in Si(001): complete isolation of the surface state

via tensile strain", Phys. Rev. Lett. **111**, 246803 (2013).

[10] Y. Q. Cai, **Z. Q. Bai**, H. Pan, Y. P. Feng, Boris I. Yakobson, and Y.-W. Zhang, "Constructing metallic nanoroad on MoS_2 monolayer via hydrogenation", Nanoscale, published online (2014)

[11] **Z. Q. Bai**, L. Shen, Y. Q. Cai, Q. Y. Wu, M. G. Zeng, G. C. Han, and Y. P. Feng, "Thermodynamic stability, electric-field control of magnetization, and non-collinear spin transport of Heusler-compound based perpendicular magnetic tunnel junctions ", submitted. arXiv:1303.3473v2.

[12] **Z. Q. Bai**, T. Markussen, Yuan Ping Feng, and K. S. Thygesen, "Electron transport across a metal/MoS_2 interface: dependence on contact area and binding distance", submitted.

[13] Q. Y. Wu, L. Shen, **Z. Q. Bai**, M. G. Zeng, M. Yang, Y. P. Feng and Z. G. Huang, "Efficient spin injection into graphene: overcoming the spin conductance mismatch by boron nitride tunneling barrier", submitted.

[14] Q. Y. Wu, L. Shen, **Z. Q. Bai**, M. G. Zeng, M. Yang, Y. P. Feng and Z. G. Huang, "Electronic and transport properties of monolayer MoS2/metal junctions: a systematic first-principles investigation", submitted.

[15] **Z. Q. Bai**, L. Shen, Y. Q. Cai, G. C. Han, and Y. P. Feng, "High-performance quaternary-Heusler compounds based magnetic tunnel junctions", in preparation.

List of Tables

List of Figures

Chapter 1

Introduction

The past decades has witnessed drastic information explosion, i.e., the monstrous growth of data created as a by-product of business and individual activities. The amount of digital information in the world continues to grow at an astonishing rate, doubling every two years and reaching 2.8 zettabytes (ZBs) -that is, 2.8 followed by 21 zeros- in 2012.[1] It is estimated that by 2020 the digital information created and replicated would increase to more than 20 ZBs. Associated with the data flood is the timely requirement for continuous innovation in data storage devices, aiming at both creation of sufficient recording space and fast access and manipulation of data.

Data storage devices are devices for recording information, which, in general, can be realized using virtually any form of energy, spanning from manual muscle power in handwriting, over acoustic vibrations in phonographic recording, to electromagnetic energy modulating magnetic and optic discs. Nowadays, mainstream massive recording techniques fall into the category of magnetic storage, that is, the storage of data on a

magnetized medium. Magnetic storage uses different orientations of magnetization in a magnetizable material to store bit information, which is accessed using one or more read/write heads. The most economical and hence most popular magnetic storage device is the magnetic hard disk drive (HDD), a manufactured miracle which enables the cost of storage per gigabyte (GB) to go down by half every 14 months over the past 30 years ($437,500/GB in 1980 down to $0.05/GB in 2013).[2]

Albeit the massive increase in capacity and decrease in cost, the access speed, i.e., the rate at which data can be read from and write in the drives, has not kept up due to the intrinsic mechanical characteristic of the HDD. In addition, the requirements of non-volatility and long data duration are also essential for the next-generation data storage devices. As a supplement to the HDD, an idea of non-volatile magnetic storage, the magnetic random access memory (MRAM), has emerged in the very recent years with the key features of fast access and long data duration. The combination of HDD and M-RAM is even proposed to be the new storage hierarchy for the next-generation computer memories.

The aforementioned unlimited increase in data amount has spurred endless development in magnetic data storage devices towards even higher capacity, higher access speed and longer data duration. Such development presents new opportunities for both theoretical and experimental search for new materials and new physics. In the following section, the trend in the development of magnetic data storage devices will be elucidated.

1.1 The evolution of magnetic data storage and its future development

1.1.1 Current-perpendicular-to-plane giant magnetoresistance and read heads of hard disk drives

One of the most commonly used magnetic data storage devices is the HDD, of which significant boost in the development originated from the discovery of the giant magnetoresistance (GMR) by Fert and Grünberg (2007 Nobel Prize in Physics) in 1988.[3, 4] The GMR, by providing a sensitive and scalable read technique, has led to an increase of the HDD areal recording density by more than two orders of magnitude (from $\sim$ 1 to $\sim$ 600 gigabits/inch^2 in 2007).[5, 6] In the early 1990s, the demonstration of GMR effect and oscillation behavior with respect to the thickness of non-magnetic (NM) layers was reported in the metallic superlattice systems Co/Cr, Co/Ru[7] and Co/Cu[8, 9], using the economical sputtering technique. Subsequently, GMR was observed for the first time in a trilayer spin-valve (SV) structure, composed of two ($Ni_{81}Fe_{19}$, $Ni_{80}Co_{20}$, Ni) ferromagnetic (FM) electrodes separated by (Cu, Ag, Au) NM spacers.[10] In 1997, current-in-plane (CIP) GMR sensors with spin-valve geometry were commercialized by IBM as HDD read heads, replacing the previous anisotropic magnetoresistance (AMR) technique. However, the planer geometry of the CIP SV sensors intrinsically limits further dimensional downscaling of the HDD read heads, and therefore, prevents higher storage density. In order to overcome this problem, a current-perpendicular-to-plane (CPP) configuration of GMR SVs was recently proposed as a promising architecture due to its geometrical compatibility with the shape of the read head track. Nonetheless, the

problem with the present CPP-GMR sensors is the low GMR ratio, which hinders their practical application. [11, 12]

1.1.2 Tuneling magnetoresistance and magnetic random access memories

Another big progress in spintronics related to data storage is the invention of the magnetic tunnel junction (MTJ), which is also a trilayer stack composed of two FM layers sandwiching a NM insulator instead of metal. The story of the MTJ development began in the mid-1970s, when Julliere reported the observation of a small MR effect from a Fe/Ge/Co MTJ structure at low temperature.[13] However, the realization of remarkable and reproducible tunneling magnetoresistance (TMR) effect had not been achieved until 1995, when the MTJ structure containing amorphous Al_2O_3 spacer was reported with a relatively large MR ratio $\sim$70% at room temperature (RT).[14, 15] The technical development of MTJ elements has been initialized and accompanied by the evolving physical understanding of TMR. A remarkable example was the theoretical prediction of large TMR ratio with a single-crystal MgO barrier, which claimed that, rather than the simple barrier model, the electron tunneling behavior of MgO-based MTJs is determined by the spin-dependent symmetry coupling of the transmission Bloch states between the ferromagnetic (FM) electrodes and the nonmagnetic (NM) MgO spacer.[16–18] This prediction led to subsequent experimental efforts and breakthrough in the MgO-based MTJ with huge TMR ratio $\sim$ 200% at room temperature (RT).[19, 20] In the recent years, the TMR effect was largely enhanced by the improved experimental techniques.[21] Currently, MTJs are widely used in the HDD read heads. They are also proposed to be

integrated into a novel nonvolatile memory, namely, the magnetic random access memory(MRAM).

MRAM has the basic “cross point” architecture, in which the binary information is recorded on the two opposite magnetization orientations of the free layer of the arrayed MTJs. It claimed by its proponents to possess overwhelming advantages (non-volatility, fast access and unlimited duration) over the current mainstream solid-state drive (SSD) memories, such as static random-access memory (SRAM), dynamic random-access memory (DRAM) and Flash,[22] and would even become dominant over all types of data storage techniques as a “universal memory ”.[23] In reality, the first MRAM product, a 4-Mbit stand-along toggle memory, was commercialized in 2006 by Freescale.[24, 25] However, the current toggle MRAM may not be expected to scale well to small dimensions due to the intrinsic requirement of large write currents in the way of Oersted-field flipping. Such poor writability limits the number of elements that can be arrayed and degrades the layout efficiency of the memory. Moreover, large write currents also increase the power consumption much beyond that of SRAM or DRAM.[26]

1.1.3 Spin-transfer torque magnetic random access memories

The hope of breakthrough for the data writing was provided by the prediction in 1996 by Slonczewski and Berger that, instead of long-range effects mediated by the write current via its Oersted field, the magnetization orientation of a free magnetic layer could be controlled by a local means of manipulation via the transfer of spin angular momentum from a spin-polarized current, or in short, the spin-transfer torque (STT) effect.[27, 28] Specically, a spin-polarized current of s-electrons are generated by transmission through

or reflection from the thick reference layer and most of the electrons maintain this polarization as the current passes through the NM spacer. When the current approaches the thin free layer, however, an s-d exchange interaction occurs, which transfers the angular momentum from the polarized current to the free-layer magnetization, acting as an effective torque. This spin torque can oppose the intrinsic damping of the magnetic layer, reverse the direction of the magnetization and lead to a resistance change. The early experimental verification of the STT effect was made in Co/Cu multilayers[29] and Co/Cu/Co CPP-GMR SV nanopillars,[30–32] whereas the interest was later shifted and focused on the association between STT and MRAM. In the spin-transfer torque random access memory (STT-MRAM), the switching threshold is determined by the injected spin-polarized current density, instead of the current, which makes it possible to ease many of the scaling limitations of the toggle MRAM.[33, 34] Besides, the elimination of the external write line would also lower the power consumption below that of both SRAM and DRAM.[26, 35, 36] Actually, several demonstrations of STT-MRAM have already been presented by industry, which exhibit many aforementioned advantages, making it competitive as a future data-storage technique.[36]

1.2 Literature Review

1.2.1 The application of Heusler compounds in CPP-GMR read heads and the "all-Heusler " design scheme

As mentioned in the previous section, the problem with the present CPP-GMR read heads, which hinders their practical application, is the low GMR ratio. A straightforward method of enhancing the GMR ratio is to use high spin-polarization (SP) materials as ferromagnetic electrodes. Among all the possible materials, the family of Heusler compounds, first discovered by and named after Fritz Heusler in 1903,[39, 40] is widely believed as potential candidates eligible for constructing CPP-GMR and TMR architectures.[41, 42]

The application of Heusler compounds in current-perpendicular-to-plane giant magnetoresistance read heads

Heusler compounds are ternary inter-metallic face-centered cubic (fcc) crystals with the general formula XYZ (often called half-Heusler) or X_2YZ (full-Heusler), in which X and Y are typically transition metals and Z is a main group element. The constituent elements of the Heusler compounds cover almost the whole periodic table, as shown in Fig. 1.1, which provides innumerable members in this family, and hence wide choices for the electronic structure tuning and material design of desirable properties, ranging from half-metallic ferromagnets (HMF),[37, 43] completely compensated ferrimagnets,[44] over non-magnetic semiconductors,[45, 46] to superconductors[47]

and topological insulators.[48–52] A comprehensive description of the Heusler family can be found in Ref. 41. A specific review on the applications of the Heusler compounds in the field of data storage can be found in Ref 53.[53]

Scientific interest in this field was sparked by the theoretical prediction[38, 54] and the subsequent experimental verification[55] of the high Curie temperature (T_c) half-metallicity in the bulk half-Heusler compound MnNiSb in the 1980s, which suggested the possibility of dramatic MR enhancement of the GMR/TMR devices by using the Heusler compounds as electrodes. However, the first MTJ with the MnNiSb epitaxial electrode yielded MR ratios as low as 9% at RT and 18% at low temperature,[56] respectively. This low MR ratio was attributed to the atomic-disorder which led to the diminishing of the half-metallic gap around the Fermi level(E_F).[57] Later on, research interest was shifted to Co-based full-Heusler compounds due to their more stable half-metallicity.[43, 60–66] The early successful demonstration of large MR values in the quaternary $Co_2Cr_{0.6}Fe_{0.4}Si$-based MTJs triggered enormous efforts focusing on the incorporation of the Co-based full Heusler compounds into both GMR and TMR devices,[65, 67] leading to a tremendous increase in the MR ratio during the recent decade.[68, 69] Narrow CPP-GMR read heads, incorporating Heusler materials as reference layers, were successfully tested using a conventional spin-stand system. In this way, the capability of the CPP-GMR technology for ultra-high density magnetic recording has already been demonstrated.[30]

It should be noted that, in addition to the electrode materials, the choice of the spacer layer is also an important issue, since an epitaxial growth of the Heusler thin film on the spacer material is required to form fully epitaxial Heusler/NM spacer/Heusler trilayers. Moreover, according to the Valet and Fert Model for CPP-GMR architecture,[11]

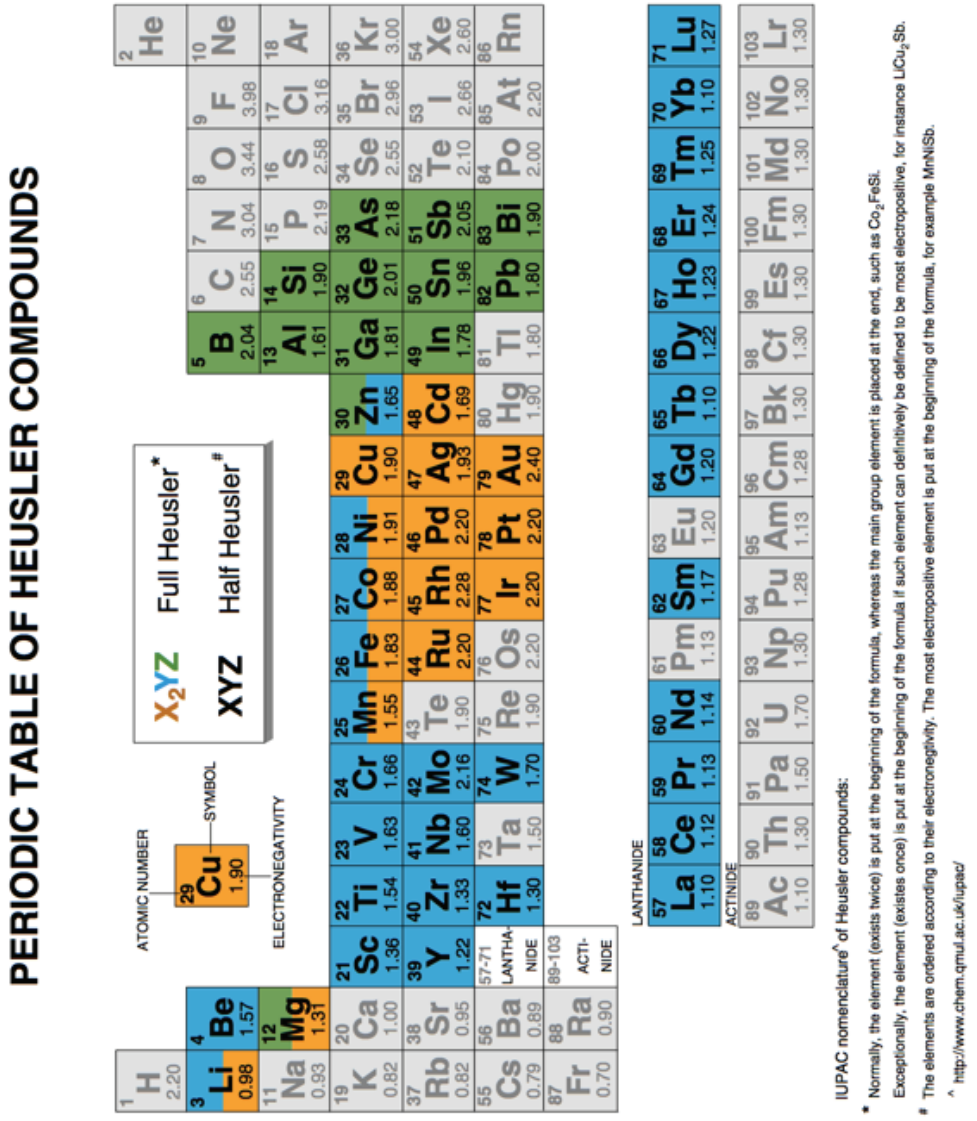

Figure 1.1: Periodic table of Heusler compounds. The huge number of full-Heusler compounds can be formed by combining different elements according to the color scheme. The electronegativity value is given below the element symbol. For half-Heusler compounds XYZ, the elements are ordered according to their electronegativity.

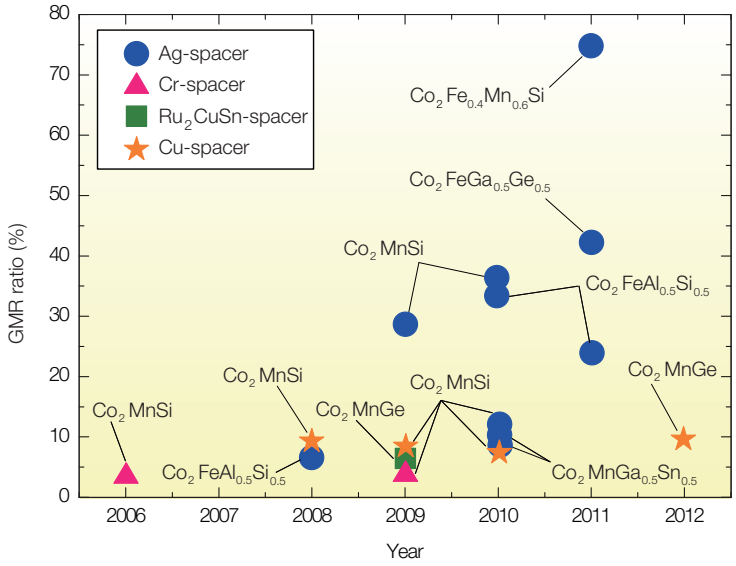

Figure 1.2: Development of the GMR ratio at room temperature for CPP-GMR SVs with Heusler electrodes.

ΔRA is determined by the intrinsic spin-asymmetry coefficients not only in the bulk FM electrode (β) but also at the FM/NM interfaces (γ). Good band matching (Fermi surface matching) between the electrode and spacer materials for the majority spin is a predominant factor in achieving large GMR.[70–74, 79]

These considerations, combined with a small lattice mismatch, have led to the selection of silver as an ideal spacer material coupled with the Heusler electrodes. Consequently, a CPP-GMR ratio of 6.9% at room temperature was realized in a $Co_2FeAl_{0.5}Si_{0.5}$/Ag/ $Co_2FeAl_{0.5}Si_{0.5}$ trilayer stack.[75] Further enhanced CPP-GMR ratios of 34% for the same system[76] and of 24% in an antiferromagnetic interlayer-exchange-coupling architecture[77] were reported. For CMS-based CPP-GMR stacks, much larger MR ratios of 28.8%[78] and 36.4%[79] were also observed by the substitution of Cr spacers by the Ag ones. In the last few years, the employment of various quaternary Co-based

Heusler compounds as electrodes were also witnessed with relatively large MR values: 8.8%[80] and 10.2%[81] of $Co_2MnGa_{0.5}Sn_{0.5}$, 41.7% of $Co_2FeGa_{0.5}Ge_{0.5}$,[82] and 74.8% , the largest value so far to our best knowledge, of $Co_2Fe_{0.4}Mn_{0.6}Si$.[83] The development of MR values in CPP-GMR SVs with various electrode and spacer materials is illustrated in Fig.1.2.

The "all-Heusler " design scheme

In order to push the ΔRA values into an applicable range, an "all-Heusler "architecture, composed of both Heusler-compound electrodes and spacer, is proposed. The potential benefit of such architecture is the optimization of interface spin asymmetry (γ) by taking advantage of the intrinsically matched crystal lattices and majority-spin electronic structures. In addition, the huge Heusler family provides sufficient choices of possible matching NM materials as spacer candidates. The very first all-Heusler architecture was demonstrated in a $Co_2MnGe(Si)/Ru_2CuSn/Co_2MnGe(Si)$ trilayer stack.[72, 84] However, the measured MR ratio was only $\sim$7%, which could possibly be attributed to the reduced interfacial spin polarization caused by the large lattice mismatch, atomic disorder and surface states in the MnGe terminated Co_2MnGe/Ru_2CuSn interface. Recently, an interesting all-Heusler compound interface Co_2CrSi/Cu_2CrAl was proposed.[71, 74] Co_2CrSi and Cu_2CrAl have the same lattice structure and their lattice constants match very well. First-principles electronic-structure calculations predicted an enhanced spin scattering asymmetry at the Co_2CrSi/ Cu_2CrAl interface, which makes the $Co_2CrSi/Cu_2CrAl/Co_2CrSi$ stacking structure an appealing candidate for the all-Heusler CPP-GMR architecture. Other all-Heusler interfaces like $L2_1$ Co_2MnSi/ Ni_2NiSi,[73] Fe_2CrSi/Cu_2CrAl,[86] as well as $C1_b$ NiMnSb/NiCuSb,[73] have also been

proposed by first-principles calculation. Based on consideration of fulfilling the requirement of the interfacial structural and chemical compatibilities, Chadov *et al.* proposed a delicate rule of material selection for the all-Heusler scheme,[85] which intends to provide stable high spin polarization at the interfaces of the magnetoresistance junctions. This can be realized by joining the semiconducting and half-metallic Heusler materials with similar structures. It was verified by first-principles calculations that the interface remains half-metallic if the nearest interface layers effectively form a stable Heusler material with the properties intermediately between the surrounding bulk parts.

1.2.2 Tunneling magnetoresistance: theoretical understanding of the lower-than-expected magnetoresistance value

Similar to GMR, large MR ratio also holds promise for TMR-based devices. In 2001, TMR ratio as high as 6000% was theoretically predicted in the Fe/MgO/Fe (001) MTJ from a ballistic conductance calculations.[16, 17] It was found that the decay rate of the wave function with the Δ_1 symmetry is much slower compared with those of the Δ_2 and Δ_5 channels in the single crystal MgO barrier owing to the symmetry compatibility with the complex Δ_1 band in the insulating gap of the MgO. Since *bcc*-Fe has half-metallic Δ_1 band, the Fe/MgO/Fe (001) MTJ can provide very large TMR. Three years later, high TMR ratios of about 180% in the Fe/MgO/Fe (001) MTJ[20] and about 220% in the CoFe/MgO/CoFe (001) MTJ[19] were successfully achieved at room temperature. Nevertheless, the values are still much lower than the theoretical predictions(up to 10,000%).[16–18] Theorists argued that various realistic defects, e.g., interfacial roughness, interfacial resonance, oxidization at metal/MgO interfaces, and

oxygen vacancy in MgO, were among the possible reasons for the observed low TMR ratio, because defect-induced diffusive scattering could diminish the symmetry selective filtering mechanism.[87–94].

Based on these theoretical understandings, experimentalists have improved the fabrication technique by introducing light boron atoms into the electrodes to make up amorphous CoFeB electrodes, which reduces metal/MgO interfacial roughness,[95] hinders interfacial oxidation by inert boron,[96] and passivates oxygen vacancies in MgO through boron diffusion.[97–100] Therefore, it seems all shortcomings that cause the low TMR in the (Co)Fe/MgO/(Co)Fe system can be removed using CoFeB electrodes. Following this approach, Lee et al. recently reported a record high TMR ratio of 1010% at 5 K in CoFeB/MgO/CoFeB MTJs.[96] This value, however, is still one order of magnitude lower than the theoretical prediction.[16–18] Such a large discrepancy remains as an open question requiring further theoretical investigation on electron tunneling through the CoFeB/MgO/CoFeB MTJs.

1.2.3 Tunneling magnetoresistance: materials design of perpendicular magnetized electrodes for spin-transfer torque magnetic random access memories

For the STT-MRAM applications, as the size of the device shrinks, the dilemma of balancing the writability and the thermal stability emerges as one of the most crucial issue[101]: For a smaller MTJ size, higher writing current density is required to overcome the increased thermal energy barrier; however, such a high density can only be

supplied by a larger transistor, which hinders the size downscaling of the MTJ in a one-transistor one-memory design scheme. In other words, the main challenge of implementing the STT-MRAM into high-density and high-speed memories is to reduce substantially the intrinsic current density required to switch the FM magnetization orientations while maintaining high thermal stability required for long-term data retention.

To address this challenge, an elegant scheme of perpendicular magnetization, in which MTJs possess perpendicular easy axes, was recently proposed as an alternative to the conventional in-plane geometry.[102–105] Two advantages are associated with such perpendicular magnetic anisotropy (PMA) scheme. On one hand, in patterned PMA devices, the magnetization is more uniform, and thus, less vulnerable to thermal fluctuation compared with the in-plane configuration with edge magnetization curling. This benefits the reduction of both the aspect ratio (length/width) of the film and the overall bit size.[102] On the other hand, the switching current of the MTJ can be decreased since PMA can counteract the large out-of-plane demagnetizing field which inhabits current-induced switching.[106–109]

A straightforward way to achieve PMA in MTJs is to take advantage of the FM films with intrinsic perpendicular anisotropy as the electrodes. However, traditional PMA materials/heterostructures containing heavy noble-metal or rare-earth elements, such as $L1_0$-ordered FePt, CoPt, Co/Ni and (Co,Fe)/(Pt, Pd) multilayers, are not ideal due to their huge Gilbert damping constants and the induced large switching current density. Very recently, it has been proposed that a group of DO_{22} tetragonally distorted Heusler compounds, the series of $Mn_{3-x}Ga$ ($0 \leq x \leq 1$) as representative prototype, also possess perpendicular easy axes. A more exciting fact is that they belong to soft compensated ferrimagnets with very small damping constants. In addition, the combination of high

spin-polarization, high Curie temperature, and low magnetization is another factor which makes $Mn_{3-x}Ga$ appealing as the electrode materials for STT applications.[110–112] Recent experimental efforts have demonstrated the effect of TMR within the epitaxial $Mn_{3-x}Ga$-based MTJs.[70]

1.2.4 Electric-field-assisted magnetization switching and its application in spin-transfer torque magnetic random access memories

In addtion to perpendicular magnetization, an alternative way to reduce writing current is to take advantage of electric-field-assisted switching which has been witnessed in CoFeB/MgO/CoFeB [113] and all-oxide composite [114–116] MTJs. In fact, electric-field control of magnetization is significant not only in sense of energy-efficiency, but also because of the compatibility with the current ubiquitous voltage-controlled semiconductor devices. The magnetoelectric (ME) effect has been widely studied in various systems both experimentally and theoretically. [113, 117–128, 181, 182] The efficiency of the electric-field manipulation is quantitatively characterized by the magnetocrystalline anisotropy (MCA) coefficient, β, defined as $\Delta\text{MAE} = \beta E$, where ΔMAE is the change in the MCA energy and E the applied electric field. Currently, FM/oxide interfaces show the best performance with the MCA coefficient $\sim 10^{-8}$ erg/V cm, which is, nevertheless, still below the requirement of practical low-power applications. Therefore, to predict and identify novel FM/oxide interfaces with giant MCA coefficient is another big challenge for achieving low-power devices.

1.3 Motivations and scope for the present work

As specified in the previous section, the huge gap between the performance of the present magnetic data storage devices and the requirements for the next-generation data recording technique are summarized below:

A common problem of almost all the current GMR and TMR devices is the insufficient signal-to-noise ratio (SNR). In addition, accompanying the device-size downscaling are the requirements for high information thermostability and low power consumption. To solve these problems, both theoretical understanding of the underlying physical mechanisms and practical design of novel materials/heterostructures are much required but still missing so far.

1. As for the Heusler-compound-based CPP-GMR HDD read heads, the GMR value is still much lower than expected, which hinders it from being applied practically. Even though an all-Heusler design scheme has been proposed to enhance the MR ratio, further studies are required to understand the interface physics and identify robust device structures. Furthermore, the relationship between the MR-related properties (i.e., β, γ, and ΔRA) and the structural/magnetic properties of the all-Heusler devices still remains unclear.

2. As for the TMR devices, the SNRs observed in realistic experiments are much lower than that predicted theoretically. Albeit various hypotheses were proposed to interpret the discrepancy, none of them have taken into consideration the boron-diffusion induced crystalline symmetry reduction, which is, however, inevitable in the state-of-the-art MTJ fabrication process, and may significantly affect the SNR.

3. In addition to theory, an essential issue in practice with the TMR devices is to concurrently achieve high thermostability, low energy consumption and large MR ratio. To address this challenge, tetragonal $D0_{22}$-phase Heusler compounds, $Mn_{3-x}Ga$, has been proposed in recent years as an appealing material for p-MTJ magnetic electrodes. However, a systematic *ab initio* calculation is missing so far and this hinders the evaluation of the suitability of the $Mn_{3-x}Ga$ series in such applications.

4. Recently a manner of electric-field assisted magnetization switching has also emerged as an efficient way to reduce the device energy consumption. Nonetheless, the electric-filed manipulation efficiency, i.e., the MCA coefficients ($\sim 10^8$ erg/V cm), is still below the requirement of practical low-power applications.

The main aims of this study were not only to provide essential supplements to the existing GMR/TMR theories, but also to design suitable materials/heterostructures for next-generation magnetic recording applications. The specific objectives of this research were to:

1. identify promising all-Heusler-compound architecture and systematically study its structural, electronic, magnetic and transport properties.

2. investigate the role that the spacer crystalline symmetry plays in determining the magnetoresistance performance of the whole magnetic tunnel junction.

3. provide a comprehensive study on the electronic-structure and magnetotransport properties of the $Mn_{3-x}Ga$ series.

4. design promising $3d$-ferromagnet/oxide interfaces to construct p-MTJs which possess

high magnetoelelctric efficiency, along with high thermostability and large MR ratio.

Although experimental methods tend to be more expensive with time, computational methods become much cheaper as computers become faster. By using the theoretical modeling and first-principles computational methods, the present study, on the one hand, should shed more light on the aforementioned underlying physics of the GMR and TMR phenomenon. On the other hand, the novel materials/heterostructures proposed herein would provide a set of selection criteria to be used as suitable building blocks for the next-generation magnetic data storage devices.

Data storage is a highly industry-oriented research field with its primary focus on R&D, and more importantly, on the massive production of cutting-edge information recording devices. Many practical aspects, such as the fabrication technology and the control of cost, would be among the central issues of this research area, which, however, are beyond the scope of the present study. This thesis focuses on the much more fundamental and microscopic areas, i.e., theoretical understanding and materials design of high-performance GMR/TMR junctions which are the essential building blocks and functional elements of the macroscopic data storage devices. Information about such underlying mechanisms and design criteria can boost performance enhancement towards the next-generation magnetic data storage devices.

First-principles approaches based on DFT and spin-dependent non-equilibrium Greens function (NEGF) technique were used throughout this study to provide unbiased determination/prediction of the electronic-structure and magnetotransport properties of materials/heterostructures. The following chapter will describe these two theoretical approaches in detail. Chapter 3 presents the all-Heusler design scheme for the CPP-GMR

read sensors. Chapter 4 reports the effect of boron-diffusion induced spatial symmetry reduction of the spacer on the TMR performance of MTJs. Chapter 5 focuses on the evaluation of the suitability of the $Mn_{3-x}Ga$ series as p-MTJ electrodes. Chapter 6 proposes the Co_2FeAl/MgO/Co_2FeAl p-MTJ as the building block for low-power STT-MRAM applications. A summary will be given in Chapter 7 to conclude this thesis.

Chapter 2

Methodology

The electronic and magnetic properties of materials are calculated by first-principles calculations using density functional theory (DFT) implemented in VASP software package.[129, 130] The calculation on the transport properties is based on nonequilibrium Green's function (NEGF) combined with DFT implemented in ATK software package.[131, 132]

2.1 Density functional theory

2.1.1 Earlier approximation and density functional theory

In terms of quantum mechanics, the property of a many-body system is described by Schrödinger equation:

$$\hat{H}\Phi = E\Phi \,, \tag{2.1}$$

where E is the energy eigenvalue, $\Phi = \Phi(\mathbf{r}_1, \mathbf{r}_2, ..., \mathbf{r}_N)$ is the wave function, and $\hat{H}$ is the Hamiltonian operator, given by

$$\hat{H} = \sum_l \frac{\hat{P}_l^2}{2m_l} + \frac{1}{2}\sum_{l \neq l'} \frac{q_l q_{l'}}{|\mathbf{r}_l - \mathbf{r}_{l'}|} \,, \tag{2.2}$$

where the summation is over all electrons and nuclei in the system, m_l is the mass of an electron or nucleus, and q_l is its charge.

For any practical system, one has to resort to many approximations. First of all, the Born-oppenheimer approximation is used to remove the nuclei from the system and treats them as in an adiabatic environment due to the fact that the nuclei are much heavier, hence move much slower than the electrons. In this approximation, the kinetic energy of the nuclei is neglected and the interaction between the nuclei can be handled classically. Thus, the original problem in Eq. (2.1) is reduced to one regarding a system of interacting electrons moving in an external potential $V(\mathbf{r})$, formed by a frozen-in ionic configuration. But, due to the electron-electron interaction, the equation can not still be solved easily. Hatree approximation separates the many-body equation into independent equations in the coordinates of the individual electrons, of which Ψ can be written as a product of one-electron wavefunctions based on the assumption that the

electrons interact only via the Coulomb force. With incorporation of electron spin effects in later Hatree-Fork equation, the resultant ground state electron wavefunctions can be found variationally by using a trial wavefunction to solve the equation until the result meets the convergence. This is the self-consist approximation. However, the calculated energy by solving the Hartree-Fock equations does not equal to that of many-body Schrödinger equation under the Born-oppenheimer approximation. It turns out that the calculations of this correlation energy and exchange energy (the energy difference for exchanging electrons in solving Hartree-Fock equations) of a complex system is very difficult. Overcoming these difficulties to some extent is the driving force to develop alternative methods, which are required to describe the electron-electron interactions more precisely and can reduce the electronic Schrödinger equation to some more attractable equations which can be solved much easily in practice.

A breakthrough is the density functional theory. Based on the following two theorems in terms of the electron density function $\rho(\mathbf{r})$:

Theorem I. If the number of electrons in the system is conserved, the external potential $V(\mathbf{r})$ uniquely determines the ground state density $\rho_0(\mathbf{r})$.

Theorem II. There exist a universal functional of ρ, E[ρ], which is minimized by the ground state density $\rho_0(\mathbf{r})$.

Kohn and Sham carried these theorems further and obtained a single-particle Schrödinger equation (Kohn-Sham equation) [133],

$$\{-\frac{1}{2}\nabla^2 + \int \frac{\rho(\mathbf{r})'}{|\mathbf{r}-\mathbf{r}'|}d^3\mathbf{r}' + \frac{\delta E_{xc}[\rho(\mathbf{r})]}{\delta\rho(\mathbf{r})} + V(\mathbf{r})\}\psi_i(\mathbf{r}) = \varepsilon_i\psi_i(\mathbf{r}), \tag{2.3}$$

where the first term in the Kohn-Sham equation is the kinetic energy, and the following terms are the Coulomb (or Hartree), the exchange-correlation (xc) and the external (*e.g.* the ionic) potentials, respectively. Kohn-Sham equation maps a many-electron interacting system into a single electron system within an effective potential formed by the nuclei and other electrons. Comparing with the many-body Schrödinger equation in Eq. (2.1), solving the Kohn-Sham equation is much easier for a practical system.

Due to the functional dependence on the density, the Kohn-Sham equation forms a set of nonlinear coupled equations, and the standard procedure to solve it is iterating until self-consistency is achieved. Starting from an assumed density $\rho(\mathbf{r})$, firstly the Coulomb and xc potentials are calculated, then solve Eq. (2.3) for the Kohn-Sham wavefuctions. With these wavefunctions, a new density can be constructed by

$$\rho(\mathbf{r}) = \sum_i |\psi_i(\mathbf{r})^2|, \tag{2.4}$$

where the index i goes over all occupied states. This procedure is repeated until self-consistency (*i.e*, consistency between the output and input densities) is obtained.

2.1.2 The exchange-correlation functional approximation

The formalism of the Kohn-Sham equation is much simpler than that of other first-principles methods, such as the Hartree-Fock method. However, in the Kohn-Sham equation, all items are treated exactly, except one term, the exchange-correlation functional $\varepsilon_{xc}[\rho(\mathbf{r})]$, which is unknown. The search for an accurate $\varepsilon_{xc}[\rho(\mathbf{r})]$ has proven to be extremely difficult, and various approximations have been made. Among them, local density approximation (LDA) [133] is the simplest, which is based on the assumption

that, for a system with slowly varying density, the electron density in a small region near point $\mathbf{r}$ can be treated as if it is homogeneous. Therefore, the $\varepsilon_{xc}[\rho(\mathbf{r})]$ can be written as

$$\varepsilon_{xc}[\rho(\mathbf{r})] = \int \epsilon_{xc}(\mathbf{r})\rho(\mathbf{r})d^3\mathbf{r}, \tag{2.5}$$

where ϵ_{xc} is the xc energy per electron. Despite its simple form, the LDA is remarkably successful in predicting the structural and electronic properties of materials. On the other hand, several problems are also encountered with the LDA. For example, LDA can not give a good description on excited states, thus underestimates the band gap of semiconductor and insulator. LDA also tends to overbind, so the calculated lattice constant is underestimated and the cohesive energy is overestimated. In addition, the LDA cannot work well for the Van der Waals interactions, and it also gives wrong predictions for some strongly correlated magnetic systems.

An improvement for the LDA is the generalized gradient approximation (GGA), in which the exchange-correlation functional is treated as the functional of the electron density and the gradient of the electron density:

$$\varepsilon_{xc}[\rho(\mathbf{r})] = \int f(\rho, \nabla\rho)d^3\mathbf{r}, \tag{2.6}$$

A variety of choices for $f(\rho, \nabla\rho)$ can be made. [134–136] The GGA can correct some problems of the LDA, such as the overbinding tendency and the wrong prediction of the non-magnetic ground state of Fe $etc.$ However, the GGA has also the underbinding problem, which results in the overestimation of lattice constants and the underestimation of cohesive energies. The excited states, strong correlated systems, and the Van de Waals interactions also cannot be correctly handled in GGA.

2.1.3 Bloch's theorem and supercell approximation

With the density functional theory, the many electron Schrödinger equation can be mapped onto the N one-electron Kohn-Shan equations. However, solid systems typically contain $\sim 10^{23}$ particles, which requires us to solve the Kohn-Sham equations with an infinite numbers orthogonalizational equations. This is impractical. Fortunately, we can reduce the infinite problems to a finite periodic systems based on the Bloch's theorem.

For a system of electron moving in a periodic potential, Bloch's theorem states that the corresponding wavefunction of the electron has the form:

$$\psi_k(\mathbf{r} + \mathbf{R}) = e^{i\mathbf{kr}} u_k(\mathbf{r}), \tag{2.7}$$

where $u_k(\mathbf{r})$ has the same periodicity as the potential. For a crystal lattice potential, it satisfies the following translation invariance:

$$u_k(\mathbf{r} + \mathbf{R}) = u_k(\mathbf{r}), \tag{2.8}$$

where $\mathbf{R}$ is a real space lattice vector.

Based on this theorem, the wavefunction of a single atom in a lattice can be written as the product of the plane wave and the periodic function $u_k(\mathbf{r})$. Also, the wavevector $\mathbf{k}$ can always be folded into the first Brillouin zone (1BZ) in the context of electronic property calculations since the electron energy is periodic in the $\mathbf{k}$-space and each $\mathbf{k}$-point outside the 1BZ can be mapped onto a $\mathbf{k}$-point inside. The number of $\mathbf{k}$-points in the 1BZ is equal to the number of unit cells in real space. Since the number of unit cells is in the magnitude of $\sim 10^{22}$, the $\mathbf{k}$-points in the 1BZ is quasi-continuous.

Many real systems do not have periodic symmetry along all three dimensions. For example, an interface system only has periodic symmetry parallel to the interface; a carbon nanotube is only one dimension and an isolated atom or molecule is completely aperiodic. To study these systems, two approximations are feasible. One is to model the system with a cluster of atoms. Another is to artificially model a periodic symmetry on the aperiodic dimension. This is the so-called supercell technique. For a interface system, the supercell approximation is implemented by modeling the interface with periodically arranged slabs which are separated by vacuum layers. To minimize the artificial Coulomb interactions between two neighbor surfaces, the vacuum layer should be thicker than 10 Å. The thickness of the slabs is dependent on the specific case, and normally the slab with smaller interlayer spacing should be thicker.

2.1.4 Brillouin zone sampling

Electronic states are allowed only at a set of $\mathbf{k}$-points determined by the boundary conditions that apply to the bulk solid. The density of allowed $\mathbf{k}$-points is proportional to the volume of the solid. The infinite number of electrons in the solid are accounted for by an infinite number of $\mathbf{k}$-points, and only a finite number of electronic states are occupied at each $\mathbf{k}$-point. By virtue of Bloch's theorem, the calculations of an infinite number of electronic wavefunctions in full space can be reduced to a finite number of electronic wave functions with an infinite number of $\mathbf{k}$-points in 1BZ. In principles, each $\mathbf{k}$-point in 1BZ have to be considered for the calculations, due to the fact that the occupied states at each $\mathbf{k}$-point contribute to the electronic potential in the bulk solid, typically, through

the following integrals,

$$I(\varepsilon) = \frac{1}{\Omega_{BZ}} \int_{BZ} F(\varepsilon)\delta(\varepsilon_{n\mathbf{k}} - \varepsilon)d\mathbf{k}, \tag{2.9}$$

where Ω_{BZ} is the volume of the BZ.

Fortunately, the electronic wavefunctions at **k**-points that are very close will be almost identical. This makes us possible to represent the wavefunctions over a region of **k** space by the wavefunctions at a single **k**-point, which indicates that only a special finite numbers of **k**-points in the 1BZ are required to calculate the electronic potentials:

$$\frac{1}{\Omega_{BZ}} \int_{BZ} f(\mathbf{k})d\mathbf{k} \Longrightarrow \sum_{\mathbf{k}_i} \omega_{\mathbf{k}_i} f(\mathbf{k}_i), \tag{2.10}$$

where $\omega_{\mathbf{k}_i}$ is the weight of $\mathbf{k}_i$. The magnitude of any error in the total energy due to inadequacy of the **k**-points sampling can always be reduced by using a denser set of **k**-points. In principle, the **k**-points mesh should be increased until the calculated total energy is converged.

Various methods have been proposed for the **k**-points sampling in the 1BZ [137, 138], in which one of the most widely used is the Monkhorst-Pack scheme. [138] The basic idea of Monkhorst-Pack scheme is to construct equally spaced **k**-points ($N_1 \times N_2 \times N_3$) in 1BZ according to

$$\mathbf{k} = \frac{n_1 + 1/2}{N_1}\mathbf{b_1} + \frac{n_2 + 1/2}{N_2}\mathbf{b_2} + \frac{n_3 + 1/2}{N_3}\mathbf{b_3}, \tag{2.11}$$

where n_1, n_1, and n_3=0,$\cdots$, N_i-1. Symmetry is used to map equivalent k-points to each other, which can reduce the total number of k-points significantly generated by Eq. (2.11).

2.1.5 Plane-wave basis sets

Based on Bloch's theorem, the electronic wavefunctions at each **k**-points can be expanded in terms of a discrete plane-wave basis sets:

$$\psi_{n,\mathbf{k}}(\mathbf{r}) = \sum_{\mathbf{G}} c_{n,\mathbf{k}+\mathbf{G}} \exp[i(\mathbf{k}+\mathbf{G})\cdot\mathbf{r}]. \tag{2.12}$$

After expanding the wavefunctions as Eq. (2.12), the Kohn-Shan equations can be reduced to the secular equation:

$$\sum_{\mathbf{G}'}[\frac{\hbar^2}{2m}|\mathbf{k}+\mathbf{G}|^2\delta_{\mathbf{G}\mathbf{G}'}+V(\mathbf{G}-\mathbf{G}')+V_H(\mathbf{G}-\mathbf{G}')+V_{xc}(\mathbf{G}-\mathbf{G}')]c_{n,\mathbf{k}+\mathbf{G}'} = \varepsilon_{n,\mathbf{k}}c_{n,\mathbf{k}+\mathbf{G}}. \tag{2.13}$$

In principle, an infinite plane-wave basis set is required to expand the electronic wavefunctions. Fortunately, the the coefficient $c_{n,\mathbf{k}+\mathbf{G}}$ for the plane-wave with small kinetic energy $\frac{\hbar^2}{2m}|\mathbf{k}+\mathbf{G}|^2$ are typically more important than those with large kinetic energy. Thus, the plane-wave basis set can be truncated to include only plane-waves that have kinetic energies less than some particular cutoff energy $E_{\text{cut}} = \frac{\hbar^2}{2m}|\mathbf{k}+\mathbf{G_{cut}}|^2$. The truncation of the plane-wave basis set at a finite cutoff energy will lead to an error in the computed total energy. However, it is possible to reduce the magnitude of the error by increasing the cutoff energy. Normally, the cutoff energy should be increased until the total energy has converged.

2.1.6 The pseudopotential approximation

Although Bloch's theorem states that the electronic wavefunctions can be expanded using a discrete set of plane-waves, a very large number of plane-waves is needed to

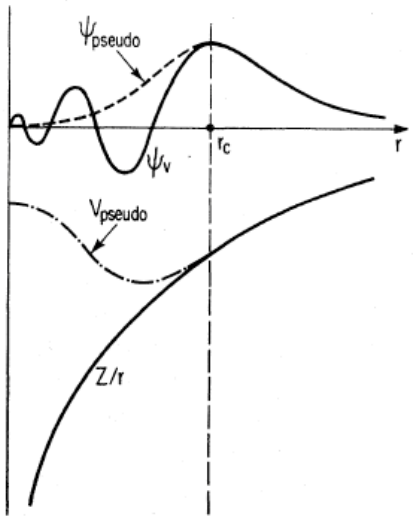

Figure 2.1: Schematic illustration of all-electron potential (solid lines) and pseudopotential (dash lines) and their corresponding wavefunctions.

expand the tightly bound core orbitals and to follow the rapid oscillations of wavefunctions of the valence electrons in the core region due to the strong ionic potential in this region, which would make the all electron calculations are very expensive and even impractical for a large system. Fortunately, the pseudopotential approximation allows the expansion of electronic wavefunctions with much smaller number of plane-wave basis sets. [139–141]

Based on the fact that most of physical properties of solids are mainly determined by the valence electrons, the pseudopotential approximation removes the core electrons and strong ionic potential, and replaces them by a weaker pseudopotential that acts on a set of pseudo wavefunctions rather than the true valence wavefunctions, as Fig. 2.1 shows. The nonlocal and angular momentum dependent pseudopotentials are usually generated from isolated atoms or ions, but can be used in other chemical environment such as

solids (transferability of the pseudopotentials). The general form for a pseudopotential is

$$V_{NL} = \sum_{lm} |lm\rangle V_l \langle lm|, \tag{2.14}$$

where $|lm\rangle$ is the spherical harmonics and V_l is the pseudopotential for the angular momentum l.

The construction of the pseudopotential within the core radius r_c should preserve the scattering properties, which means that the scattering properties for the pseudo wave-functions should be identical to that of the ion and core electrons for the valence wave-functions. The scattering properties are satisfied automatically in the region outside the r_c since there the pseudopotential and the true potential are the same. In order to improve the transferability, the norm-conserving condition:

$$\int_0^{r_c} |\phi_{n,\mathbf{k}}(\mathbf{r})|^2 d\mathbf{r} = \int_0^{r_c} |\psi_{n,\mathbf{k}}(\mathbf{r})|^2 d\mathbf{r} \tag{2.15}$$

should be fulfilled.

Norm-conserving pseudopotentials are very successful for solids of s, p-bond main group elements, but they do not give good results for the first-row elements, transition metals, and rare-earth elements due to the highly localized valence orbitals in these elements. Fortunately, this difficulty has been overcome by introducing the so-called ultrasoft pseudopotentials proposed by Vanderbilt. [142] More recently, a more accurate and efficient pseudopotential formalism, the projector augmented-wave (PAW) [130, 143], has been developed by Blöchl. Compared with the ultrasoft pseudopotentials, PAW has smaller radial cutoffs (core radii), and also exactly reconstructs the valence wave function with all nodes in the core region, which makes PAW more accurate than ultrasoft

pseudopotentials in many systems while the calculations using PAW are not more expensive.

2.2 The non-quilibrium Green's function

In our model Hamiltonian and transport calculations, the lead parts are calculated separately using DFT to get the self-consistent Kohn-Sham potentials[133] and Hamiltonian matrices. The Hamiltonian reads

$$H = \{-\nabla^2/2 + V^{\delta H}(r) + V^{NA}(r) + V^{xc}(r)\} \times \delta(r - r') + V^{NL}(r, r') \quad (2.16)$$

where, $V^{\delta H}(r)$ is the screened Hartree potential which is used to solve the Poisson equation

$$\nabla^2 V^{\delta H}(r) = -4\pi\{\rho(r) - \rho^{NA}(r)\} \quad (2.17)$$

$V^{NA}(r)$ is the local pseudopotential screened by the addition of charge density of the neutral isolated atoms $\rho^{NA}(r)$. $V^{xc}(r)$ is the exchange-correlation potential of electrons. multiplying by two numerical basis orbitals ξ_μ and ξ_υ and integrating over dr and dr' leads to the corresponding Hamiltonian matrix H. Thus, the Green's function is evaluated by inverting the finite matrix

$$G = \begin{pmatrix} H_L + \sum_L & V_L & 0 \\ V_L^\dagger & H_C & V_R \\ 0 & V_R^\dagger & H_R + \sum_R \end{pmatrix}^* \quad (2.18)$$

where H_L, H_C and H_R are the Hamiltonians of the left leads, central portion and the right leads, respectively, and V_L (V_R) is the interaction between left (right) lead and the

central portion. $\sum_L$ and $\sum_R$ are the self energies due to coupling to the left and right leads.

We can get the density matrix based on the above Green's function

$$D_{\mu\upsilon} = \int_{-\infty}^{\infty} \frac{1}{\pi} \mathrm{Im} G(\varepsilon) n_F(\varepsilon - \mu) d\varepsilon \tag{2.19}$$

where n_F is the Fermi function and μ is the chemical potential. The electron density is given by

$$\rho(r) = \sum_{\mu,\upsilon} \xi_\mu(r) D_{\mu,\upsilon} \xi_\upsilon(r) \tag{2.20}$$

This allows us to calculate the DFT Hamiltonian elements H. Once the self-consistency is achieved in the open system, the spin-polarized current through the system is calculated

$$I^{\uparrow(\downarrow)}(V_b) = \frac{e}{h} \int_{-\infty}^{\infty} \{T^{\uparrow(\downarrow)}(\varepsilon, V_b)[f_L(\varepsilon, V_b) - f_R(\varepsilon, V_b)]\} d\varepsilon \tag{2.21}$$

where $f_{L(R)}(\varepsilon, V_b) = n_F(\varepsilon - \mu_{L(R)})$ and $\mu_{L(R)}$ are the electrochemical potentials of each leads. The $T^{\uparrow(\downarrow)}(\varepsilon, V_b)$ is the spin-resolved transmission value defined as

$$T^{\uparrow(\downarrow)}(\varepsilon, V_b) = Tr[\mathrm{Im}\{\Sigma^r_{L\uparrow(\downarrow)}(\varepsilon, V_b)\} G^r_{\uparrow(\downarrow)}(\varepsilon, V_b) \times \mathrm{Im}\{\Sigma^r_{R\uparrow(\downarrow)}(\varepsilon, V_b)\} G^a_{\uparrow(\downarrow)}(\varepsilon, V_b)] \tag{2.22}$$

where $\sum^r_{L/R}$ is the retarded self-energy matrix used to take into account the left and right lead. G^r/G^a is the retarded or advanced Green's function matrix.

2.3 The collinear- and noncollinear-spin transport method

In the collinear-spin system, all spins are restricted along a global spin-quantization axis (either parallel or antiparallel), with the spin-up and spin-down electrons completely decoupled from each other, i.e., no spin flip occurs. In transport theory, this spin-resolved

manner is known as the "two-spin fluid "approximation, of which the Hamiltonian, overlap matrix and all other operators have the form of a 2×2 matrix in spin space,

$$A = \begin{pmatrix} A^{\uparrow} & 0 \\ 0 & A^{\downarrow} \end{pmatrix} \tag{2.23}$$

where A^{σ} denotes the spin σ sub-band. In this case, the two spins can be separated and treated independently,each as that in the non-spin polarized system.

On the contrary, the non-collinear spin scheme allows a spatial variation of the spin directions. In such circumstance, the operators have the following general form,

$$A = \begin{pmatrix} A^{\uparrow\uparrow} & A^{\uparrow\downarrow} \\ A^{\downarrow\uparrow} & A^{\downarrow\downarrow} \end{pmatrix} \tag{2.24}$$

The off-diagonal terms couple the up and down spins and are related to the angles between the local magnetization and the global spin-quantization axis. For transport calculation, the NEGF entries have to be extracted from the non-collinear spin DFT[146–148] which take cares of the general spin orientations.

We start from the density matrix $\rho(\mathbf{r})$, which can be treated as an equivalent 2×2 Hermitian matrix of the charge density $n(\mathbf{r})$ and the vector magnetization quantity **m(r)**,[149]

$$\rho(\mathbf{r}) = \frac{1}{2}(n(r)\mathbf{I} + \mathbf{m}(\mathbf{r}) \cdot \boldsymbol{\sigma}) = \frac{1}{2} \begin{pmatrix} n(\mathbf{r}) + m_z(\mathbf{r}) & m_x(\mathbf{r}) - im_y(\mathbf{r}) \\ m_x(\mathbf{r}) + im_y(\mathbf{r}) & n(\mathbf{r}) - m_z(\mathbf{r}) \end{pmatrix} \tag{2.25}$$

where **I** is a 2×2 unit matrix in spin space and $\boldsymbol{\sigma}$ the standard Pauli matrix, respectively. $n(\boldsymbol{r})$ and **m(r)** are defined in the global coordinate reference. The off-diagonal elements

of Eq. 2.25, introduced by the non-collinear scheme, are essentially the magnetization perpendicular to the global spin-quantization axis. At a given **r**, the density matrix $\rho(\mathbf{r})$ can be diagonalized to the collinear form through a unitary transformation from the global coordinate reference to the local one that parallels the z-axis magnetization orientation,[150]

$$\rho(\mathbf{r}) = \mathrm{U}^{\dagger}(\theta(\mathbf{r}), \varphi(\mathbf{r})) \begin{pmatrix} \rho_{\uparrow}(\mathbf{r}) & 0 \\ 0 & \rho_{\downarrow}(\mathbf{r}) \end{pmatrix} \mathrm{U}(\theta(\mathbf{r}), \varphi(\mathbf{r})) \tag{2.26}$$

where U is the well-known spin-1/2 rotation matrix,

$$\mathrm{U} = \begin{pmatrix} e^{\frac{1}{2}i\varphi}\cos(\frac{1}{2}\theta) & e^{-\frac{1}{2}i\varphi}\sin(\frac{1}{2}\theta) \\ -e^{\frac{1}{2}i\varphi}\sin(\frac{1}{2}\theta) & e^{-\frac{1}{2}i\varphi}\cos(\frac{1}{2}\theta) \end{pmatrix} \tag{2.27}$$

where φ and θ are azimuthal and polar angles of the magnetization **m(r)** with respect to the global coordinate reference.

Following the standard variational procedure for the Hohenberg-Kohn functional $E^{HK}(\rho(\mathbf{r}))$, we get the noncollinear Kohn-Sham mean-field Hamiltonian,

$$H_{noncol-DFT} = (-\frac{\hbar^2}{2m}\nabla^2 + V_0(\mathbf{r}))\mathbf{I} + \mathbf{V}(\mathbf{r}) \cdot \boldsymbol{\sigma} \tag{2.28}$$

where $V_0(r)$ and $V(r)$ are the non-magnetic and magnetic parts of the DFT effective potential $V_{eff}(\mathbf{r})$ consisting of the external, Hartree, and exchange and correlation potentials. $V_{eff}(\mathbf{r})$ can be diagonalized in the same manner as the density matrix $\rho(\mathbf{r})$,

$$V_{eff}(\mathbf{r}) = \mathrm{U}^{\dagger}(\theta(\mathbf{r}), \varphi(\mathbf{r})) \begin{pmatrix} V_{eff}(\rho_{\uparrow}(\mathbf{r})) & 0 \\ 0 & V_{eff}(\rho_{\downarrow}(\mathbf{r})) \end{pmatrix} \mathrm{U}(\theta(\mathbf{r}), \varphi(\mathbf{r})) \tag{2.29}$$

where $V_{eff}(\rho_{\uparrow/\downarrow}(\mathbf{r}))$ is completely analogous to the effective potential in the collinear ferromagnetic gas theory and hence can be approximated by L(S)DA. Then the Hamiltonian, in combination with the overlap and density matrices of the noncollinear magnetized leads, can be solved self-consistently by DFT bulk calculation in the normal

way and used to set up the electron density, chemical potential, and self-energies for the non-collinear transport calculation.

It should be noted that the above non-collinear transport scheme in this thesis (in Chapter 6) only takes into consideration the inhomogeneous magnetization induced spin-channel mixing, by which one can evaluate how the non-collinear magnetism of the leads affect the tunneling magnetoresistance. No fully relativistic spin-orbit coupling effect is included, and therefore the direct spin-flip process is ignored.

2.4 VASP and ATK software packages

VASP (Vienna *ab initio* simulation package) [129, 130] is a first-principle calculation code within the DFT framework, which uses ultrasoft pseudopotentials or the PAW method and a plane wave basis set. The approach implemented in this code is based on the (finite-temperature) LDA with the free energy as variational quantity and an exact evaluation of the instantaneous electronic ground state at each molecular dynamics (MD) time step. It also uses efficient matrix diagonalisation schemes and an efficient Pulay/Broyden charge density mixing. Thus, it can give information about total energies, forces and stresses on an atomic system, as well as calculating optimum geometries, band structures, optical spectra, *etc.* It can also perform first-principles molecular dynamics simulations.

ATK (Atomistix ToolKit) [131, 132] is designed to help to understand and improve the functionality of nanoscale systems. The modeling platform can be used to calculate electrical properties of nanostructures coupled to semi-infinite electrodes under a finite bias

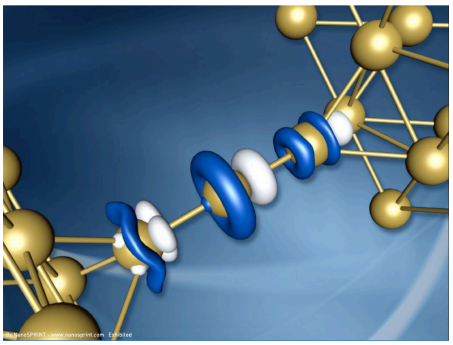

Figure 2.2: Schematic illustration of two-probe system in ATK

voltage (so-called two-probe systems). In addition, Atomistix ToolKit can be used for conventional electronic structure simulations, including spin-polarized calculations and atomic geometry optimizations, of periodic and isolated systems. Transport properties: 1) transmission coefficients and transmission spectra in the presence/absence of an applied bias voltage; 2) *I*-*V* characteristics; 3) density of states and local density of states; 4) voltage drop across a two-probe system; 5) spin-dependent transport, and much more. Based on self-consistent density functional theory (DFT) and non-equilibrium Green's functions for the transport calculations, atomic-scale modeling in Atomistix ToolKit is an efficient and powerful tool for calculating and understanding the intrinsic properties of nanoscale systems. The strength of ATK lies in its flexibility to describe systems of different symmetries. It can describe isolated systems (molecules), periodic systems (crystals), and systems of the type bulk-nanodevice-bulk (two-probe systems). The most unique feature of ATK is its ability to calculate the electronic transport properties of two-probe systems under a finite bias. However, the relaxation under bias and the simulation of the gate voltage are the two limitation of the current version of ATK software.

In this thesis, VASP were heavily used for the calculation of electronic/magnetic properties of various magnetic materials/heterostructures, whereas the spin-transport properties, such as magnetoresistance of the TMR/GMR devices, were calculated using ATK.

Chapter 3

The all-Heusler design scheme of CPP-GMR read heads

3.1 Introduction

Continuous evolution of HDD read heads, with higher sensor output, lower resistance, and higher bit resolution, is essential for further increase in the areal density in massive magnetic recording. Low-resistance magnetoresistance (MR) devices are of urgent requirement for impedance matching between read sensors and the preamplifiers, for lower electric noises, and for high frequency data transfer.[35, 151, 152] A read-sensor resistance-area product (RA) less than 0.1 $\Omega\mu m^2$ is necessary for a recording density higher than 2 Tbit/in^2.[35] This is a big challenge for the current magnetic tunnel junctions (MTJs) with a high impedance insulator spacer, but can be easily achieved using the CPP-GMR spin valves(SVs) composed of all-metallic layers. The RA values

of CPP-GMR SVs are typically below 0.05 $\Omega\mu m^2$. However, the drawback of the CPP-GMR SVs based on conventional ferromagnetic materials is their low signal-to-noise ratio(SR). For example, the resistance change-area product of the CoFe-based CPP-GMR SV is $\sim$ 1 $m\Omega\mu m^2$,[153, 154] which must be improved substantially. The utilization of half-metallic FM materials, such as the cobalt-based Heusler compounds, is expected to provide efficient spin-dependent scattering in the FM electrodes, thereby improving ΔRA.[69] Nevertheless, the MR performance of the current Heusler-based GMR devices is not as good as expected, e.g., the largest room-temperature (RT) GMR ratio achieved so far is only 74.8%, which is still too low for practical application.[83] The less satisfactory MR performance could be partially attributed to two challenges. One is the difficulty in fabricating "stoichiometric perfect"Heusler electrodes. The defect states, induced mostly by configurational disorders, destroys the half-metallic ground state. The other one is the non-perfect interface between the Heusler electrodes and transition-metal (TM) spacers (mismatch of the lattice structures, energy bands, and Fermi surfaces). These two challenges drastically degrade the device performance. According to the Valet-Fert model,[11] ΔRA can be expressed by two factors which determine the overall spin-dependent electron scattering, i.e., the bulk spin-asymmetry coefficient within the FM electrodes and the interfacial spin-asymmetry coefficient at the electrode-spacer interfaces. The β is enhanced by the employment of half-metallic electrodes, whereas the enhancement of the γ can be achieved via the modification of the spin-dependent interfacial resistance by a rational design of the interface structure. Specifically, in CPP-GMR devices with half-metallic Heusler electrodes, looking for matching non-magnetic (NM) spacers is crucial to construct such a working interface with large γ. The all-Heusler structure, with both the FM electrodes and NM spacer

composed of the Heusler compounds, can be a possible solution due to the intrinsically matched crystal lattices and electronic structures between the electrode-spacer pair. Besides, the huge Heusler family provides sufficient choices of possible matching NM candidates. Efforts have been made in designing and fabricating all-Heusler GMR junctions in the past decade.[71–74, 84–86] Even though some structural design principles have been proposed, further studies are required to understand the interface physics and identify robust device structures. Furthermore, the relationship between the MR-related properties (i.e., β, γ, and ΔRA) and the structural/magnetic properties of the all-Heusler devices still remains unclear.

In Section 3.1 of this chapter, we elaborated on a Co_2CrSi(CCS)Cu_2CrAl(CCA)/Co_2CrSi trilayer model and spin-dependent quantum transport calculation to demonstrate as a first step the advantage of the all-Heusler design scheme in view of magnetoresistance improvement. In Section 3.2, a more general and comprehensive study, by comparing a prototypical Co_2MnSi(CMS)/Ni_2NiSi(NNS)/Co_2MnSi stack with the state-of-the-art CMS/Ag/CMS on both the electronic structure and magneto-transport properties was further carried out to illustrate the physical origin of the superiority of the all-Heusler architecture.

First principles electronic structure calculations based on DFT were performed using the VASP code,[129, 130] whereas the NEGF method combined with DFT implemented in the ATK package was utilized for the spin dependent transport calculation.[131, 132] The spin-polarized generalized-gradient approximation (SGGA) proposed by Perdew et al. was employed as the exchange and correlation functional consistently throughout this work.[135] For transport calculation, the double-ζ polarized basis set was used for

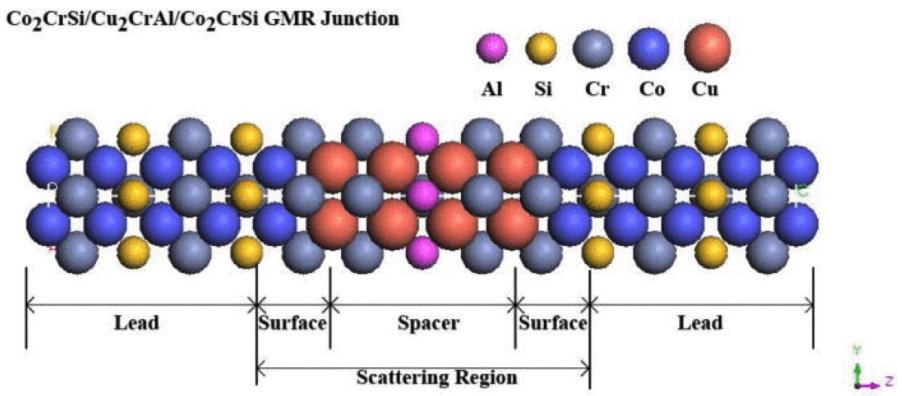

Figure 3.1: A schematic device model of the $Co_2CrSi/Cu_2CrAl/Co_2CrSi$ giant magnetoresistance junction.

the electron wave function. A cutoff energy of 150 Ry and a Monkhorst-Pack [138] **k**-mesh of $8 \times 8 \times 100$ yielded a good balance between computational time and accuracy in the results. It should be noted that conductance calculated using the DFT-NEGF method may deviate systematically from experimental measurement for the three-dimensional metallic multilayer structure. This, however, is not a concern here as the aim of our study is to understand the effect of the NM spacer in the FM/NM/FM trilayer structure instead of obtaining quantitative conductance of the system.

3.2 Results and discussion

3.2.1 The $Co_2CrSi/Cu_2CrAl/Co_2CrSi$ all-Heusler GMR junction: A case study

The CCS/CCA/CCS structure was modeled using a tetragonal supercell, as shown in Fig. 3.1. The in-plane lattice constant is set to 3.995 Å which is $1/\sqrt{2}$ of the experimental lattice constant (5.65 Å) of bulk CCS. There is a 2.8% lattice mismatch between CCS and CCA, and structural relaxation results in a 5.8% expansion of the CCA spacer along the (001) direction.

The calculated spin-dependent electron transmission spectra of the system are shown in Fig. 3.2. As can be seen in Fig. 3.2(b), there exists a transmission gap around the Fermi level for both spin-up and spin-down electrons when the magnetizations of the two electrodes are antiparallel, which results in a negligible conductance in this configuration. On the contrary, if the magnetizations of the electrodes are parallel, the transmission coefficient for the spin-up electrons is as high as 0.66 at the Fermi level, while that for the spin-down electrons remains almost zero, as shown in Fig. 3.2(a). Therefore, the current consists of essentially spin-up electrons in this magnetic configuration of the electrodes.

To understand the transport property, we examine the $\mathbf{k}_{//}$-dependence of the transmission channels at the Fermi level for both spin-up and spin-down electrons in the parallel and antiparallel configurations. Here, the in-plane electron wave vector $\mathbf{k}_{//}$=(k_x, k_y) specifies a point in the two-dimensional Brillouin zone perpendicular to the transmission direction(z-axis in Fig. 3.1). The $\mathbf{k}_{//}$-dependent transmission coefficient $T^{\sigma}(E_{\mathrm{F}}, \mathbf{k}_{//})$ is

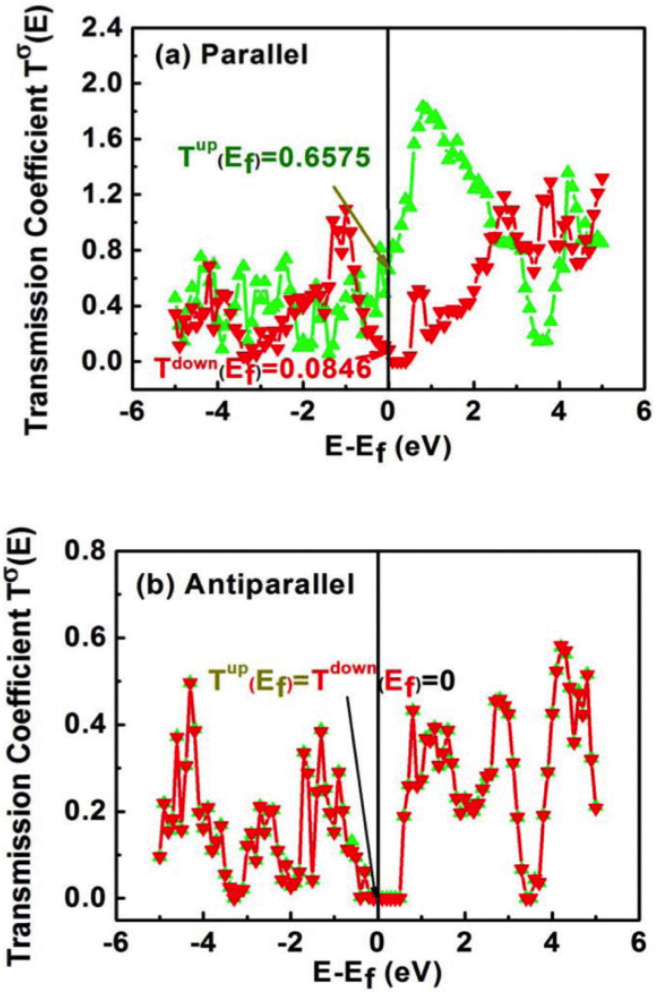

Figure 3.2: Spin-dependent transmission spectra of the $Co_2CrSi/Cu_2CrAl/Co_2CrSi$ junction at zero bias when the magnetization of the electrodes are (a) parallel and (b) antiparallel, respectively.

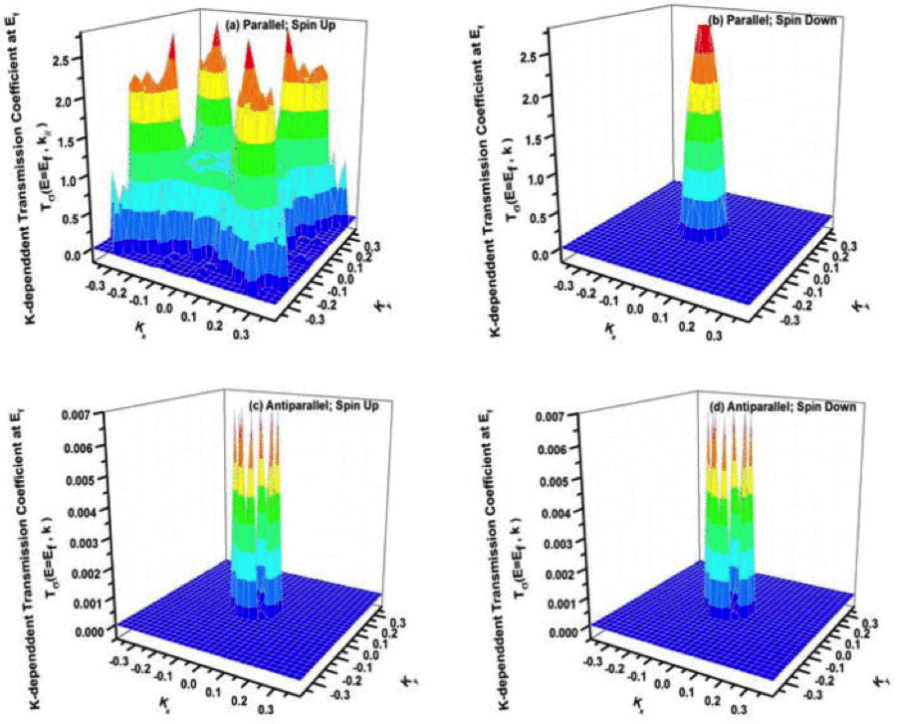

Figure 3.3: $\mathbf{k}_{//}$-dependence of spin-dependent transmission spectra, where $\mathbf{k}_{//}$=(k_x, k_y) is the in-plane wave vector specifying a point in the two dimensional Brillouin zone. (a) and (b) show the transmission of spin-up and spin-down electrons, respectively, under the parallel magnetic configuration of the two electrodes. (c) and (d) show the transmission of spin-up and spin-down electrons, respectively, under antiparallel magnetic configuration of the two electrodes.

the projection of $T^{\sigma}(E_{\mathrm{F}})$ on the (k_x, k_y) plane, i.e.,

$$T^{\sigma}_{P/AP} = \frac{1}{N^2} \sum_{\mathbf{k}_{//}} T^{\sigma}(E_{\mathrm{F}}, \mathbf{k}_{//}) \tag{3.1}$$

where σ denotes spin state. The summation is carried out over the entire in-plane **k**-space and normalized by the number of sampling points ($N \times N$, with N chosen to be 31 in the present study). Results of our calculations (Fig. 3.3) show that, in the parallel magnetic configuration of the two electrodes, highly conductive channels are available over almost the entire $\mathbf{k}_{//}$space for the majority-spin electrons, while the conductive channels for the minority-spin electrons are limited to a small region near the Γ point. This is consistent with the calculated transmission spectra shown in Fig. 3.2(a). In the antiparallel magnetic configuration, however, both the spin-up and spin-down transmission channels are almost blocked. Therefore, the all-Heusler junction can function as a spin valve. It should be pointed out that the reason for the finite transmission, instead of being absolutely blocked, in both the parallel minority and the anti-parallel cases as presented in Figs. 3.3(b)-3.3(d) should be addressed to the induced minority interfacial states, which decrease the spin polarization from the bulk value of 100% to 87.6%,[71] and provide the possibility of minority electron diffusion between the two electrodes.

The optimistic and pessimistic magnetoresistances of the device are estimated based on the calculated transmission spectra as follows:

$$MR\%(optimistic) = \frac{T_P - T_{AP}}{T_{AP}} \times 100\% = \frac{(T_P^{\uparrow} + T_P^{\downarrow}) - (T_{AP}^{\uparrow} + T_{AP}^{\downarrow})}{T_{AP}^{\uparrow} + T_{AP}^{\downarrow}} \times 100\% \tag{3.2}$$

$$MR\%(pessimistic) = \frac{T_P - T_{AP}}{T_{AP+T_{AP}}} \times 100\% = \frac{(T_P^{\uparrow} + T_P^{\downarrow}) - (T_{AP}^{\uparrow} + T_{AP}^{\downarrow})}{T_P^{\uparrow} + T_P^{\downarrow} + (T_{AP}^{\uparrow} + T_{AP}^{\downarrow})} \times 100\% \tag{3.3}$$

where T_P and T_{AP} are the transmission coefficients in the parallel and antiparallel magnetic configurations, respectively. The theoretical optimistic MR ratio is $\sim 10^6\%$ and the pessimistic MR ratio is 99.96% which are very high for a GMR device. This is due to the highly conductive transmission channels under the parallel magnetic configuration of the electrode and almost complete block of transmission channels for both majority and minority spin electrons when the magnetization of the electrodes are antiparallel.

We also calculated bias-dependent transmission curves of the GMR device and obtained its spin-resolved current-voltage characteristics. The spin-polarized current through the system is calculated from the Landauer-Buttiker formula:

$$I^{\uparrow(\downarrow)}(E, V_b) = \frac{\mathrm{e}}{\mathrm{h}} \int_{-\infty}^{+\infty} \mathrm{d}E T^{\uparrow(\downarrow)}(E, V_b)[f_L(E, V_b) - f_R(E - V_b)] \tag{3.4}$$

where $f_{L(R)}(E, V_b) = n_F(E - \mu_{L(R)})$ is the Fermi distribution function, with $\mu_{L(R)}$ being the electrochemical potential of the left (right) lead, and $T^{\uparrow(\downarrow)}(E, V_b)$ is the spin-resolved transmission given by

$$T^{\uparrow(\downarrow)}(E, V_b) = \mathrm{Tr}[G^r_{\uparrow(\downarrow)}(E, V_b)\Gamma_{\mathrm{L}}(E, V_b)G^a_{\uparrow(\downarrow)}(E, V_b)\Gamma_{\mathrm{R}}(E, V_b)] \tag{3.5}$$

where $\mathrm{G}^{r(a)}_{\uparrow(\downarrow)}(E, V_b)$ is the retarded (advanced) Green's function, and $\Gamma_{(\mathrm{L,R})}(E) = i(\Sigma^r_{(\mathrm{L,R})}(E) -$

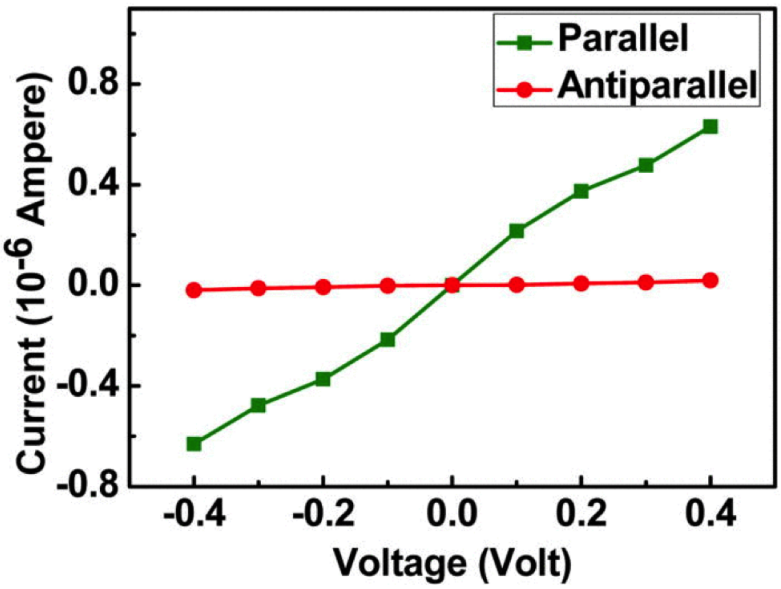

Figure 3.4: Calculated $I-V$ curves of the $Co_2CrSi/Cu_2CrAl/Co_2CrSi$ GMR junction.

$\Sigma^{a}_{(\mathrm{L,R})}(E))$ describes the level broadening due to coupling to the left and right electrodes expressed in terms of the electrodes self-energies $\Sigma_{(\mathrm{L,R})}(E)$. The NEGF-DFT self-consistency is controlled by a numerical tolerance of 10^5 eV.

As shown in Fig. 3.4, the calculated currents under the parallel and antiparallel magnetization configurations of the two electrodes show a large disparity. The magnitude of the current in the parallel configuration of electrodes is several orders of magnitudes larger than that in the antiparallel configuration at a given bias voltage. The calculated $I-V$ characteristics confirm that the $Co_2CrSi/Cu_2CrAl/Co_2CrSi$ device can function as a good spin valve.

The promising spin valve property of the $Co_2CrSi/Cu_2CrAl/Co_2CrSi$ device can be attributed not only to the good lattice and band-structure matching at the Co_2CrSi and Cu_2CrAl interface, but also to the nearly 100% spin-polarization of charge carriers, both

in the bulk and at the FM/NM interface, in the all-Heusler electrodes and spacer architecture. According to the Valet and Fert Model, in the $Co_2CrSi/Cu_2CrAl/Co_2CrSi$ device, the bulk spin-asymmetry β is largely enhanced by the extremely high spin-polarization of the all-Heusler alloy structure. Furthermore, the good match of spin-up band structures, which accounts for high transmission of majority-spin electrons across the interface, results in enhanced interface spin-asymmetry γ.[71] Therefore, compared with Heusler/TM interfaces which are widely used in current GMR devices, the all-Heusler Co_2CrSi/Cu_2CrAl interface proposed here is expected to have a much improved performance due to the larger ΔRA. In the next section, we will further carry out a more comprehensive study to provide a direct comparison between the all-Heusler scheme and the state-of-the-art GMR stack with a silver spacer, and to shed more light on the physical origin of the superiority of the all-Heusler architecture.

3.2.2 The advantage of the all-Heusler design scheme: A general study

Figure 3.5 shows the model of the CMS/NNS/CMS trilayer being studied. The tetragonal supercell includes two CMS electrodes of 12 atomic layers each, and a NNS spacer of 16.7 Å, i.e., 13 atomic layers. Due to the fact that the GMR stack with the silver spacer shows the best MR properties in the state-of-the-art Heusler/TM/Heusler system,[155, 156] for comparison, we carried out similar calculation on the CMS/Ag/CMS system with approximately the same spacer thickness (9 atomic layers of Ag). The MnSi/NiNi or MnSi/Ag interface termination was shown to be energetically stable compared to other terminations and is assumed here. The optimized lattice constants of bulk CMS and

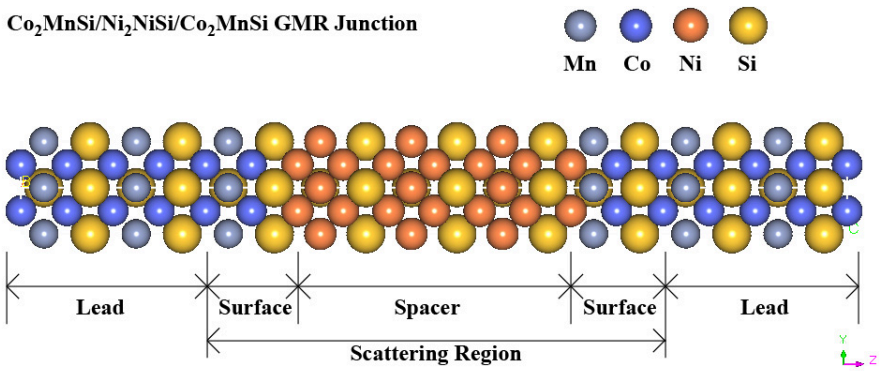

Figure 3.5: A schematic device model of the $Co_2MnSi/Ni_2NiSi/Co_2MnSi$ giant magnetoresistance junction.

NNS are 5.65 Å and 5.61 Å , respectively, leading to only 0.7% mismatch, which is even smaller than the case of CMS/Ag (5.78 Å, $\sqrt{2}a$) with 2.2% mismatch. The structure was optimized by relaxing the scattering region until the Hellmann-Feynman force on each atom is less than 0.01 eV/Å.

The calculated majority-spin band structures of CMS-NNS and, for comparison, CMS-Ag pairs are shown in Figs. 3.6(a) and 3.6(b), respectively, whereas the corresponding Fermi surfaces are presented in Figs. 3.6(c)-(e), respectively. Only the majority band matching between the electrode and spacer is discussed in this work (main text and Fig.3.6) because of the ideal half-metallic property of Co_2MnSi. Note that a finite conductance might appear in the minority-spin channel in real devices because of the atomic disorder and thermal fluctuation of magnetic moments. In contrast to the rather poor energy-band and Fermi-surface matching between CMS and Ag, the Fermi surfaces and the energy bands in the vicinity of Fermi levels of CMS and NNS almost coincide with each other. Such good matching would suppress the electron back-scattering at

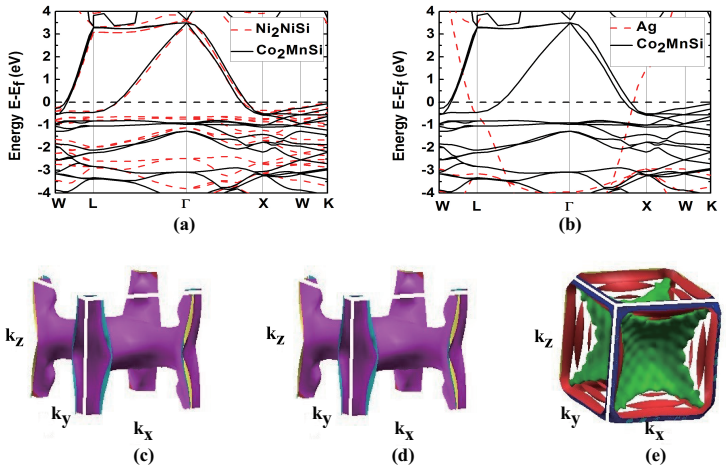

Figure 3.6: The majority-spin band structures of (a) CMS (black solid line) vs. NNS (red dashed line) and (b) CMS (black solid line) vs. Ag (red dashed line). The Fermi surfaces in the first Brillouin zones corresponding to the tetragonal unit cells of (c) $L2_1$-CMS, (d) $L2_1$-NNS, and (e) fcc-Ag plotted by XCRYSDEN.

the FM/NM interfaces in the majority channel, ensure a smooth propagation of majority electrons across the interfacial region, and consequently, enhance the interfacial spin-asymmetry coefficient (γ). Therefore, based on the Valet-Fert model,[11] the MR properties are improved in the all-Heusler devices.[72, 84, 156, 158]

To provide further evidence for good MR properties of the all-Heusler architecture and demonstrate its suitability for CPP-GMR application, we calculated the transmission spectrum and present in Fig. 3.7 the in-plane wave-vector $\mathbf{k}_{//}$-resolved transmission spectrum at the Fermi energy for the parallel majority spin within the CMS/NNS/CMS and CMS/Ag/CMS junctions. As can be seen in the figure, the majority transmission channel of the all-Heusler junction is largely enhanced in a vast region around the Γ point compared with that of the CMS/Ag junction. This significant enhancement of

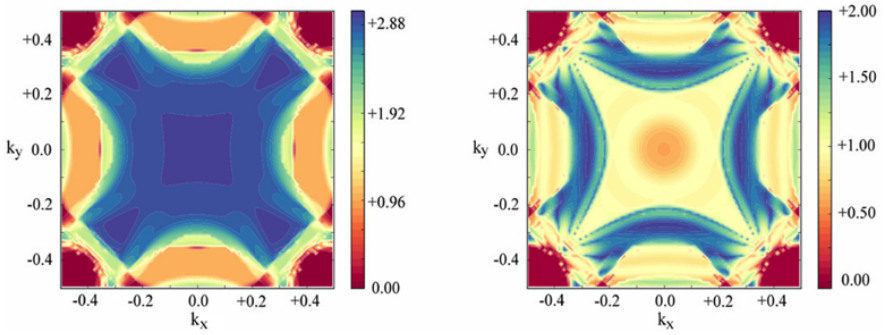

Figure 3.7: In-plane wave vector $k_{//}$=(k_x, k_y) dependence of the majority spin transmittance at the Fermi energy for (a) CMS/NNS/CMS and (b) CMS/Ag/
CMS GMR junction in the parallel magnetization configuration.

the transmittance in the parallel electrode magnetic configuration could be qualitatively attributed to the perfect Fermi surface match between the Heusler pair as shown in Fig. 3.6(c) and 3.6(d), since at the interface of well-crystallized metallic junctions, only those propagating states with their conserved in-plane wave-vector $\mathbf{k}_{//}$ coexisting within both metals can contribute to the conduction.[159] This is also confirmed by the fact that the area of enhanced transmittance and the zone where the Fermi surfaces of CMS and NNS overlap have the same shape.

The transmission mechanism stated above can be directly visualized and verified by the macroscopic conduction behaviours, e.g., the in-plane averaged voltage drop along the transmission direction (z-axis) of the whole junction, of which the results are illustrated in Fig. 3.8 for the all-Heusler (red dash line) and Heusler/TM (black solid line) junctions, both in the parallel magnetization configuration. It is noted that the drop is nearly linear throughout the all-Heusler stack, which behaves as a “homogeneous ”junction. However, the voltage across the CMS/Ag/CMS junction exhibits obvious heterogeneous

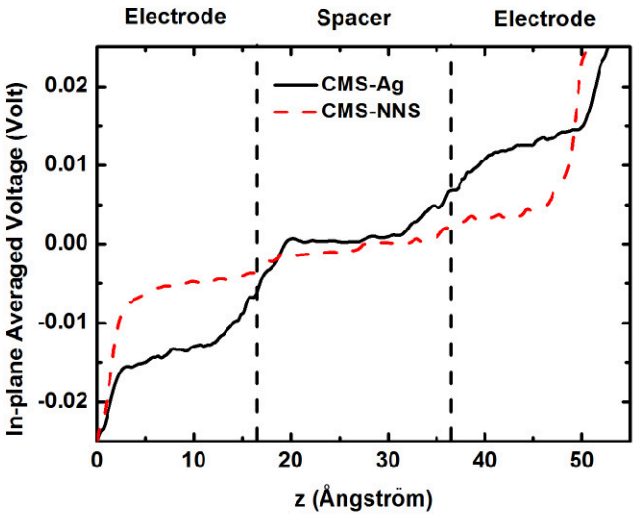

Figure 3.8: In-plane averaged voltage drop along the transmission direction (z-axis) across the all-Heusler (red dashed line) and Heusler/TM (black solid line) junctions. The vertical black dashed lines show the position of the FM/NM interfaces. It shows a smooth change of voltage drop at the interface of CMS/NNS, while a sharp change of CMS/Ag.

Table 3.1: The calculated conductance (Siemens) and RA product ($m\Omega{\cdot}\mu\mathrm{m}^2$) of CMS/NNS/CMS and CMS/Ag/CMS junctions.

Structure	G_P	G_{AP}	RA
CMS/NNS/CMS	6.71×10^{-4}	1.48×10^{-14}	0.24
CMS/Ag/CMS	2.34×10^{-5}	1.39×10^{-14}	6.28

characteristics, with a couple of step-like drops located right at the Heusler/TM interfaces, indicating comparatively heavier interfacial scattering for the majority conduction electrons. As a result, the interfacial spin-asymmetry coefficient (γ) is weakened, which, in turn, decreases ΔRA according to the Valet-Fert two-current model. This point can be quantitatively confirmed by the differences of the conductance and RA between the all-Heusler and Heusler/TM junctions, as listed in Tab. 3.1. The higher parallel interfacial conductance of the all-Heusler junction leads to a GMR ratio around 30 times larger than that of its Heusler/TM counterpart.

In-plane averaged voltage drop along the transmission direction (z-axis) across the all-Heusler (red dashed line) and Heusler/TM (black solid line) junctions. The vertical black dashed lines show the position of the FM/NM interfaces. It shows a smooth change of voltage drop at the interface of CMS/NNS, while a sharp change of CMS/Ag.

We also calculate self-consistently the bias-dependent transmission curves of the GMR devices and obtained their macroscopic current-voltage (I-V) characteristics. The currents through the two junctions under parallel and antiparallel electrode magnetization configurations are calculated based on the Landauer-Buttiker formula. As can be seen in Fig. 3.9, the antiparallel currents of the two systems show similar trends against the bias voltage, whereas for the parallel case, there is large disparity. The parallel current

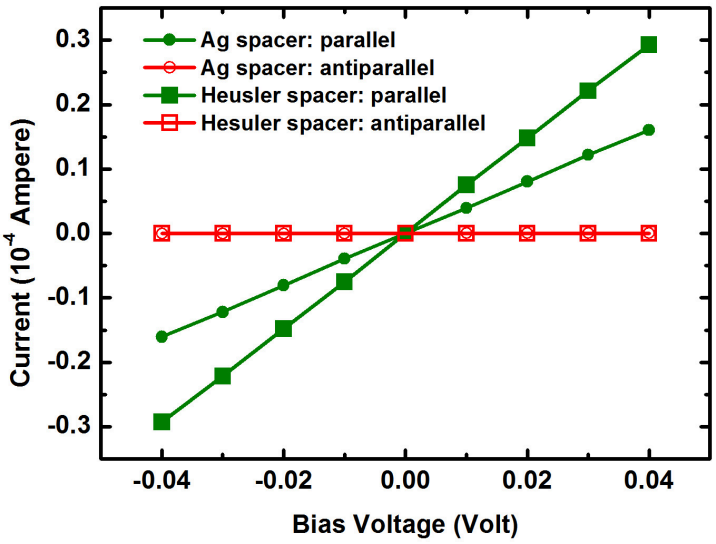

Figure 3.9: Calculated $I - V$ curves of the CMS/NNS/CMS and CMS/Ag/CMS GMR junctions.

of the all-Heusler junction is, unsurprisingly, much larger that of the Heusler/TM one, which can be attributed to its aforementioned smaller interfacial resistance. This explicitly confirms that the all-Heusler interfaces have much improved spin-valve performance compared with the widely-used Heusler/TM interfacial structure.

3.3 Chapter summary

In this chapter, we present an all-Heusler architecture for the rational design of high-efficiency CPP-GMR junctions for the HDD read heads. The intrinsic advantages of the all-Heusler stacking structure, i.e., the half-metallicity of the Heusler electrodes (large β) and the well matched energy bands and Fermi surfaces between the electrode-spacer

pair (large γ), lead to much improved MR properties, and hence much higher spin-filter efficiency. It should be noted that we discuss the all-Heusler CMS/NNS junction only as a representative example of an optimum design scheme superior to the state of art. Further theoretical and experimental efforts, following the all-Heusler scheme, are strongly recommended in designing and fabricating well-crystallized non-magnetic Heusler compounds as the tag spacer materials which can well match the Co-based full-Heusler electrodes.

Chapter 4

Tunneling magnetoresistance: the role of crystalline symmetry in spin transport through magnetic tunnel junctions

4.1 Introduction

Parallel to giant magnetoresistance, the tunnel magnetoresistance (TMR) effect, another importance spintronics phenomenon, has been observed in magnetic tunnel junctions (MTJs).[160] MTJs have been used as key components of data storage devices such

as read heads of hard disk drives and recording bits of magnetic random access memories. Due to the interfacial spin polarization, the TMR value is very low in normal insulator-based MTJs. Around a decade ago, two groups predicted very high TMR values in MgO-based MTJ with (Co)Fe electrodes which were attributed to the electron coherent tunneling of the Bloch states with Δ_1 symmetry via a wave-function symmetry selection rule.[16–18] Soon after, TMR ratios as high as 200% was reported experimentally in (Co)Fe/MgO/(Co)Fe MTJs.[19, 20] Nevertheless, such TMR ratio is still much lower than the previously predicted value (up to 10,000%).[16–18] Theorists argue that interfacial roughness, interfacial resonance, oxidized metal/MgO interface and oxygen vacancy in MgO are likely the main causes for the low TMR ratio observed in the experiments because defects and diffusive scattering can strongly reduce the wave-function-symmetry-filtered tunneling current.[87–94] Based on these theoretical understandings, experimentalists make a technique improvement by introducing boron into the electrode. CoFeB electrode can reduce metal/MgO interfacial roughness,[95] hinder interfacial oxidation by inert boron,[96] and passivate oxygen vacancies in MgO through boron diffusion.[98–100, 167] Therefore, it seems *all* shortcomings that contribute to the low TMR in the (Co)Fe/MgO/(Co)Fe system can be removed using CoFeB electrodes. Following this approach, Lee *et al.*, recently reported a record high TMR ratio of 1,010% at 5 K in CoFeB/MgO/CoFeB MTJs.[96] This value, however, is still one order of magnitude lower than the theoretical prediction.[16–18] This raises the questions of whether there are other factors that contribute to the low TMR in the CoFeB/MgO-based MTJs, and whether the physical mechanism in the CoFeB/MgO-based MTJs is different from that in Fe/MgO- or CoFe/MgO-based MTJs.

Besides the questions on the physical mechanism, the crystal structure of the tunneling barrier is also not clear. For example, an interesting experimental observation is the phase transition of amorphous CoFeB into the epitaxial *bcc* phase of CoFe (without boron) near the interface upon annealing.[19, 95, 97, 98] However, it is still not clear what happens to the B atoms after being "pushed" out of the CoFeB electrodes by annealing, and how they would affect the spin-dependent transport of the MTJ.

In this chapter, we address these questions related to B dynamics in the CoFeB/MgO/CoFeB MTJs by carrying out a comprehensive first principles investigation on its phonon dispersion, electronic structure, and spin transport properties. Based on phonon spectra, we propose that $Mg_3B_2O_6$ (kotoite) is formed and stable due to B diffusion from electrodes to the thin MgO spacer. From MgO to kotoite, the crystal symmetry reduces from C_{4v} to C_{2v}, but the wave-function symmetry maintains a good matching, *i.e.*, $\Delta_1(\text{MgO}) \rightarrow \widetilde{\Delta}_1(Mg_3B_2O_6)$, and $\Delta_5(\text{MgO}) \rightarrow \widetilde{\Delta}_2(Mg_3B_2O_6)$. Our spin-dependent transport calculations predict a TMR value of 210% for the CoFe/$Mg_3B_2O_6$/CoFe MTJ, which is much lower than the ideal value predicted based on CoFe/MgO/CoFe MTJs but in good agreement with experimental values[97]. We conclude that the different TMRs in CoFe/$Mg_3B_2O_6$/CoFe and CoFe/MgO/CoFe MTJs are related to the different crystal symmetries of MgO and $Mg_3B_2O_6$. The strong scattering of the Δ_1-liked Bloch states in CoFe/$Mg_3B_2O_6$/CoFe weakens its tunneling transmission. Therefore, good matching of wave-function symmetry between the electrode and spacer is a necessary but not a sufficient condition for high TMR. Mismatching of crystal symmetry can be detrimental for high TMR. Furthermore, our calculations indicate that spin-dependent tunneling is very sensitive to the interfacial chemical bonding. Residual boron atoms, which remain at the interface due to insufficient annealing temperature, can reduce the coupling between the

Δ_1 states of the electrodes and spacer, and further reduce the tunneling conductance.

First-principles calculations were carried out within a pseudopotential plane-wave framework as implemented in the VASP code.[129] We adopted the generalized gradient approximation (GGA)[135] for the exchange and correlation functional. A plane-wave basis set, with a 500 eV kinetic energy cut-off, was used to expand the Kohn-Sham orbitals. A supercell consisting of $4\times2\times3$ unit cells was used for calculating the phonon dispersion which is sufficient to eliminate the coupling effect and only Γ point of k-mesh of $1\times\ 1\times\ 1$ was used for such large supercell. Both the lattice parameters and atom positions were fully relaxed using the conjugate gradient algorithm. A small force tolerance (1 meV/Å) was used in structural optimization in order to obtain accurate structure and the force-constant matrix, which is essential for calculation of phonon dispersion. The small displacement method was used for the calculation of the force constants,[161] in which atoms in the central unit cell are displaced from their equilibrium positions by 0.015 Å in directions $\pm$x, $\pm$y, and $\pm$z. The longitudinal optical-transverse optical splitting is not considered in the calculation. Besides the phonon dispersion of Mg-B-O, we also calculated eigenvalues of CoFe/MgBO/CoFe MTJs to confirm the stability of the device structure. The in-plane lattice constants of the model were constrained to the values of CoFe, while the out-of-plane lattice parameter was fully relaxed to release the stress in the structure. Device optimization and quantum transport calculations were carried out within the framework of density functional theory combined with non-equilibrium Green's function method, as implemented in the ATK package.[131, 132] The GGA was adopted for exchange and correlation functional and the double-ζ polarized basis set was used for expanding the electron wave function. A

cutoff energy of 150 Ry and a Monkhorst-Pack k-mesh of 6$\times$ 6$\times$ 100 were used as previous calculations,[162–164] which can yield a good balance between the computational time and accuracy in the results of the transport calculation.

4.2 Results and discussion

While directly experimental evidence is insufficient to conclude what happens to the B atoms near the interface after annealing, our study on the crystal structure is based on the following experimental demonstrations. First, B-free crystalline CoFe was observed at the interface after annealing.[97–100, 165, 166] Second, there has been experimental evidence for diffusion of boron atoms from amorphous CoFeB to the MgO spacer layer.[97–100] Furthermore, X-ray absorption spectroscopy showed 4-fold coordinated boron at the interface,[98] and K-edge EELS data indicated possible formation of polycrystalline Mg-B-O after annealing when the spacer layer is less than 2 nm thick.[97] Nevertheless, the exact chemical composition and crystal structure of Mg-B-O in the spacer are unknown. On the other hand, Mg-B-O is known to exist in three stable phases in nature, monoclinic or triclinic $(MgO)_2B_2O_3$ (suanite) and orthorhombic $(MgO)_3B_2O_3$ (kotoite). These are natural starting points for our investigation to find a possible crystal structure of the spacer layer in the annealed CoFe/Mg-B-O/CoFe MTJs.

To evaluate the thermal stability of each phase of Mg-B-O sandwiched between two CoFe electrodes, we first carried out a phonon dispersion analysis. The calculated phonon dispersions along the various symmetry directions of all three naturally stabled bulk Mg-B-O structures ($(MgO)_x(B_2O_3)$ (x=2,3)) are shown in Fig. 4.1. As mentioned

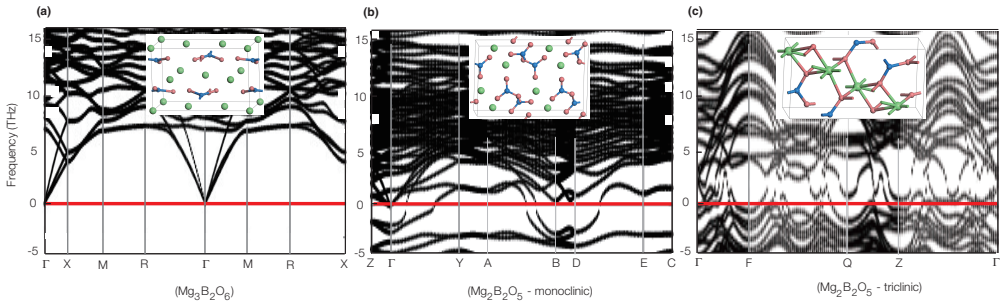

Figure 4.1: Calculated phonon dispersion for (a) $Mg_3B_2O_6$, (b) monoclinic $Mg_2B_2O_5$, and (c) triclinic $Mg_2B_2O_5$, respectively. The optimized geometric structures are shown in the insets. The in-plane lattice constants are constrained to those of bulk CoFe electrodes (a=4.095 Å; b=8.190 Å) while that in the normal direction is optimized (c=5.88 Å, 3.038 Å, and 4.155 Å

of kotoite, monoclinic suanite and triclinic suanite, respectively). Imaginary phonon frequencies (of unstable modes) are represented as negative values.

above, the in-plane lattice parameters of Mg-B-O were constrained to those of CoFe while that in the transport direction was relaxed in our calculation to mimic a thin MgO or Mg-B-O layer grown on CoFe. It is clear that one of the acoustic branches of both monoclinic (Fig. 4.1b) and triclinic (Fig. 4.1c) $Mg_2B_2O_5$ is imaginary over wide ranges of the Brillouin zones, indicating that the $Mg_2B_2O_5$ phases are not stable when sandwiched between CoFe electrodes. In contrast, no imaginary frequency is found in the entire Brillouin zone for orthorhombic $Mg_3B_2O_6$ (Fig. 4.1a). We also calculated phonon frequencies of the CoFe/Mg-B-O/CoFe devices, not only the Mg-B-O bulk. The fact that all calculated frequencies in the CoFe/$Mg_3B_2O_6$/CoFe structure are real confirms that among the three possible phases of Mg-B-O, $Mg_3B_2O_6$ is more likely to form between the CoFe electrodes following annealing of the CoFeB/MgO/CoFeB structure. The excellent thermal stability of orthorhombic $Mg_3B_2O_6$ is expected because its lattice

constants match well to those of MgO (0.1% mismatch along the *b*-axis and 6% along the *c*-axis, respectively), and correspondingly to those of CoFe. Furthermore, some experiments do suggest that the boron concentration in the Mg-B-O regions is about 5-10%.[97, 167] This favors $Mg_3B_2O_6$, as it has the lowest boron concentration (18%) among the three magnesium borates. Some other experimental supports include the XPS results of a highly oxidized state B^{3+} and the NEXAFS results of 4-fold coordinated B in the compound.[99, 100] Therefore, on the basis of these experimental evidences and our phonon dispersion analysis, we propose that the *thin* MgO spacer is transformed into $Mg_3B_2O_6$ after the CoFeB/MgO(thin)/CoFeB MTJ is annealed, due to B diffusion into MgO.

From the device performance point of view, a *thin* insulating spacer layer is desired for MTJs which leads to low resistance-area (RA) product that is compatible to other elements in the same device. The thickness of the MgO spacer layer in current industry products is about 1-2 nm which results in an RA of 0.1-100 $\Omega{\cdot}\mu m^2$. Therefore, we included a MgO or $Mg_3B_2O_6$ spacer of around 1.5 nm thick in our models to study the spin-dependent transport of the CoFe/MgBO/CoFe junctions. The calculated tunneling conductance, TMR ratio and RA product of the CoFe/MgBO/CoFe MTJ are given in Table 4.1, along with available experimental values for reference. For the purpose of comparison, we also calculated these qualities of the well-studied CoFe/MgO/CoFe MTJs in Table. 4.1. In agreement with previous predictions[18], the calculated TMR ratios of CoFe/MgO/CoFe junctions are about two orders of magnitude higher than the respective measured values[19, 20]. Interestingly, the calculated tunneling conductance ($G_{\uparrow\uparrow}$) of CoFe/MgBO/CoFe is much lower than that of CoFe/MgO/CoFe and in quite good agreement with the observed experimental value[97], while $G_{\uparrow\downarrow}$ is similar. This

Table 4.1: Thickness of spacer (nm), calculated tunneling conductance (G) in various spin channels, TMR ratio (%), and RA product ($\Omega \cdot \mu m^2$) of CoFe/MgO/CoFe and CoFe/MgBO/CoFe junctions, respectively.

Junction	d	$G^{maj}_{\uparrow\uparrow}$	$G^{min}_{\uparrow\uparrow}$	$G^{maj}_{\uparrow\downarrow}$	$G^{min}_{\uparrow\downarrow}$	TMR	RA	Ref.
CoFe/MgO/CoFe	1.5	1.29×10^{-8}	5.20×10^{-13}	6.75×10^{-11}	6.75×10^{-11}	9440	-	this work
	1.5	-	-	-	-	10000	-	calculation Ref.[4]
CoFe/MgBO/CoFe	1.4	2.59×10^{-10}	4.06×10^{-10}	1.07×10^{-10}	1.07×10^{-10}	210	504	this work
	1.4	-	-	-	-	190	400	experiment Ref.[17]

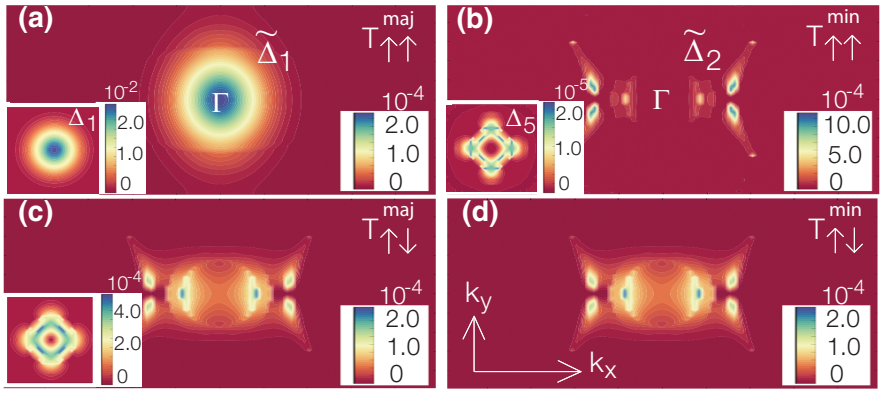

Figure 4.2: Spin-dependent transmission coefficient as a function of in-plane wave vector $\mathbf{k}_{//} = (k_x, k_y)$ of CoFe/MgBO/CoFe and CoFe/MgO/CoFe (inset) MTJs, respectively. (a) Majority-spin in the parallel magnetic configuration. (b) Minority-spin in the parallel magnetic configuration. (c) and (d) Majority-spin and minority-spin in the antiparallel magnetic configuration.

suggests that carriers (electrons) in the Δ_1 state are scattered in MgBO, but can easily tunnel through MgO[16–18].

In order to understand the difference between the spin transport performances of CoFe/MgBO/CoFe and CoFe/MgO/CoFe MTJs, we calculated the spin-dependent transmission coefficient and show it as a function of the in-plane vector $\mathbf{k}_{\|} = (\mathbf{k}_x, \mathbf{k}_y)$ in Fig. 4.2 for CoFe/MgBO/CoFe and CoFe/MgO/CoFe (inset). In the CoFe/MgO-based MTJs with the C_{4v} symmetry, the high TMR relies on symmetry selective filtering between CoFe and MgO. In particular, the majority carriers in the Δ_1 state (s, z, z^2) of CoFe couple efficiently with that in MgO, while the minority carriers only couple through the Δ_5 (x, y, xz, yz) and the Δ_2 $(x^2 - y^2)$ states, which decay much faster than Δ_1 [see the imaginary bands of Figure 4.3a][18]. In MgBO which has the C_{2v} symmetry, the majority carrier $\widetilde{\Delta}_1$ state (s, z, x^2, y^2, z^2) couples effectively with the Δ_1 state of CoFe, while the minority

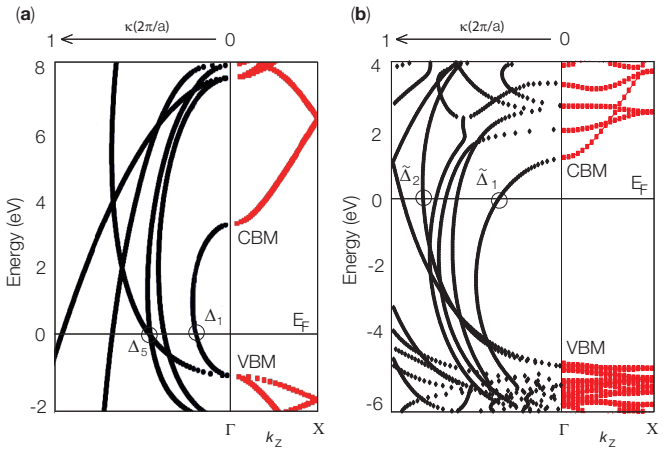

Figure 4.3: Calculated complex band structures of (a) MgO and (b) $Mg_3B_2O_6$. Both the real bands (red) and imaginary bands (black) are plotted.

carrier $\widetilde{\Delta}_2$ state (x, xz) couples only with the Δ_5 state of CoFe which decays very fast [see the imaginary bands of Figure 4.3(b)]. Therefore, $Mg_3B_2O_6$ has similar complex band structures and wave-function symmetries to MgO[168]. That is to say, the wave-function symmetry between CoFe and kotoite is conserved. However, the matching of wave-function symmetry is not a sufficient condition to get high TMR. Although MgBO and MgO have similar complex band structures and wave-function symmetries, the transmission coefficients of the $\widetilde{\Delta}_1$ and the $\widetilde{\Delta}_2$ states of MgBO are about two orders of magnitude lower than those of Δ_1 and Δ_5 states of MgO (see Figure 4.2). This suggests a strong scattering of the Δ_1 and Δ_5 states for both majority and minority carriers of the CoFe electrodes. The strong scattering of the Δ_1 and Δ_5 states in CoFe/MgBO/CoFe can be attributed to the crystal symmetry of MgBO. It is noted that the reduced crystal symmetry modifies the spatial distribution of wave function (asymmetrical dumbbell-shape of p_z of interfacial O atoms (see the shape of transmission eigenstates of the interfacial O atom in the CoFe/MgBO/CoFe junction)), but the symmetry matching of the wave

function ($\widetilde{\Delta}_1$ of MgBO and Δ_1 of CoFe) is not broken.

The strong scattering of both Δ_1 and Δ_5 states in CoFe electrodes can be understood based on the geometric structure and schematic density of states, as shown in Figure 4.4. The majority carriers in the CoFe electrodes are in the Δ_1 state, and the minority carriers are in the Δ_5 state. In the case of MgO, the Δ_1 state of MgO has a small decay rate, while the Δ_5 state has a large decay rate. Therefore, the majority carriers can tunnel through the MgO layer and reach the other electrode, while the minority carriers are blocked. In terms of wave function or band structure, the situation is essentially the same in the case of MgBO. That is, the $\widetilde{\Delta}_1$ state has a small decay rate while the $\widetilde{\Delta}_2$ state decays fast. However, the $\mathbf{k}_{//}$ tunneling transmission in MgBO is not conserved, as shown in Fig. 4.4(b). This is due to the C_{2v} symmetry of MgBO, which does not match the C_{4v} symmetry of the CoFe electrodes. In the case of MgO, both the CoFe electrode and MgO spacer have the same symmetry (C_{4v}) and thus the $\mathbf{k}_{//}$ tunneling is conserved (Fig. 4.4(c)).

A final remaining question in the experiment is the annealing-temperature dependence of TMR. The measured TMR ratio was around 190% when the MTJ was annealed at a higher temperature of 350 °C. But it was reduced to 90% when the junction was annealed at a lower temperature of 250 °C[97]. The reduced TMR ratio at the low annealing temperature could be due to residual B atoms at the interface as a result of insufficient annealing at the low temperature. To confirm this hypothesis, we considered two interface models with different chemical bonding environments. It can be expected that Fe-O bonds would dominate at the interface when the junction is thoroughly annealed at a high temperature, while at a low annealing temperature, there would be a large number of Fe-B bonds due to residual B atoms at the interface. We calculated the transmission

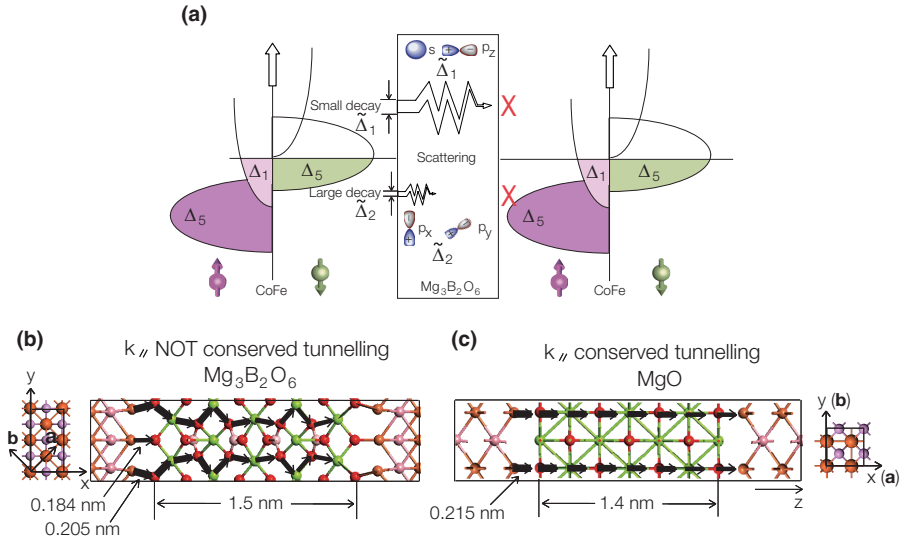

Figure 4.4: (a) Schematic diagram of the electron transmission in the CoFe/MgBO/ CoFe junction. The crystal symmetry mismatch strongly scatters both $\widetilde{\Delta}_1$ and $\widetilde{\Delta}_2$ states even the $\widetilde{\Delta}_1$ state having a small decay ratio compared to the $\widetilde{\Delta}_2$ state [see Fig. 4.3]. (b) & (c) The optimized structures of CoFe/MgBO/CoFe and CoFe/MgO/CoFe junctions. The small figures are the view along the transport direction (z). Note that there is a 45 degree rotation of the xy plane axis, resulting in a different side view of the electrode part. The black arrows schematically indicate that the $\mathbf{k}_{//}$ tunneling transmission is conserved in MgO with a C_{4v} symmetry (c), but is not conserved in MgBO with a C_{2v} symmetry (b). The latter results in a low MR ratio.

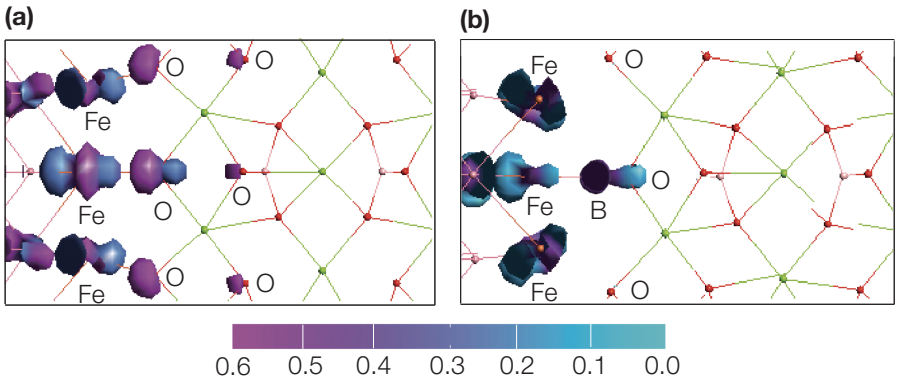

Figure 4.5: The transmission eigenstates of the CoFe/MgBO/CoFe junction with (a) Fe-O and (b) Fe-B interfacial bonding. The Fe Δ_1 Bloch states effectively couple with the MgBO $\widetilde{\Delta}_1$ evanescent states (p_z orbital of O) at the interface in the $\mathbf{k}_{//} = 0$ direction, while they are not at the Fe-B interface.

eigenstates of CoFe/MgBO/CoFe MTJs with Fe-O and Fe-B interfacial bonds, respectively, and show the results in Fig. 4.5. The transmission eigenstates are the eigenstates of the transmission matrix, which are obtained by propagating the linear combination of the Bloch states. Figure 4.5(a) shows a strong coupling between the Fe d_{z^2} and O p_z orbitals at the Fe-O interface. However, at the Fe-B interface, the coupling between Fe and O is weak due to trapping of the electrons density at B and surrounding Fe atoms, as shown in Fig. 4.5(b)[169]. This weakens the tunneling of the Δ_1 states at the interface, and accordingly reduces the TMR ratio significantly. Based on our model calculation, the TMR ratio is reduced from 210% for the MTJ with Fe-O interface bonding to 55% for the MTJ with interfacial B. Therefore, we can conclude that residual boron atoms at the interface, due to low annealing temperature, weakens the interfacial coupling of the Δ_1 states and results in further reduction of TMR.

4.3 Chapter summary

In this chapter, based on information provided by recent experiments and our phonon dispersion analysis on existing structures of Mg-B-O, $Mg_3B_2O_6$ is identified as the only stable phase of the spacer after annealing the CoFeB/MgO(thin)/CoFeB junction. TMR ratio derived from spin-dependent transport calculation based on the CoFe/MgBO/CoFe structure is in good agreement with measured value. The previously proposed mechanism of low TMR in (Co)Fe/MgO/(Co)Fe MTJs is not suitable for CoFeB/MgO-based MTJs. New physics is proposed which ascribes the low TMR to the crystal symmetry reduction which is induced by the boron diffusion during annealing. This leads to a strong scattering of the $\mathbf{k}_{//}$ transmission. Furthermore, residual boron atoms at the interface, due to insufficient annealing temperature, can further reduce the TMR. As a final remark, it has been noted that $Mn_{3-x}Ga$ ($0 \leq x \leq 1$) and $Mn_{3-x}A_xGa$ (A=Fe, Co and Ni) compounds which have been proposed recently as promising electrode materials of MgO-based spin-transfer torque devices, might be better than CoFe(B)electrodes, due to their high spin polarization, high Curie temperature, good lattice match with the MgO barrier, and most remarkbly, the perpendicular magnetic anisotropy. [70, 157, 170, 171]. The next chapter will be dedicated to a detailed discussion of binary compounds $Mn_{3-x}Ga$ and the evaluation of their suitability as FM electrodes of spin-transfer torque devices.

Chapter 5

The $Mn_{3-x}Ga$ compounds and their application in spin-transfer-torque magnetic random access memories

5.1 Introduction

Following the theoretical work on the tunneling magnetoresistance in Chapter 4, we move to its application aspects in Chapters 5 and 6. Perpendicular magnetic tunnel junctions (p-MTJs), with perpendicular magnetization easy axes, have recently attracted considerable interest due their potential for realizing next-generation spin-transfer-torque magnetic random access memories (STT-MRAMs) with high thermal stability and low critical current for the current-induced magnetization switching.[172, 173] However,

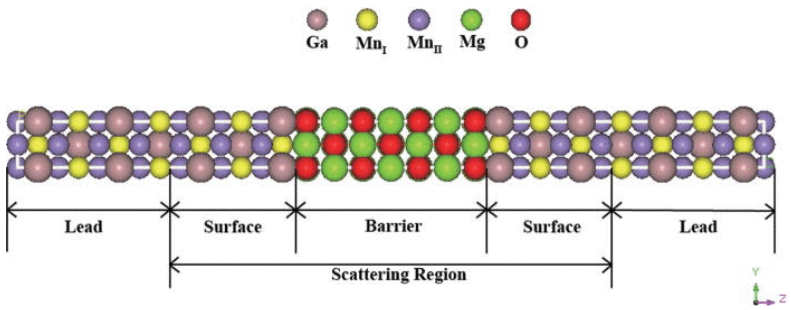

Figure 5.1: A schematic device model of Mn_3Ga/MgO/Mn_3Ga magnetic tunnel junction.

conventional perpendicular ferromagnets (FMs) containing noble-metal (4/5*d*) or rare-earth elements (*f*), such as $L1_0$-FePt, are not ideal electrode materials for p-MTJs because of the large Gilbert damping constants (e.g., $\alpha_{\text{FePt}} = 0.3$), which inevitably leads to high switching current density, and in turn, huge power consumption.[174, 175]. To overcome this barrier, searching for soft perpendicularly magnetized materials/ heterostructures as electrodes for the device is an essential step. Recently, it has been proposed that compensated ferrimagnets, for instance, $Mn_{3-x}Ga$ ($0 \leq x \leq 1$) compounds with DO_{22} tetragonally distorted Heusler-like phase possess a perpendicular easy axis. In addition, the combination of high spin-polarization, high Curie temperature, small damping constant and low magnetization is another factor which makes $Mn_{3-x}Ga$ appealing materials as the FM functional elements for p-MTJs.[110–112] Recent experimental efforts have been made on the demonstration of tunneling magnetoresistance (TMR) effect within the epitaxially grown magnetic tunnel junctions (MTJs) using $Mn_{3-x}Ga$ compounds as electrodes.[70] However, a systematic *ab initio* transport calculation is missing so far to investigate the magnetic and tunneling properties of the $Mn_{3-x}Ga$-based MTJs, which is indispensable to evaluate the suitability of these potential candidate materials for p-MTJs.

In this chapter, this question is addressed by employing Mn_2Ga (x=1) and Mn_3Ga (x=0), coupled with the typical MgO spacer, to construct Mn_2Ga/MgO/Mn_2Ga (001) and Mn_3Ga/MgO/Mn_3Ga (001) epitaxial trilayer MTJ-like structures. It has been found that, in view of magnetoresistance performance, only $Mn_{3-x}Ga$ compounds with low Mn concentration are promising candidate materials to serve as the electrodes of spin-transfer torque devices. The theoretical model of the latter stack is shown in Fig. 5.1, whereas the former one is achieved merely by removing all the type I Mn atoms out of the structure. The interfacial architecture with the Mn-Ga layer on top of oxygen atoms is verified as the most energetically favored one among all the possible $Mn_{3-x}Ga$/MgO interfaces. Experimental in-plane lattice parameters (a=3.909 Å for Mn_3Ga and a=3.905 Å for Mn_2Ga) are used for both cases. Geometry optimization is done by relaxing the scattering region until the force on each atom is less than 0.01 eV/Å . Density functional theory embedded in the VASP code is used for the electronic structure calculation,[129, 130] whereas non-equilibrium Green's function combined with DFT implemented in the ATK package is utilized for the MTJ transport simulation.[131, 132] Spin-polarized generalized gradient approximation (SGGA) proposed by Perdew et al. is utilized for the exchange and correlation functional consistently throughout this work.[135] For the transmission calculation, the double-ζ polarized basis set is used to expand the electron wave function. A cutoff energy of 75 Ry and a Monkhorst-Pack [138] **k**-mesh of $8 \times 8 \times 100$ yield a good balance between computational time and accuracy in the results.

5.2 Results and discussion

The magnetic anisotropy of Mn_2Ga and Mn_3Ga thin films is testified by the non-collinear DFT with spin-orbit interaction (SOI) taken into consideration. The magnetic anisotropy energy, $E_{MAE} = E(m_\perp) - E(m_{//})$, where $E(m_\perp)$ and $E(m_{//})$ represent the total energy of the system with perpendicular-to-plane and in-plane magnetization, is calculated for both Mn_2Ga and Mn_3Ga compounds. It is found that E_{MAE} is -1.28 meV/unit-cell for the former and -2.76 meV/unit-cell for the latter, which indicates perpendicular magnetic anisotropy (PMA) for both the materials and consists with the previous experimental results.[111, 112] Additionally, based on our calculation, the PMA is preserved when the scale of both materials increases to bulk size, which eliminates the possibility of surface effect.

With respect to the MTJ transport performance, the calculated spin-resolved $\mathbf{k}_{//}$-dependent transmission probability at the Fermi energy (E_F) is shown in Figs. 5.2(a)-5.2(d) for Mn_2Ga/MgO/Mn_2Ga and 5.2(e) and 5.2(f) for Mn_3Ga/MgO/ Mn_3Ga structures, respectively. As can be seen in Figs. 5.2(a)-5.2(d), in the parallel magnetic configuration of two electrodes, the majority channel exhibits a rather broad and smooth peak centered at the Γ point with comparatively high transmission coefficient, whereas the minority one is only composed of some widely spread discrete spikes, which is referred to as hot-spot conductance originating from the effect of resonant interface states,[177] in the two-dimensional (2D) Brillouin zone. On the other hand, for the case of antiparallel magnetization alignment, the transmission pathway, similar to that of the parallel minority spin, is essentially blocked, bearing negligible tunneling probability. Based on the above transmission behavior, the investigated Mn_2Ga/MgO/Mn_2Ga acts as a promising

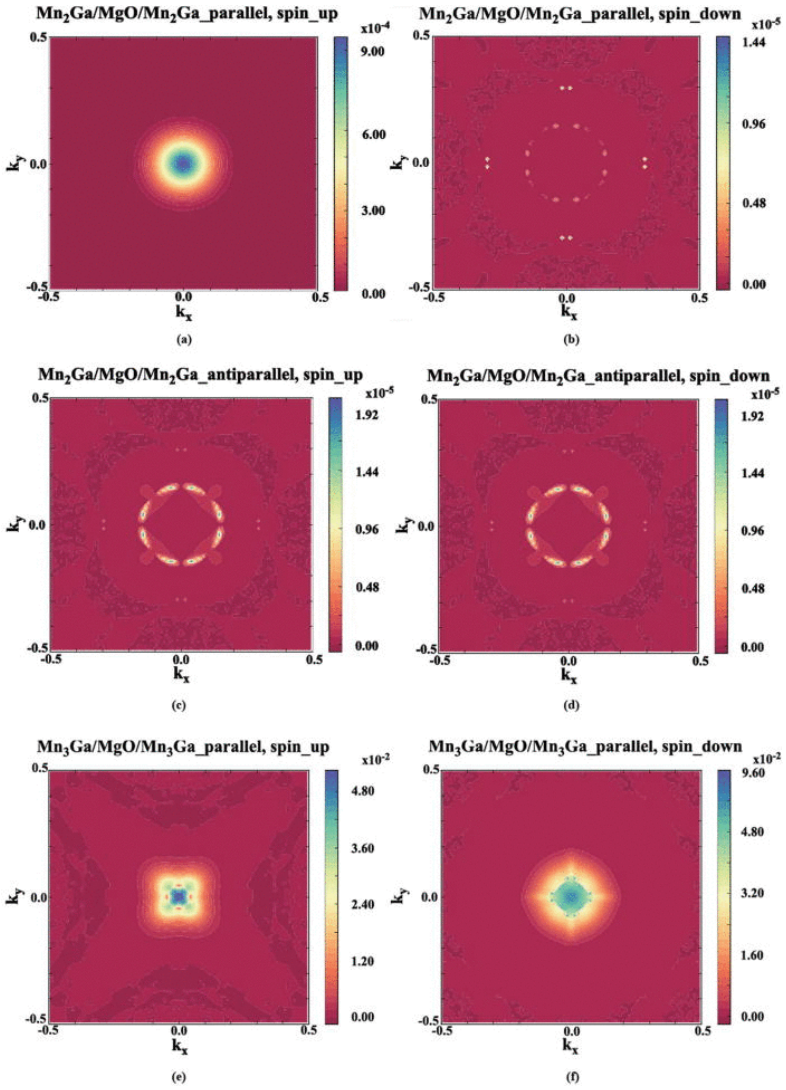

Figure 5.2: Spin-dependent transmission coefficient as a function of in-plane wave vector $\mathbf{k}_{//}$=(k_x, k_y) of Mn_2Ga/MgO/Mn_2Ga and Mn_3Ga/MgO/ Mn_3Ga MTJs. For the Mn_2Ga/MgO/Mn_2Ga MTJ, (a) and (b) show the transmission of spin-up and spin-down electrons, respectively, under parallel magnetic configuration of two electrodes. (c) and (d) show the transmission of spin-up and spin-down electrons, respectively, under antiparallel magnetic configuration of two electrodes. For the Mn_3Ga/MgO/Mn_3Ga MTJ, (e) and (f) show the transmission of spin-up and spin-down electrons, respectively, under parallel magnetic configuration of two electrodes.

MTJ, of which the optimistic TMR ratio was estimated using the following equation:

$$MR\%(optimistic) = \frac{T_P - T_{AP}}{T_{AP}} \times 100\% = \frac{(T_P^{\uparrow} + T_P^{\downarrow}) - (T_{AP}^{\uparrow} + T_{AP}^{\downarrow})}{T_{AP}^{\uparrow} + T_{AP}^{\downarrow}} \times 100\% \quad (5.1)$$

where T_P and T_{AP} are the total transmission coefficients when magnetization alignment of two electrodes are parallel and antiparallel, respectively. $T_{P/AP}^{\sigma}$, with σ denoting spin, the spin-dependent transmission coefficient, *i.e.*,

$$T_{P/AP}^{\sigma} = \frac{1}{N^2} \sum_{\mathbf{k}_{//}} T^{\sigma}(E_{\mathrm{F}}, \mathbf{k}_{//}) \quad (5.2)$$

The summation is carried out over the entire in-plane $\mathbf{k}_{//}$- resolved space and normalized by the size of sampling mesh ($N \times N$, with N chosen to be 100 in our study). The theoretical MR ratio is as high as $10^3\%$ for the Mn_2Ga/MgO/Mn_2Ga MTJ. It is worth to mention that the calculated extremely large MR ratio of the MTJ with perfect modeling structure might be deteriorated in reality when various defects, impurities, and lattice distortions are induced.[70, 87–89]

As for the device with Mn_3Ga as electrodes, however, the transmission channels, when the electrode magnetization aligns in parallel, are open for both majority and minority electrons, regardless of their spin directions, leaving no spin filtering effect at all, as illustrated in Figs. 5.2(e) and 5.2(f). Since the whole series of $Mn_{3-x}Ga$ share lots of common promising magnetic features as reported,[110–112] the calculated transmission disparity between low and high Mn concentrations seems quite unexpected at first glance and, therefore, leads to further investigation on its origin.

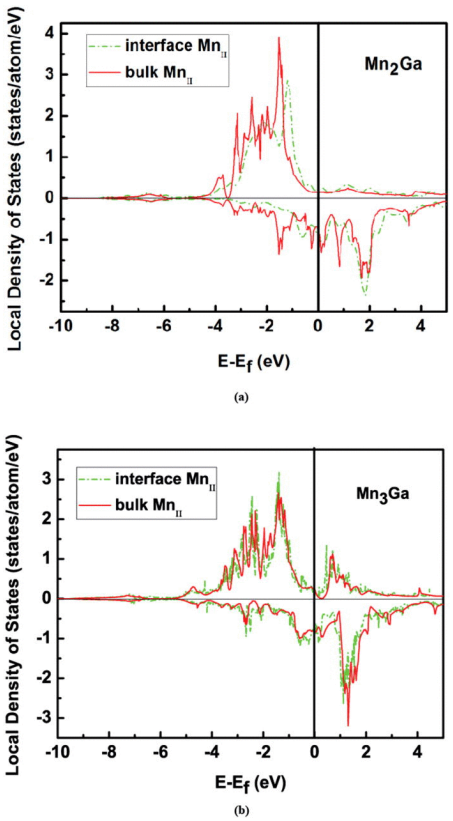

Figure 5.3: The spin-resolved LDOSs of the interfacial (marked as dash-dotted lines, green) and bulk (marked as solid lines, red) Mn atoms within (a) Mn_2Ga/ MgO/Mn_2Ga (001) and (b) Mn_3Ga/MgO/Mn_3Ga (001) MTJs.

This completely different transport behavior might be attributed to two possible reasons, among which the first one is due to the induced interfacial states which might kill the high spin-polarization at the Fermi level in the interfacial Mn_3Ga regions and, thus, break the filtering effect of the whole MTJ device. In order to examine this possibility, the spin-dependent local density of states (LDOSs) of the Mn atoms at Mn_2Ga/MgO(001) and Mn_3Ga/MgO(001) interfaces are calculated and presented as dash-dotted lines (green) in Figures 5.3(a) and 5.3(b). For comparison, the bulk LDOSs of the Mn atoms lying deeply in Mn_2Ga and Mn_3Ga electrodes are also shown as solid lines (red) in the same figures.

Spin polarization at the Fermi energy is calculated using the following formula:

$$P = \frac{n_{\uparrow}(E_{\mathrm{F}}) - n_{\downarrow}(E_{\mathrm{F}})}{n_{\uparrow}(E_{\mathrm{F}}) + n_{\downarrow}(E_{\mathrm{F}})} \times 100\% \tag{5.3}$$

where $n_{\uparrow(\downarrow)}(E_{\mathrm{F}})$ is the DOS of spin up (down) electrons at the Fermi level. It has been found, nonetheless, that there is no significant difference in the spin polarization at the Fermi energy between interfacial and bulk Mn atoms for both Mn_2Ga and Mn_3Ga cases. The interfacial polarization values are 67.95% for the former and 72.17% for the latter, which are comparable to those of bulk configurations, i.e., 68.09% and 72.96%. Such conservation of high spin polarization, in spite of good news for the transport performance of MTJ devices, has unfortunately made our first assumption insufficient to explain the absence of spin filtering effect in the Mn_3Ga/MgO/Mn_3Ga MTJ.

The other possible reason to interpret the entirely different performance between Mn_2Ga and Mn_3Ga electrodes is the symmetry selective filtering effect,[16, 17] which suggests

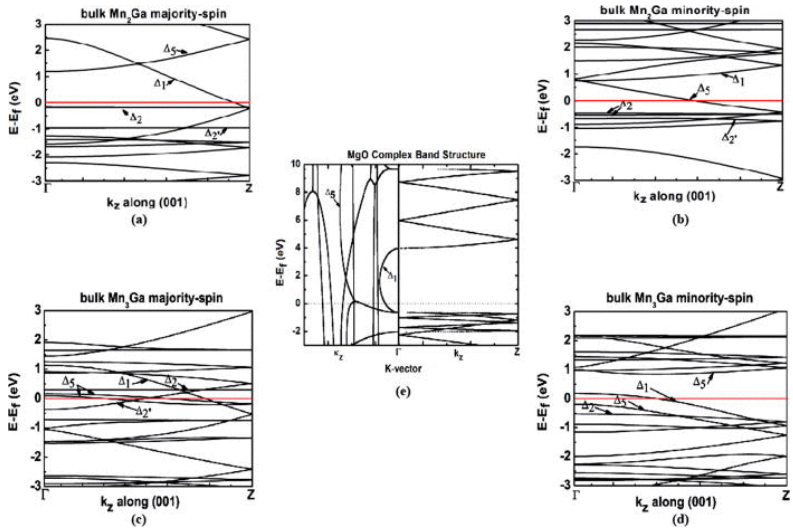

Figure 5.4: The majority- and minority-spin band structures of bulk (a)-(b) Mn_2Ga and (c)-(d) Mn_3Ga along (001) direction at $\mathbf{k}_{//}$=(0,0). (e) shows the complex band structure of MgO, where κ_z and k_z denote the magnitude of imaginary and real parts of the wave-vector of propagating Bloch states, respectively. The decay rates of a specified symmetry can be evaluated by the value of κ at which its corresponding band intersects the Fermi level.

that the incident propagating Bloch states from electrodes with different symmetries decay at different rates within the MgO barrier; the evanescent wavefunction bearing Δ_1 circle symmetry is confirmed to be attenuated much slower than those with Δ_5, Δ_2, or $\Delta_2^{'}$ symmetries,[168, 178] and therefore, it should be the Δ_1 conduction bands of the electrode material that dominates the tunneling behavior owing to the symmetry compatibility with the metal induced gap states (MIGSs) in the MgO complex band structure (CBS),[168, 179, 180] as illustrated in Fig. 5.4(e).

Aiming at verifying this presumption, the band structures of bulk Mn_2Ga and Mn_3Ga along the transmission direction (001) at $\mathbf{k}_{//}$=(0,0) are calculated and plotted in Fig. 5.4. Based on symmetry analysis, it is found that, in the Mn_2Ga case, only Δ_1 majority-spin and Δ_5 minority-spin conduction bands intersect the Fermi level, and hence, each of them contributes exclusively to their respect spin channels. According to the symmetry filtering effect stated above, the incident majority spins would tunnel through the MgO spacer with the least attenuation, whereas the minority spins have to encounter much tougher obstacles on their way and would be scattered heavily by the barrier. As a result, the quantity of majority spins reaching the opposite terminal of the device is several orders larger than that of the minority ones, leaving obvious filtering effect, which is consistent with the results shown in Figs. 5.2(a)-5.2(d).

With respect to Mn_3Ga, however, not only majority but also minority spins have Δ_1-symmetry conduction bands crossing the Fermi level, which causes the large transmission for electrons through both spin channels and, therefore, undermines the spin filtering effect of the Mn_3Ga/MgO/Mn_3Ga trilayer stack. Additionally, from Figs. 5.4(c) and 5.4(d), it can be seen that, unlike the minority spin channel which merely consists of the

Δ_1-symmetry wavefunction, the majority channel of Mn_3Ga electrodes also comprises the fast-decaying Δ_2 and $\Delta_2^{'}$ components, which, consequently, leads to the smaller transmission possibility of the majority spin than that of the minority one, as shown in Figs. 5.2(e) and 5.2(f). Eventually, we may reach to the conclusion that Mn_2Ga, or $Mn_{3-x}Ga$ with low Mn content ($x \rightarrow 1$), should be more eligible for p-MTJ electrode materials than those with high Mn content ($x \rightarrow 0$) with respect to the TMR performance.

5.3 Chapter summary

In this chapter, we show by first-principles electronic-structure and spin transport calculation that the Mn_2Ga/MgO/Mn_2Ga trilayer stacking structure behave as a good MTJ with high TMR ratio, whereas the Mn_3Ga/MgO/Mn_3Ga stack exhibits no spin filtering effect at all. The entirely different performance can be explained by the symmetry selective filtering effect. Combined with its perpendicular easy axis, small Gilbert damping constant and other promising magnetic properties, $Mn_{3-x}Ga$ with low Mn content ($x \rightarrow 1$), should be good materials to serve as electrodes of the p-MTJ functional element embedded in spin-transfer torque devices.

Chapter 6

Electric-field-assisted magnetization switching in Heusler-compound-based perpendicular magnetic tunnel junctions

6.1 Introduction

In addition to direcly searching for soft perpendicular materials as discussed in Chapter 5, perpendicular magnetic anisotropy (PMA) can also be realized in soft ferromagnet (FM)/oxide heterostructures by interfacial hybridization effects. In particular, PMA was demonstrated by combining ultra-thin CoFeB eletrodes, a soft $3d$-ferromagnet

($\alpha_{\mathrm{CoFe}} = 0.01$), with the MgO barrier, opening a novel avenue for realizing low-power p-MTJs with small switching current density.[173] However, the damping constant of the CoFe(B) film increases rapidly with decreasing film thickness [173]. Therefore, to seek soft $3d$-FMs with intrinsic small α as well as large interfacial PMA on oxides remains as one big challenge.

An alternative way to reduce writing current is to take advantage of electric-field-assisted switching which has been witnessed in CoFeB/MgO/CoFeB [113] and all-oxide composite [114–116] MTJs. In fact, electric-field control of magnetization is significant not only in sense of energy-efficiency, but also because of the compatibility with the current ubiquitous voltage-controlled semiconductor devices. The magnetoelectric (ME) effect has been widely studied in various systems both experimentally and theoretically. [113, 117–128, 181, 182] The efficiency of the electric-field manipulation is quantitatively characterized by the magnetocrystalline anisotropy (MCA) coefficient, β, defined as $\Delta\mathrm{MAE} = \beta E$, where ΔMAE is the change in the MCA energy and E the applied electric field. Currently, FM/oxide interfaces show the best performance with the MCA coefficient ($\approx 10^{-8}$ erg/V cm), which is, nevertheless, still below the requirement of practical low-power applications. Therefore, to predict and identify novel FM/oxide interfaces with giant MCA coefficient is another big challenge for achieving low-power devices. Looking further ahead, to design FM/oxide/FM perpendicular magnetic tunnel junctions that simultaneously satisfy high thermal stability, low switching current density and desired magnetoresistance performance is in urgent demand but currently still absent.

In this chapter, we propose *cobalt-based full-Heusler compounds* to be used as the p-MTJ electrodes, in junction with the typical MgO spacer, and investigate the possibility of addressing all these challenges. Well-studied Co_2FeAl(CFA) is chosen as a representative example of the family in view of its small intrinsic damping constant ($\alpha_{\mathrm{CFA}} \approx 0.001$), small lattice mismatch with MgO (3.7%), and half-metallicity. [53] First, we map out a thermodynamic phase diagram of the CFA/MgO interface to examine its thermal stability in terms of chemical potential in the ambient condition. *Ab initio* atomistic thermodynamics analysis shows that the oxygen-top FeAl termination is the only possible interfacial geometry with its stability protected by the thermodynamic equilibrium limit. Second, a rather strong perpendicular magnetic anisotropy, with an MCA energy($K_{\mathrm{u}} \cdot t$) of 0.428 erg/cm^2, is found at the interface, which can compete with thermal fluctuation and enhance the robustness of the recorded magnetic configuration. Third, the CFA/MgO interface is found to manifest a giant magnetoelectric effect due to its high interfacial spin imbalance. The calculated MCA energy coefficient is around 10^{-7} erg/V cm, at least one order of magnitude higher than reported values.[128] The efficient electric-field control of magnetization is considered desirable in view of reducing the switching current of the p-MTJ elements. Finally, non-collinear spin transport calculations demonstrate enhanced magnetoresistance performance (much larger MR ratio) of the CFA/MgO/CFA p-MTJ compared with that of its conventional CoFe- or FePt-based counterparts. The combination of high thermal stability, low-power consumption, and good magnetoresistance performance makes the CFA/MgO/CFA p-MTJ an appealing building block towards the next-generation spin-based non-volatile memories, leading to enormous power savings, in addition to fast, nonvolatile, and ultra-long term data storage.

The electronic structure calculations were carried out within the framework of density functional theory as implemented in the Vienna *Ab-initio* Simulation Package.[129, 130] The projector augmented-wave (PAW) pseudopotential[143] and the generalized gradient approximation PBE (GGA-PBE) formalism of exchange and correlation functional[135, 136] were employed consistently throughout this work. A standard plane-wave basis set with a kinetic energy cutoff of 500 eV and a Monkhorst-Pack k-mesh[138] of $25 \times 25 \times 1$ sampling in the full Brillouin zone yielded a good balance between the computational time and accuracy. Geometry optimization was done until the Hellman-Feynman force on each atom was less than 1 meV/Å.

The non-equilibrium Green's function (NEGF) formulism, implemented in the Atomistix ToolKit package (ATK v13.8),[131, 132] was used for the non-collinear transport calculation of CFA/MgO/CFA p-MTJs. The electron wave functions was expanded in a double-ζ polarized basis set. A kinetic energy cutoff of 150 Ry was used for representing the density and potential, and a 100×100 Monkhorst-Pack **k**-point was used to sample the transverse Brillouin zone. We found such sampling size is large enough to achieve satisfactory convergence of conductance.

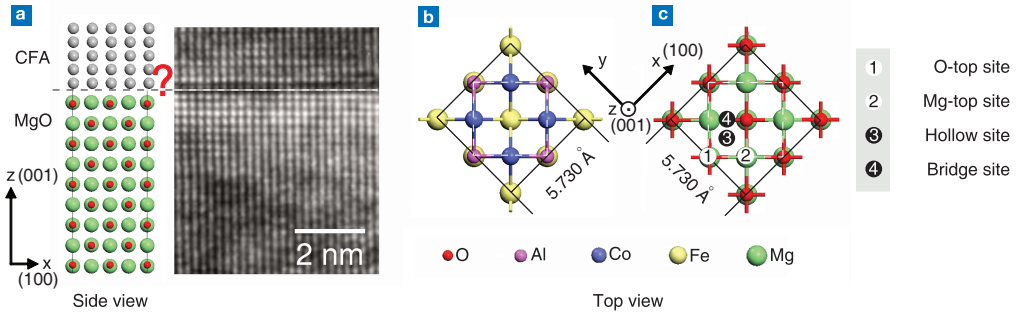

Figure 6.1: (a) Schematic structure and HRTEM image of the Co_2FeAl/MgO(001) interface, which can accurately reveal atomic position, but cannot identify the element of atoms at the interface. (b) and (c) shows atomic configuration of the frontier layers of CFA and MgO, respectively, residing at the interface. The unit cells are bounded by the white-dashed squares. The four different CFA termination registries relative to MgO are labeled by numbers 1 to 4. The in-plane lattice parameter of MgO is reduced by 3.7 % to match $1/\sqrt{2}$ of the experimental lattice parameter of bulk CFA (5.73 Å).

6.2 Results and discussion

6.2.1 Thermal stability of the Co_2FeAl (CFA)/MgO interface

It has been reported that the electronic structure, magnetic and spin-transport properties of the Heusler-compound-based MTJs are highly sensitive to the structural configuration of the Heusler-compound/MgO interfaces.[53, 184, 185] However, although high-resolution transmission electron microscopy can reveal a clear atomic-layer structure of the CFA/MgO interface, the exact atomic configuration of the interface cannot be recognized (see Fig. 6.1(a)).[186] In this sense, before carrying out any further calculations, we first examine the thermal stability of the interface and identify the robust structural

geometry. As shown in Figs.6.1(b) and 6.1(c), the CFA/MgO(001) interface has four possible types of terminations on CFA (by CoCo, FeAl, FeFe, and AlAl). Furthermore, each of these terminations has four possible registries relative to MgO(001), i.e., on top of the O atoms (O-top), on top of the Mg atoms (Mg-top), hollow and bridge sites. In our calculation, the CFA/MgO interfaces were modeled in a supercell geometry, using 9 monolayers (MLs) of MgO and 15 MLs of CFA for FeAl-, FeFe-, and AlAl-termination, and 17 MLs for the CoCo-case with one additional CoCo layer at both CFA/MgO interfaces. The DFT total energy is minimized by optimizing the atomic position, as well as the longitudinal size of the supercells. It reveals that, for the CoCo-, FeAl-, and FeFe-terminated CFA, the configuration of the O-top site is much lower in energy than others, whereas for the AlAl-termination, the Mg-top site is favored.

To further compare the thermal stability of these four possible stable interfaces (CoCo|O, FeFe|O, FeAl|O, AlAl|Mg), we use the $ab\ intio$ atomistic thermodynamics technique,[184, 187, 188] in correspondence to the experimental annealing/quenching process in the ambient condition. The interface formation energy, E_{f}, is calculated for the four interfacial structures:

$$E_{\mathrm{f}} = \frac{1}{2\mathrm{A}}[G_{\mathrm{hetero}} - G_{\mathrm{bulk}} - \sum_i n_i \mu_i] \tag{6.1}$$

where A is the cross-section area of a given CFA/MgO interface, G_{hetero} and G_{bulk} the Gibbs free energies of the heterostructure and appropriate amounts of bulk CFA and MgO, n_i counting the number of atoms in which the interface deviates from bulk composition, and μ_i the chemical potential of the element. In our models, the size of bulk MgO supercell is chosen to be exactly the same as that included in the interface. Thus, i only varies among Co, Fe and Al. Moreover, the interface is assumed to be in thermodynamic equilibrium with the bulk Heusler compounds, i.e., $\mu_{\mathrm{CFA}} = 2\mu_{\mathrm{Co}} + \mu_{\mathrm{Fe}} + \mu_{\mathrm{Al}}$,

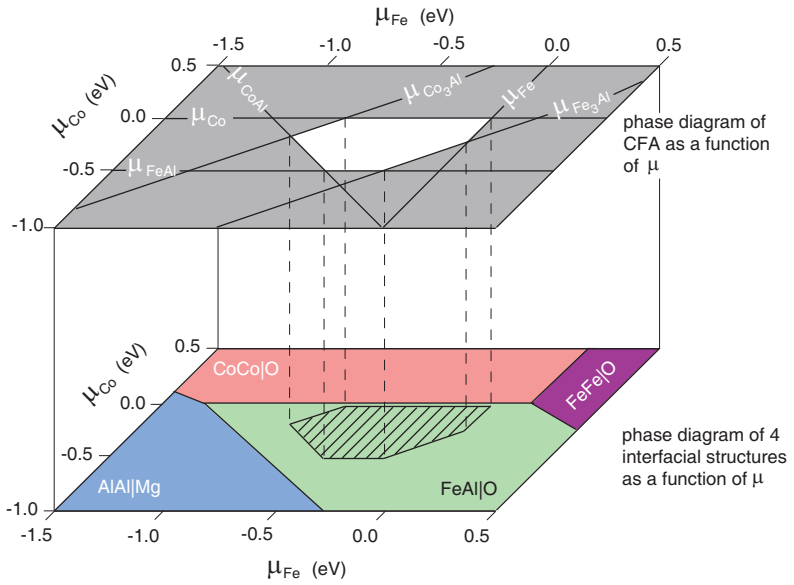

Figure 6.2: Phase diagram of Co_2FeAl (upper plane) and phase diagram of four possible stable interfacial structures (lower plane) as a function of chemical potentials of Co and Fe. The white hexagon indicates region accessible in thermodynamic equilibrium, and shaded area marks the most thermal stable interfacial structure (FeAl|O) under ambient conditions.

which allows us to further reduce the number of variable quantities to two, for example, the μ_{Co} and μ_{Fe} pair.

Since the interface formation energy is a free-energy difference, it is often a good approximation to calculate the formation energy E_{f} from the differences of total energies obtained by DFT calculations. This is the general idea behind *ab initio* atomistic thermodynamics. In this way, we calculate the formation energy and compare the relative stability of the four terminations. The calculated phase diagram of the epitaxial interfaces is shown in Fig. 6.2 as a function of chemical potentials of Co and Fe. The four colored regions in the lower plane of Fig. 6.2 correspond to the chemical-potential

ranges, in which each termination has the lowest formation energy, thus being stable. Moreover, the accessible chemical potential of CFA must be confined within the thermodynamic equilibrium boundaries with the bulk-phase *hcp*-Co, *bcc*-Fe, CoAl, Co_3Al, FeAl and Fe_3Al, i.e., the white hexagon bounded by the 6 lines in the upper plane of Fig. 6.2. When projected onto the four-color phase diagram, the entire accessible region falls in the FeAl|O area, which indicates that FeAl|O is the only configuration with its stability protected by the thermodynamic equilibrium limit. In experiments, CFA films are annealed under high temperature after deposition on a buffer layer in order to obtain the $L2_1$- or B2-ordered phase. In other words, the interface formation is governed by the aforementioned atomistic thermodynamics mechanism. In the following, we focus on this stable interface and discuss its magnetocrystalline anisotropy, magnetoelectric effect and magnetoresistance properties.

6.2.2 Perpendicular magnetocrystalline anisotropy

In addition to structural stability, the stability of magnetic configuration plays another key role in MTJ device performance. In particular, a high magnetic thermal stability factor $K_\mathrm{u} \cdot V/k_\mathrm{B}T$ ($K_\mathrm{u} \cdot V$ is the anisotropy energy barrier distinguishing two magnetization orientations and $k_\mathrm{B}T$ the thermal perturbation energy) over 40 is at least required for data retention over ten years on a bit level [189]. Under perpendicular magnetization condition, the stability can be enhanced against thermal fluctuation due to the PMA barrier. Therefore, we next check the magnetocrystalline anisotropy of the CFA/MgO interface. The MCA energy($K_\mathrm{u} \cdot t$) is obtained by taking the difference between the

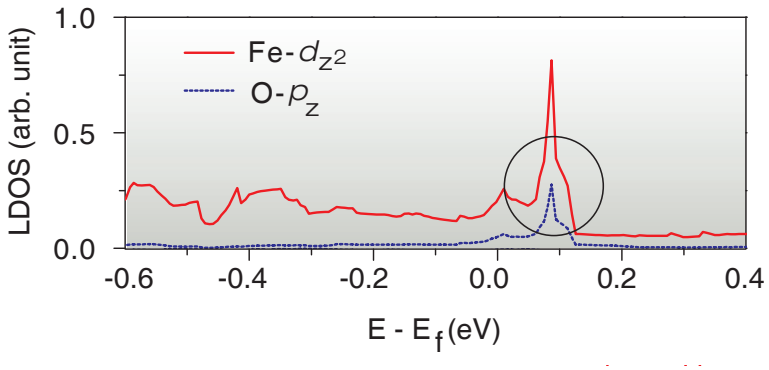

Figure 6.3: The local density of states projected onto the interfacial iron atom (red solid line) and the oxygen atom (blue dash line). The black circle indicates the hybridization states in the vicinity of the Fermi level which contributes to the perpendicular magnetocrystalline anisotropy.

total energy calculated within the force theorem corresponding to magnetization pointing along the in-plane (100) and out-of-plane (001) directions as shown in Fig. 6.1, i.e., $E(100) - E(001)$. Noncollinear DFT with spin-orbit coupling (SOC) was employed. Our calculation shows that PMA is energetically favored, with a rather strong interfacial MCA energy of 0.428 erg/cm^2, which is in good agreement with the available experimental report [190]. The origin of the PMA can be understood by the electronic structure in the vicinity of the Fermi level via the second order perturbation theory [123, 191–193],

$$E_{\mathrm{MCA}} \propto \xi^2 \sum_{\mathbf{k}} \sum_{o,u} \frac{|\langle \mathbf{k}_o | L_z | \mathbf{k}_u \rangle|^2 - |\langle \mathbf{k}_o | L_x | \mathbf{k}_u \rangle|^2}{\varepsilon_{\mathbf{k}_u} - \varepsilon_{\mathbf{k}_o}}. \tag{6.2}$$

where E_{MCA} is the MCA energy, ξ an average of the SOC coefficient, $\mathbf{k}_o$ and $\mathbf{k}_u$ the occupied and unoccupied states with the wave vector $\mathbf{k}$, and L_z and L_x the angular momentum operators along (001) and (100) directions, respectively. According to Eq. 6.2, the SOC between the occupied and unoccupied states with the same magnetic quantum

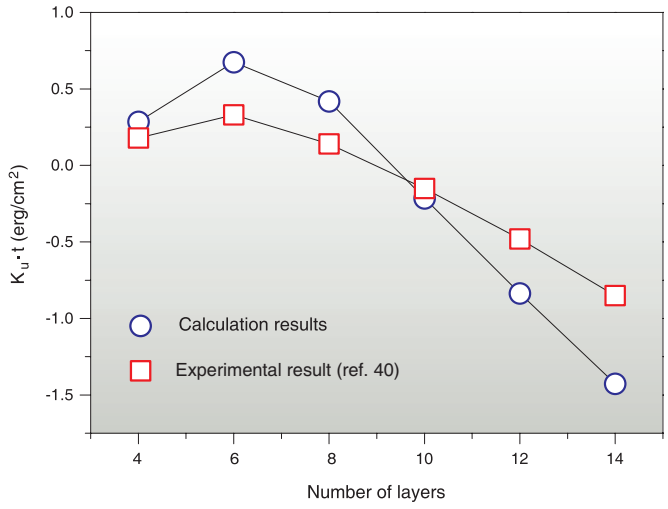

Figure 6.4: Co_2FeAl-layer thickness dependence of the interfacial MCA.

number (m) through the L_z operator enhances E_{MCA}, while that with different m through the L_x operator weakens it. Fig. 6.3 shows the local density of states (LDOSs) of interfacial Fe and O atoms. Only the majority-states are shown, since the PMA mainly originates from SOC within the majority bands around the Fermi level, while the minority bands are fully occupied and the spin-flip terms of SOC can be neglected [120, 128]. Metal-induced gap states, due to hybridization between O-p_z and Fe-e_g orbitals (d_{z^2} and $d_{x^2-y^2}$), are captured near the Fermi level. On the basis of the perturbation theory, the hybridization between the partially filled O-p_z and Fe-d_{z^2} leads to PMA since the matrix element $\langle p_z|L_z|d_{z^2}\rangle$ (positive contribution to PMA) is non-vanishing while $\langle p_z|L_z|d_{x^2-y^2}\rangle$ and $\langle p_z|L_x|d_{x^2-y^2}\rangle$ are zero.

To further verify the origin of the PMA as an interfacial effect, the CFA thickness dependence of the MCA is investigated. As illustrated in Fig. 6.4, the MCA decreases monotonically as the thickness of the CFA layers increases from 6 MLs (7.16 Å) to

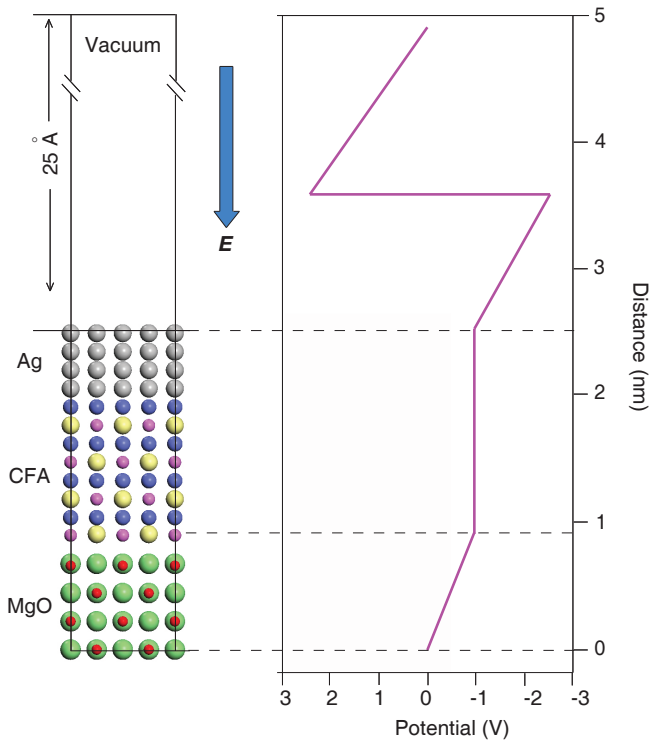

Figure 6.5: Model of the CFA/MgO supercell and the calculated layer-averaged on-site electrostatic potential under an electric field of 2 V/nm.

14 MLs (18.6 Å), while the system completely loses its PMA when the CFA layer exceeds 12 Å. Again, our calculation result shows similar trend with the experimental report.[190] This is essentially due to the intrinsic in-plane nature of MCA of the soft CFA film, which overwhelms the PMA induced by the hybridization at the interface. Thus, the possibility of the CFA bulk contribution is eliminated and the PMA merely originates from the interfacial effect as aforementioned.

6.2.3 Magnetoelectric effect: electric-field-assisted magnetization switching

We next investigate the magnetoelectric (ME) property of the CFA (1 nm)/MgO interface. Another supercell consisting of 8 MLs of CFA on top of four MLs of MgO followed by four MLs of silver (Ag) and 25 Å vacuum along the (001) direction are constructed, as shown in Fig. 6.5, with the same in-plane lattice parameter as the previous interface model. The Ag layer, which serves in experiment commonly as the buffer layer between the bottom CFA electrode and the substrate,[190, 194] is used here to eliminate the screening charge at the otherwise CFA/vacuum interface. The electric field, which points away from the CFA layer at the MgO/CFA interface Fig. 6.5, is introduced by the dipole layer method [195] with the dipole placed in the vacuum region of the supercell. The calculated layer-averaged electrostatic potential across the supercell is shown in Fig. 6.5 under an electric field of 2 V/nm. It can be found that, because of the electrostatic screening at the CFA/MgO and Ag/vacuum interfaces, no electric field exists at the CFA/Ag junction. Therefore, the anisotropy contribution of the CFA/Ag interface is irrelevant to the external electric fields, which allows us to obtain quantitatively the exact ME effect right at the CFA/MgO interface. For each given electric field E, we calculate the MCA of the MgO/CFA/Ag/Vacuum stack and subtract that of the CFA/Ag interface obtained in a separate calculation for a CFA/Ag(001) supercell.

As shown in Fig. 6.6, in absence of the electric field, the MCA energy is consistent with the aforementioned experimental results of CFA/MgO [190] and CoFe/MgO [173]. It is also close to the calculated values of CoFe/MgO [182] and Fe/MgO [128]. In presence of the electric field, the MCA energy exhibits almost linear decrease with increasing field

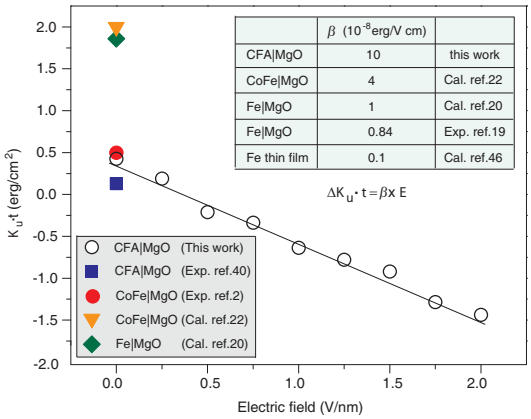

Figure 6.6: The magnetocrystalline anisotropy energy of the CFA/MgO interface ($t_{\mathrm{CFA}} = 1$ nm) as a function of the external electric field. Some experimental and calculated $K_{\mathrm{u}} \cdot t$, at $E = 0$, of CFA/MgO, CoFe/MgO and Fe/MgO are shown for comparison. The table shows the MCA coefficient (β) of various FM/MgO structures.

intensity. The interfacial MCA coefficient β is as large as 10^{-7} erg/V cm, which is one order of magnitude larger than those of CoFe/MgO [173, 182] and Fe/MgO [127, 128] and almost two orders larger than those of the Fe thin film and the Fe/metal (Pt or Ag) interface [122, 123, 196]. As discussed earlier, β is a key quantity characterizing the efficiency of electric field manipulation of MCA. Such a giant ME effect suggests the electric-field-assisted magnetization switching in the CFA/MgO/CFA p-MTJs to be more efficient than that in the well-studied CoFe(B)/MgO-based p-MTJs.[113]

To interpret the ME effect, a simple, but instructive way is to compare the variations of MCA and the orbital moment anisotropy (OMA), $\Delta M_l = M_{l(001)} - M_{l(100)}$, since both of these anisotropies originates from the spin-orbit coupling. As shown in Fig. 6.7, similar to MCA, OMA also responses linearly to the electric fields, which, in principle, only occurs when the minority d-bands are fully occupied. This indicates the magnetic

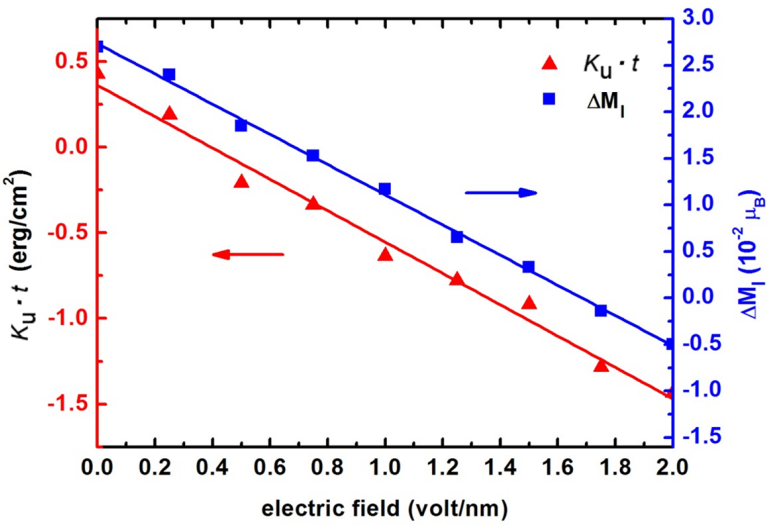

Figure 6.7: The MCA energy (red triangles) and the orbital moment anisotropy ΔM_l (blue squares) of the CFA/MgO (001) interface as a function of the external electric field.

dipole operator entries, accounting for the spin-flip excitation between the exchange-split majority and minority bands, to be vanishing in the SOC matrix. [197] Therefore, the spin-flip contribution to the MCA energy can be neglected and we can focus on the electric-field induced redistribution of majority electrons between difference d orbitals, which, in this case, is the dominant factor for the change of MCA energy.

The ME effect can be further elucidated by the electric-field-induced electron redistribution between different d orbitals. As shown in Fig. 6.8(a), the longitudinal electric field breaks the inversion symmetry along z-axis of the doubly degenerate Fe-e_g orbitals, which are consequently splitted into Fe-$d_{x^2-y^2}$ and -d_{z^2}, straddling the Fermi level and separated by 0.53 eV. Electron transfer hence takes place from the high-lying Fe-d_{z^2} orbital to the lower Fe-$d_{x^2-y^2}$ one. Figs. 6.8(b) and 6.8(c) illustrate the charge transfer by the reduced/enhanced occupation of the two orbitals. Furthermore, both

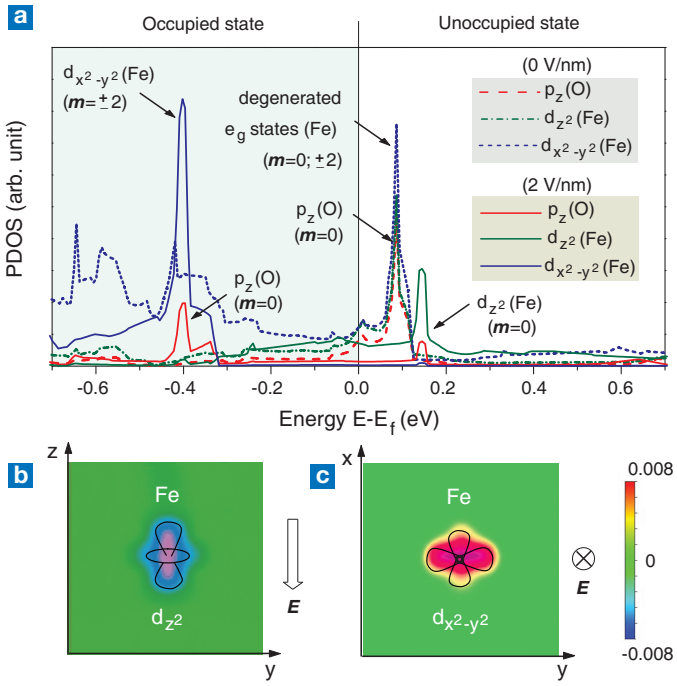

Figure 6.8: (a) Orbital-resolved LDOSs projected on the interfacial iron and oxygen atoms in absence (dashed line) and presence (solid line, $E = 2$ V/nm) of an electric field. (b) & (c) Field-induced differential electron-density, in units of e/Å^3, at the interfacial Fe atom for $E = 2$ V/nm in $y - z$ (100) and $x - y$ (001) planes, respectively.

characteristic peaks of Fe-O hybridization, i.e., $d_{x^2-y^2}$-p_z and d_{z^2}-p_z, are pushed away from the Fermi energy, with the **k** states involved in the former peak completely filled and in the latter empty. Thus, almost no available occupied/unoccupied **k**-state pairs can contribute to the matrix element $\langle p_z|L_z|d_{z^2}\rangle$ which leads to the PMA as aforementioned. This explains the reason why the PMA is destroyed under applied electric field and the MCA of the soft CFA film [186] resumes to be in-plane.

In addition, it is known that the ME effect of the FM surfaces or FM/dielectric interfaces origins from the spin-dependent screening of the electric field by the local spin-imbalanced charges.[196] Specifically, the electric-field manipulation efficiency is determined by the extent of the spin imbalance at the surface/interface, i.e., the spin polarization. [196] We will further present, in the following section, that the spin-polarization of CFA/MgO is much larger than those of the conventional FM-based interfaces due to the intrinsic half-metallicity of bulk-phase CFA. Hereby we argue that the comparatively large β value is given rise by such enhanced spin imbalance.

6.2.4 Magnetoresistance properties

The $L1_0$-FePt/MgO interface was demonstrated experimentally to possess good interfacial properties, such as large PMA ($K_u \sim 10^6 - 10^7$ erg/cm^3) and giant MCA coefficient ($\beta \sim 10^{-7}$ erg/V cm). [125] However, FePt/MgO/FePt p-MTJs show poor magnetoresistance performance in terms of both TMR ratio and ΔRA.[198] This raises the question of whether the CFA/MgO/CFA junction possesses desired spin transport properties. In this section, we investigate the MR performance of CFA/MgO/CFA p-MTJs, including interfacial spin polarization and non-collinear spin transport performance.

Interfacial spin polarization

The spin-dependent tunneling conductance of the MgO-based MTJs is determined by two factors, the symmetry matching between the transmission Bloch states in FM electrodes and evanescent states in the MgO barrier, and the spin-polarization (SP) both within the electrodes and at the electrode/barrier interfaces. [16, 89, 183, 199] As for the former factor, the spin-filter effect can be tremendously boosted if the FM electrode materials possess half-metallic Δ_1 bands, of which the Bloch states suffer from the smallest decay within the C_{4v}-symmetry MgO barrier. It has already been reported that both bulk CoFe and CFA are Δ_1-band half-metallic,[183, 186] whereas $L1_0$-FePt is not. [198] Hereby only the latter factor, i.e., the spin-polarization, is examined. We calculated and present in Fig. 6.9(a) the spin-resolved local density of states of the C-FA/MgO interface. As shown, although the SP is low at the frontier atomic layer due to the existence of interfacial states in the minority gap, it increases sharply away from the interface, jumping to 75% in the second atomic layer and recovering to 100% at 0.8 nm from the interface because of the intrinsic half-metallic nature of bulk CFA. In contrast, there is no pronounced spin-polarization shown at either CoFe or FePt interface.(Figs. 6.9(b) and 6.9(c)) In particular, the SP value is $\sim 20\%$ around 1.5 nm, which is the critical thickness of PMA,[173] away from the CoFe/MgO interface. This indicates another advantage of CFA over CoFe/FePt in sense of simultaneous existence of PMA and high SP. It should be noted that, for the spin-polarization calculation, we employed the Hubbard U correction based on the simplified Dudarev's approach[200] to take into account the strong electron-electron correlation effect within the d bands of CFA. In such approach, only the difference between the screened Coulomb (U) and exchange (J) parameters, i.e., $U_{eff} = U - J$, is meaningful. It has been justified that U_{eff}

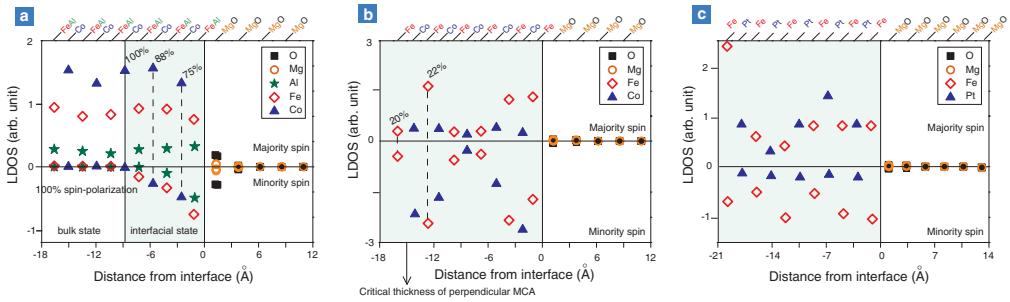

Figure 6.9: The spin-resolved LDOSs at the Fermi energy projected on each atomic sphere as a function of the distance from the (a) CFA/MgO (001), (b) CoFe/MgO (001) and (c) FePt/MgO (001) interfaces. The upper (lower) panels denote majority (minority) spin. The LDOSs of Co are doubled in (a).

values of 1.92 eV for Co and 1.80 eV for Fe give reasonable results for CFA in terms of the equilibrium volume, magnetic moments, minority band gap, etc.,[201] and were used herein. Besides, we used the Hubbard U correction on top of GGA rather than LSDA parameterization of the exchange and correlation functional. No worthy differences were observed using one or the other parameterizations.

Non-collinear spin transport

The *collinear* spin transport calculation can provide good description of MR properties of conventional MTJs. [89, 114, 183] However, the *non-collinear* spin transport method must be employed when evaluating the performance of MTJs with perpendicular magnetic easy axes. In the present study, the state-of-the-art non-collinear spin transport method was used to study the coherent transport of CFA/MgO/CFA (001) p-MTJs. The polar angles θ were set to be either 0 or π, corresponding to the two magnetization orientations of the p-MTJ electrodes. The azimuthal angles φ at all atomic sites were

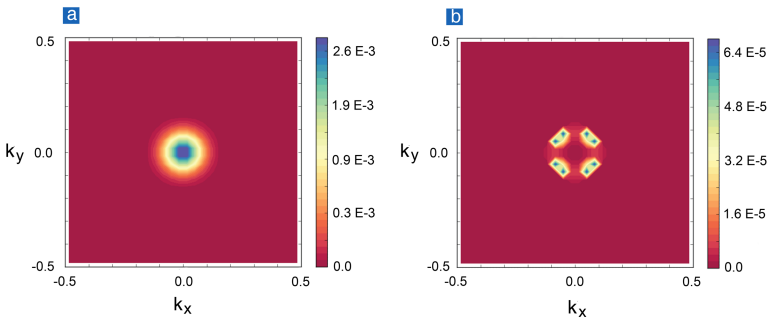

Figure 6.10: Transverse wave vector $\mathbf{k}_{//} = (k_x, k_y)$ dependent transmission spectra of the CFA/MgO/CFA p-MTJ in (a) parallel and (b) antiparallel magnetization configurations.

Table 6.1: The calculated conductance (Siemens) of the parallel (G^{P}) and antiparallel (G^{AP}) channels of the CFA/MgO/CFA, CoFe/MgO/CoFe, and FePt/MgO/FePt perpendicular magnetic tunnel junctions. The thickness of the MgO spacer is 17.1 Å for all three structures.

Structure	G^{P}	G^{AP}
CFA/MgO/CFA(collinear)	1.38×10^{-9}	3.37×10^{-14}
CFA/MgO/CFA(non-collinear)	4.42×10^{-9}	5.17×10^{-12}
CoFe/MgO/CoFe(non-collinear)	2.72×10^{-10}	6.45×10^{-12}
FePt/MgO/FePt(non-collinear)	3.23×10^{-11}	5.54×10^{-12}

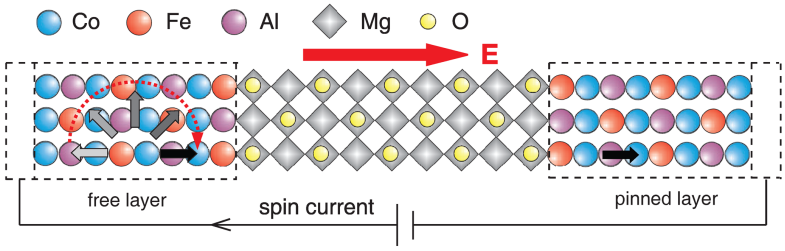

Figure 6.11: A sketch of a CFA/MgO/CFA p-MTJ and the electric-field-assisted manipulation of the magnetization configuration (AP to P).

were uniformly set to be zero since no spin-orbit coupling is considered (see Section 2.3 for detailed theoretical background of the non-collinear spin transport method). For comparison, we carried out the same calculations on the well-studied CoFe/MgO/CoFe (001) and FePt/MgO/FePt (001) junctions. The calculated conductance of these systems are listed in Table 6.1. The almost perfect antiparallel blocking in the collinear calculation is suppressed by two orders of magnitude in the non-collinear method due to the introduction of the spin-mixing terms in the density matrix . In contrast to the previous study on the interfacial spin fluctuation effect, [156] such spin-mixing does not change the nature of the antiparallel channel. As shown in Fig. 6.10, the transverse wave vector $\mathbf{k}_{//}$-resolved transmission spectrum shows a dominant hot-spot resonance tunneling feature with no Δ_1 conductance observed. The calculated TMR ratio of the CFA/MgO/CFA junction is one or two orders of magnitude larger than those of the CoFe- and FePt-based junctions.

6.3 Chapter summary

To conclude this chapter, we present a schematic sketch of the CFA/MgO/CFA p-MTJ in Fig. 6.11. The polarized current adds a spin torque on the magnetization of the free layer and switches its orientation. Due to the large interfacial MCA coefficient, the switching current density can be significantly reduced via an external electric field generated by the same applied voltage which drives the current. Such a giant ME effect, together with the high thermal stability and desired MR properties, as demonstrated in this work, makes the CFA/MgO/CFA p-MTJ an appealing building blocks of the next-generation spin-based nonvolatile memories (e.g., STT-MRAMs) with long data retention and low power consumption.

In addition, the comprehensive first-principles approach as presented herein, which combines $ab\ initio$ atomistic thermodynamics, DFT electronic structure calculation and NEGF non-collinear transport technique, can be regarded as a standard scheme to identify promising FM/oxide interfaces for p-MTJ applications.

Chapter 7

Conclusion remarks

7.1 Conclusions

In this thesis, a rather comprehensive first-principles investigation was carried out on both theoretical demonstration of microscopic mechanisms and practical establishment of general material/heterostructure design frameworks towards the next-generation magnetic data storage devices, including novel CPP-GMR read heads and non-volatile M-RAMs.

In Chapter 3, we presented an all-Heusler architecture which could be used as a rational design scheme for achieving high spin-filter efficiency in the CPP-GMR devices. A simple case study on the $Co_2CrSi/Cu_2CrAl/Co_2CrSi$ GMR stack was first performed, which provides a hint of enhanced magnetoresistance value by employing the all-Heusler structure. Then a more general calculation was carried out on a prototypical $Co_2MnSi/Ni_2NiSi/$

Co_2MnSi trilayer stack, of which the electronic structure and magnetotransport properties were systematically investigated by first-principles approaches. Well matched energy bands and Fermi surfaces between the all-Heusler electrode-spacer pair was found, which, in combination with the electrode half-metallicity, leads to larger bulk and interfacial spin-asymmetry, higher spin-filter efficiency, and consequently better magnetoresistance performance. Transport calculations further confirm the superiority of the all-Heusler architecture over the conventional Heusler/transition-metal structure by comparing their transmission coefficients and interfacial resistances of parallel conduction electrons, as well as the macroscopic current-voltage characteristics. The design scheme is significant as it suggests an alternative perspective on the selection of spacer materials, other than noble metals, for magnetoresistance enhancement. It should be noted that the all-Heusler junction based on the hypothetical $L2_1$-phased Ni_2NiSi is only a representative example of an optimum design scheme superior to the state of the art. Further theoretical and experimental efforts, following the all-Heusler scheme, are strongly recommended in designing and fabricating well-crystallized non-magnetic Heusler compounds as the tag spacer materials which can well match the Co-based full-Heusler electrodes.

In Chapter 4, we investigated the effect of crystalline symmetry on spin transport through CoFeB/MgO(thin)/CoFeB magnetic tunnel junctions.The calculated phonon spectrum showed that $Mg_3B_2O_6$ (kotoite) is the only stable structure of the spacer after annealing-driven boron diffusion. The calculated tunneling magnetoresistance (TMR) of CoFe/ kotoite/CoFe is 210%, which is in good agreement with the available experimental value and two orders of magnitude lower than the predicted values of CoFe/MgO/CoFe

junctions. This realistic TMR value can be ascribed to the reduction in crystalline symmetry from C_{4v} of MgO to C_{2v} of kotoite. Such symmetry reduction induces scattering and weakens the tunneling transmission of the Δ_1-like Bloch states. Our calculations also revealed that the tunneling transmission is sensitive to the electrode/spacer interfacial chemical bonding. Residual boron, localized at the interface due to insufficient annealing temperature, can further reduce the TMR. Our finding significantly contributes to the physical understanding of electron transport through MTJs, and specifically, the role that crystalline symmetry plays in determining the spin tunneling behavior. The Green's function based calculation is within the ballistic transport regime, and therefore, no diffusive scattering effect can be taken into consideration. But this does not undermine the physical essence of the symmetry effect we unveiled. Based on these theoretical findings, we suggest further experimental efforts in preventing both boron diffusion into the MgO spacer and residual at the electrode/spacer interface.

In Chapter 5, we focused on the application aspects of TMR, i.e., the material/ heterostructure design towards high-performance perpendicular magnetic tunnel junction (p-MTJs), the building blocks of magnetic random access memories. We evaluated the suitability of the recently emerging tetragonal Heusler compounds $Mn_{3-x}Ga$ ($0 \leq x \leq 1$) as the electrode material of p-MTJs. It was found that, despite the high spin polarization for both Mn_2Ga and Mn_3Ga , there exists considerable disparity in the spin transport performance between Mn_2Ga/MgO/Mn_2Ga(001) and Mn_3Ga/MgO/Mn_3Ga(001) MTJs: huge optimistic tunneling magnetoresistance ratio of $10^3\%$ for the former, and nevertheless, no tunneling magnetoresistance effect for the latter. Our finding is in contrast to the existing theory, but inconsistent with the preceding experimental results.

The phenomenon can be attributed to the symmetry selective filtering effect of the MgO spacer, in other words, the Bloch-state matching at $Mn_{3-x}Ga$/MgO interfaces. On this premise, we provide a insightful perspective on distinguishing good $Mn_{3-x}Ga$ compounds from the bad ones. $Mn_{3-x}Ga$ with lower Mn concentration is, in principle, suggested as promising candidate materials to serve as the p-MTJ electrodes, and deserves future experimental demonstration.

From a broader view, good p-MTJs must simultaneously satisfy the requirements of high thermal stability, low power consumption and good spin transport performance. To address these challenges, in Chapter 6, we proposed another family of materials, the cobalt-based full-Heusler compounds, to be used as the p-MTJ electrodes, in junction with the MgO spacer. The well-studied Co_2FeAl was chosen as a representative example of the family in view of its small intrinsic damping constant ($\alpha_{Co_2FeAl} \approx 0.001$), small lattice mismatch with MgO (3.7%), and half-metallicity. We first examined the thermal stability of the CFA/MgO interface by mapping out a thermodynamic phase diagram in terms of chemical potential under ambient condition. It was found that O-top FeAl termination is the only stable interfacial structure of CFA/MgO. In addition to geometric stability, a rather strong PMA, with an interfacial MCA energy (Kut) of 0.428 erg/cm^2, was found, which can compete with thermal fluctuation and enhance the robustness of the magnetic configuration. Second, the CFA/MgO interface manifested giant ME efficiency due to its high interfacial spin imbalance. The calculated anisotropy energy coefficient was around 10^{-7} erg/V cm, one order of magnitude higher than the state of the art. The efficient electric-field control of magnetization is considered desirable in view of power saving. Finally, non-collinear spin transport calculations demonstrated superior magnetotransport performance (larger MR ratio) of the CFA/MgO/CFA p-MTJ over

its conventional CoFe- or FePt-based counterparts. The combination of high thermal stability, low power consumption, and enhanced MR ratio as demonstrated in the present work provides a new framework for designing Heusler-compound-based building blocks towards the next-generation non-volatile memories. Further experimental work is highly recommended, following our theoretical framework, to fabricate and characterize the the CFA/MgO/CFA p-MTJs.

Bibliography

[1] http://www.emc.com/leadership/programs/digital-universe.htm.

[2] http://www.statisticbrain.com/average-cost-of-hard-drive-storage.

[3] M. N. Baibich, J. M. Broto, A. Fert, F. N. Van Dau, F. Petro, P. Etienne, G. Creuzet, A. Friederich and J. Chazelas, Phys. Rev. Lett. **61**, 2472 (1988).

[4] G. Binasch, P. Grunberg, F. Saurenbach and W. Zinn, Phys. Rev. B **39**, 4828 (1989).

[5] A. Fert, Rev. Mod. Phys. **80**, 1517 (2008).

[6] C. Chappert, A. Fert and F. N. Van Dau, Nat. Mater. **6**, 813 (2007).

[7] S. S. P. Parkin, N. More and K. P. Roche, Phys. Rev. Lett. **64**, 2304 (1990).

[8] D. H. Mosca, F. Petro, A. Fert, P. A. Schroeder, W. P. Pratt Jr and R. Laloee, J. Magn. Magn. Mater. **94**, L1 (1991).

[9] S. S. P. Parkin, R. Bhadra and K. P. Roche, Phys. Rev. Lett. **66**, 2152 (1991).

[10] B. Dieny, V. S. Speriosu, S. S. P. Parkin, B. A. Gurney, D. R. Wilhoit and D. Mauri, Phys. Rev. B **43**, 1297 (1991).

[11] T. Valet and A. Fert, Phys. Rev. B **48**, 7099 (1993).

[12] M. Takagishi, K. Koi, M. Yoshikawa, T. Funayama, H. Iwasaki and M. Sahashi, IEEE Trans. Magn. **38**, 2277 (2002).

[13] M. Julliere, Phys. Lett. A **54**, 225 (1975).

[14] T. Miyazaki and N. Tezuka, J. Magn. Magn. Mater. **139**, L231 (1995).

[15] J. S. Moodera, L. R. Kinder, T. M. Wong and R. Meservey, Phys. Rev. Lett. **74**, 3273 (1995).

[16] W. H. Butler, X. G. Zhang, T. C. Schulthess and J. M. MacLaren, Phys. Rev. B **63**, 054416 (2001).

[17] J. Mathon and A. Umerski, Phys. Rev. B **63**, 220403 (2001).

[18] X. G. Zhang and W. H. Butler, Phys. Rev. B **70**, 172407 (2004).

[19] S. S. P. Parkin, C. Kaiser, A. Panchula, P. M. Rice, B. Hughes, M. Samant and S.-H. Yang, Nat. Mater. **3**, 862 (2004).

[20] S. Yuasa, T. Nagahama, A. Fukushima, Y. Suzuki and K. Ando, Nat. Mater. **3**, 868 (2004).

[21] S. Ikeda, J. Hayakawa, Y. Ashizawa, Y. M. Lee, K. Miura, H. Hasegawa, M. Tsunoda, F. Matsukura and H. Ohno, Appl. Phys. Lett. **93**, 082508 (2008).

[22] J. M. Daughton, J. Appl. Phys. **81**, 3758 (1997).

[23] J. AŁkerman, Science **308**, 508 (2005).

[24] M. Durlam, D. Addie, J. Akerman, B. Butcher, P. Brown, J. Chan, M. DeHerrera, B. N. Engel, B. Feil, G. Grynkewich, J. Janesky, M. Johnson, K. Kyler, J. Molla,

J. Martin, K. Nagel, J. Ren, N. D. Rizzo, T. Rodriguez, L. Savtchenko, J. Salter, J. M. Slaughter, K. Smith, J. J. Sun, M. Lien, K. Pap- worth, P. Shah, W. Qin, R. Williams, L. Wise and S. Tehrani, presented at the Electron Devices Meeting, 2003. IEDM '03 Technical Digest. IEEE International, 2003 (unpublished).

[25] B. N. Engel, J. Akerman, B. Butcher, R. W. Dave, M. DeHerrera, M. Durlam, G. Grynkewich, J. Janesky, S. V. Pietambaram, N. D. Rizzo, J. M. Slaughter, K. Smith, J. J. Sun and S. Tehrani, IEEE Trans. Magn. **41**, 132 (2005).

[26] J. A. Katine and E. E. Fullerton, J. Magn. Magn. Mater. **320**, 1217 (2008).

[27] L. Berger, Phys. Rev. B **54**, 9353 (1996).

[28] J. C. Slonczewski, J. Magn. Magn. Mater. **159**, L1(1996).

[29] M. Tsoi, A. G. M. Jansen, J. Bass, W. C. Chiang, M. Seck, V. Tsoi and P. Wyder, Phys. Rev. Lett. **80**, 4281 (1998).

[30] F. J. Albert, J. A. Katine, R. A. Buhrman and D. C. Ralph, Appl. Phys. Lett. **77**, 3809 (2000).

[31] J. A. Katine, F. J. Albert, R. A. Buhrman, E. B. Myers and D. C. Ralph, Phys. Rev. Lett. **84**, 3149 (2000).

[32] E. B. Myers, D. C. Ralph, J. A. Katine, R. N. Louie and R. A. Buhrman, Science **285**, 867 (1999).

[33] J. Z. Sun, Phys. Rev. B **62**, 570 (2000).

[34] J. C. Slonczewski, Phys. Rev. B **71**, 024411 (2005).

[35] E. Chen, D. Apalkov, Z. Diao, A. Driskill-Smith, D. Druist, D. Lottis, V. Nikitin, X. Tang, S. Watts, S. Wang, S. A. Wolf, A. W. Ghosh, J. W. Lu, S. J. Poon, M. Stan, W. H. Butler, S. Gupta, C. K. A. Mewes, T. Mewes and P. B. Visscher, IEEE Trans. Magn. **46**, 1873 (2010).

[36] T. Kawahara, K. Ito, R. Takemura and H. Ohno, Microelectron. Reliab. **52**, 613 (2012).

[37] C. Felser, G. H. Fecher and B. Balke, Angew. Chem. Int. Ed. **46**, 668 (2007).

[38] R. A. de Groot, F. M. Mueller, P. G. V. Engen and K. H. J. Buschow, Phys. Rev. Lett. **50**, 2024 (1983)

[39] W. S. F. Heusler and E. Haupt, Verh. DPG **5** (1903).

[40] F. Heusler, Verh. DPG **5**, 219 (1903).

[41] T. Graf, C. Felser and S. S. P. Parkin, Progr. Solid State Chem. **39**, 1 (2011).

[42] T. Graf, S. S. P. Parkin and C. Felser, IEEE Trans. Magn. **47**, 367 (2011).

[43] J. Kubler, A. R. William and C. B. Sommers, Phys. Rev. B **28**, 1745 (1983).

[44] S. Wurmehl, H. C. Kandpal, G. H. Fecher and C. Felser, J. Phys.: Condens. Matter **18**, 6171 (2006).

[45] J. Pierre, R. Skolozdra, J. Tobola, S. Kaprzyk, C. Hordequin, M. A. Kouacou, I. Karla, R. Currat and E. Lelievre-Berna, J. Alloy. Compd. **262**, 101 (1997).

[46] D. Jung, H. J. Koo and M. H. Whangbo, J. Mol. Struct. (THEOCHEM) **527**, 113 (2000).

[47] J. Winterlik, G. H. Fecher, A. Thomas and C. Felser, Phys. Rev. B **79**, 064508 (2009).

[48] W. Al-Sawai, H. Lin, R. S. Markiewicz, L. A. Wray, Y. Xia, S. Y. Xu, M. Z. Hasan and A. Bansil, Phys. Rev. B **82**, 125208 (2010).

[49] S. Chadov, X. L. Qi, J. Kubler, G. H. Fecher, C. Felser and S. C. Zhang, Nat. Mater. **9**, 541 (2010).

[50] W. Feng, D. Xiao, Y. Zhang and Y. Yao, Phys. Rev. B **82**, 235121 (2010).

[51] H. Lin,L. A. Wray,Y. Q. Xia,S. Y. Xu,S. A. Jia, R. J. Cava, A. Bansil and M. Z. Hasan, Nat. Mater. **9**, 546 (2010).

[52] D. Xiao, Y. Yao, W. Feng, J. Wen, W. Zhu, X.-Q. Chen, G. M. Stocks and Z. Zhang, Phys. Rev. Lett. **105**, 096404 (2010).

[53] Z. Bai, L. Shen, G. Han, and Y. P. Feng, SPIN **2**, 1230006 (2013).

[54] K. E. H. M. Hanssen and P. E. Mijnarends, Phys. Rev. B **34**, 5009 (1986).

[55] K. E. H. M. Hanssen, P. E. Mijnarends, L. P. L. M. Rabou and K. H. J. Buschow, Phys. Rev. B **42**, 1533 (1990).

[56] C. T. Tanaka, J. Nowak and J. S. Moodera, J. Appl. Phys. **86**, 6239 (1999).

[57] S. J. Jenkins, Phys. Rev. B **70**, 245401 (2004).

[58] M. C. Kautzky, F. B. Mancoff, J. F. Bobo, P. R. Johnson, R. L. White and B. M. Clemens, J. Appl. Phys. **81**, 4026 (1997).

[59] P. R. Johnson, M. C. Kautzky, F. B. Mancoff, R. Kondo, B. M. Clemens and R. L. White, IEEE Trans. Magn. **32**, 4615 (1996).

[60] S. Ishida, S. Fujii, S. Kashiwagi and S. Asano,J. Phys. Soc. Jpn. **64**, 2152 (1995).

[61] W. E. Pickett and J. S. Moodera, Phys. Today **54**, 39 (2001).

[62] I. Galanakis, P. H. Dederichs and N. Papanikolaou, Phys. Rev. B **66**, 174429 (2002).

[63] S. Picozzi, A. Continenza and A. J. Freeman, Phys. Rev. B **66**, 094421 (2002).

[64] N. Auth, G. Jakob, T. Block and C. Felser, Phys. Rev. B **68**, 024403 (2003).

[65] T. Block, C. Felser, G. Jakob, J. Ensling, B. Muhling, P. Gutlich and R. J. Cava, J. Solid State Chem. **176**, 646 (2003).

[66] C. Felser, B. Heitkamp, F. Kronast, D. Schmitz, S. Cramm, H. A. Durr, H. J. Elmers, G. H. Fecher, S. Wurmehl, T. Block, D. Valdaitsev, S. A. Nepijko, A. Gloskovskii, G. Jakob, G. Schonhense and W. Eberhardt, J. Phys.: Condens. Matter **15**, 7019 (2003).

[67] K. Inomata, S. Okamura, R. Goto and N. Tezuka, Jpn. J. Appl. Phys. **42**, L419 (2003).

[68] K. Inomata, N. Ikeda, N. Tezuka, R. Goto, S. Sugimoto, M. Wojcik and E. Jedryka, Sci. Tech. Adv. Mater. **9**, 014101 (2008).

[69] T. M. Nakatani, N. Hase, H. S. Goripati, Y. K. Takahashi, T. Furubayashi and K. Hono, IEEE Trans. Magn. **48**, 1751 (2012).

[70] T. Kubota, Y. Miura, D. Watanabe, S. Mizukami, F. Wu, H. Naganuma, X. M. Zhang, M. Oogane, M. Shirai, Y. Ando and T. Miyazaki, Appl. Phys. Exp. **4**, 043002 (2011).

[71] V. Ko, G. Han, J. Qiu and Y. P. Feng, Appl. Phys. Lett. **95**, 202502 (2009).

[72] K. Nikolaev, P. Kolbo, T. Pokhil, X. Peng, Y. Chen, T. Ambrose and O. Mryasov, Appl. Phys. Lett. **94**, 222501 (2009).

[73] V. Ko, G. Han and Y. P. Feng, J. Magn. Magn. Mater. **322**, 2989 (2010).

[74] Z. Q. Bai,Y. H. Lu,L. Shen,V. Ko,G. C. Han and Y. P. Feng, J. Appl. Phys. **111**, 093911 (2012).

[75] T. Furubayashi, K. Kodama, H. Sukegawa, Y. K. Takahashi, K. Inomata and K. Hono, Appl. Phys. Lett. **93**, 122507 (2008).

[76] T. M. Nakatani, T. Furubayashi, S. Kasai, H. Sukegawa, Y. K. Takahashi, S. Mitani and K. Hono, Appl. Phys. Lett. **96**, 212501 (2010).

[77] T. M. Nakatani, S. Mitani, T. Furubayashi and K. Hono, Appl. Phys. Lett. **99**, 182505 (2011).

[78] T. Iwase, Y. Sakuraba, S. Bosu, K. Saito, S. Mitani and K. Takanashi, Appl. Phys. Exp. **2**, 063003 (2009).

[79] Y. Sakuraba, K. Izumi, T. Iwase, S. Bosu, K. Saito, K. Takanashi, Y. Miura, K. Futatsukawa, K. Abe and M. Shirai, Phys. Rev. B **82**, 094444 (2010).

[80] N. Hase, T. M. Nakatani, S. Kasai, Y. K. Takaha- shi, T. Furubayashi and K. Hono, J. Magn. Magn. Mater. **324**, 440 (2012).

[81] N. Hase, B. Varaprasad, T. M. Nakatani, H. Sukegawa, S. Kasai, Y. K. Takahashi, T. Fur- ubayashi and K. Hono, J. Appl. Phys. **108**, 093916 (2010).

[82] Y. K. Takahashi, A. Srinivasan, B. Varaprasad, A. Rajanikanth, N. Hase, T. M. Nakatani, S. Kasai, T. Furubayashi and K. Hono, Appl. Phys. Lett. **98**, 152501 (2011).

[83] J. Sato, M. Oogane, H. Naganuma and Y. Ando, Appl. Phys. Exp. **4**, 043002 (2011).

[84] T. Ambrose and O. Mryasov, U.S. patent 6,876,522 (2005).

[85] S. Chadov, T. Graf, K. Chadova, X. Dai, F. Casper, G. H. Fecher, and C. Felser, Phys. Rev. Lett. **107**, 047202 (2011).

[86] V. Ko, J. Qiu, P. Luo, G. C. Han, and Y. P. Feng, J. Appl. Phys. **109**, 07B103 (2011).

[87] D. Waldron, V. Timoshevskii, Y. Hu, K. Xia, and H. Guo, Phys. Rev. Lett. **97**, 226802 (2006).

[88] Y. Ke, K. Xia, and H. Guo, Phys. Rev. Lett. **100**, 166805 (2008).

[89] Y. Ke, K. Xia, and H. Guo, Phys. Rev. Lett. **105**, 236801 (2010).

[90] J. P. Velev, K. D. Belashchenko, and E. Y. Tsymbal, Phys. Rev. Lett. **96**, 119601 (2006).

[91] K. D. Belashchenko, J. Velev, and E. Y. Tsymbal, Phys. Rev. B **72**, 140404(R) (2005).

[92] H. L. Meyerheim, R. Popescu, J. Kirschner, N. Jedrecy, M. Sauvage- Simkin, B. Heinrich, and R. Pinchaux, Phys. Rev. Lett. **87**, 076102 (2001).

[93] X.-G. Zhang, W. H. Butler, and A. Bandyopadhyay, Phys. Rev. B **68**, 092402 (2003).

[94] J. Velev, K. Belashchenko, S. Jaswal, and E. Tsymbal, Appl. Phys. Lett. **90**, 072502 (2007).

[95] D. D. Djayaprawira, K. Tsunekawa, M. Nagai, H. Maehara, S. Yamagata, N. Watanabe, S. Yuasa, Y. Suzuki, and K. Ando, Appl. Phys. Lett. **86**, 092502 (2005).

[96] Y. M. Lee, J. Hayakawa, S. Ikeda, F. Matsukura, and H. Ohno, Appl. Phys. Lett. **90**, 212507 (2007).

[97] J. J. Cha, J. C. Read, W. F. Egelhoff, P. Y. Huang, H.-W. Tseng, Y. Li, R. A. Buhrman, and D. A. Muller, Appl. Phys. Lett. **95**, 023506 (2009).

[98] H. Kurt, K. Rode, K. Oguz, M. Boese, C. C. Faulkner, and J. M. D. Coey, Appl. Phys. Lett. **96**, 262501 (2010).

[99] A. K. Rumaiz, J. C. Woicik, W. G. Wang, J. Jordan-Sweet, G. H. Jaffari, C. Ni, J. Q. Xiao, and C. L. Chien, Appl. Phys. Lett. **96**, 112502 (2010).

[100] Y. Lu, B. Lepine, G. Jezequel, S. Ababou, M. Alnot, J. Lambert, A. Renard, M. Mullet, C. Deranlot, H. Jaffres, F. Petroff, and J.-M. George, J. Appl. Phys. **108**, 043703 (2010).

[101] R. Sbiaa, H. Meng and S. N. Piramanayagam, Phys. Status Solidi-Rapid Res. Lett. **5**, 413 (2011).

[102] N. Nishimura, T. Hirai, A. Koganei, T. Ikeda, K. Okano, Y. Sekiguchi and Y. Osada, J. Appl. Phys. **91**, 5246 (2002).

[103] O. Redon, B. Dieny and B. Rodmacq, U.S. Patent No. 6532164 B2, 3 November 2003.

[104] A. D. Kent, B. Ozyilmaz and E. del Barco, Appl. Phys. Lett. **84**, 3897 (2004).

[105] K. J. Lee, O. Redon and B. Dieny, Appl. Phys. Lett. **86**, 022505 (2005).

[106] L. Liu, T. Moriyama, D. C. Ralph and R. A. Buhrman, Appl. Phys. Lett. **94**, 122508 (2009).

[107] T. Moriyama, T. J. Gudmundsen, P. Y. Huang, L. Liu, D. A. Muller, D. C. Ralph and R. A. Buhrman, Appl. Phys. Lett. **97**, 072513 (2010).

[108] P. K. Amiri, Z. M. Zeng, J. Langer, H. Zhao, G. Rowlands, Y. J. Chen, I. N. Krivorotov, J. P. Wang, H. W. Jiang, J. A. Katine, Y. Huai, K. Galatsis and K. L. Wang, Appl. Phys. Lett. **98**, 112507 (2011).

[109] M. T. Rahman, A. Lyle, P. K. Amiri, J. Harms, B. Glass, H. Zhao, G. Rowlands, J. A. Katine, J. Langer, I. N. Krivorotov, K. L. Wang and J. P. Wang, J. Appl. Phys. **111**, 07C907 (2012).

[110] B. Balke, G. H. Fecher, J. Winterlik, and C. Felser, Appl. Phys. Lett. **90**, 152504 (2007).

[111] J. Winterlik, B. Balke, G. H. Fecher, C. Felser, M. C. M. Alves, F. Bernardi, and J. Morais, Phys. Rev. B **77**, 054406 (2008).

[112] H. Kurt, K. Rode, M. Venkatesan, P. Stamenov, and J. M. D. Coey, Phys. Rev. B **83**, 020405(R) (2011).

[113] W.-G. Wang, M. Li, S. Hageman, and C. Chien, Nat. Mater. **11**, 64 (2012).

[114] J. D. Burton and E. Y. Tsymbal, Phys. Rev. Lett. **106**, 157203 (2011).

[115] N. M. Caffrey, T. Archer, I. Rungger, and S. Sanvito, Phys. Rev. Lett. **109**, 226803 (2012).

[116] N. M. Caffrey, T. Archer, I. Rungger, and S. Sanvito, Phys. Rev. B **83**, 125409 (2011).

[117] J. Hu and R. Q. Wu, Phys. Rev. Lett. **110**, 097202 (2013).

[118] N. N. Negulyaev, V. S. Stepanyuk, W. Hergert, and J. Kirschner, Phys. Rev. Lett. **106**, 037202 (2011).

[119] T. R. Dasa, P. A. Ignatiev, and V. S. Stepanyuk, Phys. Rev. B **85**, 205447 (2012).

[120] P. Ruiz-Diaz, T. R. Dasa, and V. S. Stepanyuk, Phys. Rev. Lett. **110**, 267203 (2013).

[121] C.-G. Duan, S. S. Jaswal, and E. Y. Tsymbal, Phys. Rev. Lett. **97**, 047201 (2006).

[122] K. Nakamura, R. Shimabukuro, Y. Fujiwara, T. Akiyama, T. Ito, and A. Freeman, Phys. Rev. Lett. **102**, 187201 (2009).

[123] M. Tsujikawa and T. Oda, Phys. Rev. Lett. **102**, 247203 (2009).

[124] M. Tsujikawa, A. Hosokawa, and T. Oda, Phys. Rev. B **77**, 054413 (2008).

[125] M. Weisheit, S. F ahler, A. Marty, Y. Souche, C. Poinsignon, and D. Givord, Science **315**, 349 (2007).

[126] W. Zhu, Y. Liu, and C.-G. Duan, Appl. Phys. Lett. **99**, 032508 (2011).

[127] T. Maruyama, Y. Shiota, T. Nozaki, K. Ohta, N. Toda, M. Mizuguchi, A. Tulapurkar, T. Shinjo, M. Shiraishi, S. Mizukami, Y. Ando, and Y. Suzuki, Nat. Nanotechnol. **4**, 158 (2009).

[128] M. K. Niranjan, C.-G. Duan, S. S. Jaswal, and E. Y. Tsymbal, Appl. Phys. Lett. **96**, 222504 (2010).

[129] G. Kresse and J. Furthmuller, Phys. Rev. B **54**, 11169 (1996).

[130] G. Kresse and J. Furthmuller, Com. Mater. Sci. **6**, 15 (1996).

[131] J. Taylor, H. Guo, and J. Wang, Phys. Rev. B **63**, 121104 (2001).

[132] J. Kurti, C. Magyar, A. Balazs, and P. Rajczy, Synthetic. Met. **71**, 1865 (1995).

[133] W. Kohn and L. J. Sham. Phys, Rev. **140**, A1133 (1965).

[134] J. P. Perdew and Y. Wang, Phys. Rev. B **45**, 13244 (1992).

[135] J. P. Perdew, K. Burke, and M. Ernzerhof, Phys. Rev. Lett. **77**, 3865 (1996).

[136] J. P. Perdew, K. Burke, and M. Ernzerhof, Phys. Rev. Lett. **78**, 1396 (1997).

[137] D. J. Chadi and M. L. Cohen, Phys. Rev. B **8**, 5747 (1973).

[138] H. J. Monkhorst and J. D. Pack, Phys. Rev. B **13**, 5188 (1976).

[139] J. C. Phillips, Phys. Rev. **112**, 685 (1958).

[140] M. L. Cohen and V. Heine, Solid State Phys. **24**, 37 (1970).

[141] M. T. Yin and M. L. Cohen, Phys. Rev. B **25**, 7403 (1982).

[142] D. Vanderbilt, Phys. Rev. B **41**, 7892 (1990).

[143] P. E. Bl*ö*chl, Phys. Rev. B **50**, 17953 (1994).

[144] G. Kresse and J. Joubert, Phys. Rev. B **59**, 1758 (1999).

[145] G. Kresse and J. Hafner, Phys. Rev. B **47**, 558 (1993); Phys. Rev. B **48**, 131115 (1994).

[146] J. Kubler, K. H. Hock, J. Sticht, and A. R. Williams, Journal of Physics F: Metal Physics **18**, 469 (1988).

[147] T. Oda, A. Pasquarello, and R. Car, Phys. Rev. Lett. **80**, 3622 (1998).

[148] K. Nakamura, T. Ito, A. J. Freeman, L. Zhong, and J. Fernandez-de Castro, Phys. Rev. B **67**, 014420 (2003).

[149] V. M. Garcia-Suarez, C. M. Newman, C. J. Lambert, J. M. Pruneda, and J. Ferrer, Journal of Physics: Condensed Matter **16**, 5453 (2004).

[150] K. Knopfle, L. M. Sandratskii, and J. Kubler, Phys. Rev. B **62**, 5564 (2000).

[151] K. Nagasaka, J. Magn. Magn. Mater. **321**, 508 (2009).

[152] M. Takagishi, K. Yamada, H. Iwasaki, H. N. Fuke, and S. Hashimoto, IEEE Trans. Magn. **46**, 2086 (2010).

[153] M. Covington, M. AlHajDarwish, Y. Ding, N. J. Gokemeijer, and M. A. Seigler, Phys. Rev. B **69**, 184406 (2004).

[154] J. R. Childress, M. J. Carey, S. I. Kiselev, J. A. Katine, S. Maat, and N. Smith, J. Appl. Phys. **99**, 08S305 (2006).

[155] Y. Sakuraba, K. Izumi, T. Iwase, S. Bosu, K. Saito, K. Takanashi, Y. Miura, K. Futatsukawa, K. Abe, and M. Shirai, Phys. Rev. B **82**, 094444 (2010).

[156] Y. Miura, K. Futatsukawa, S. Nakajima, K. Abe, and M. Shirai, Phys. Rev. B **84**, 134432 (2011).

[157] Z. Bai, Y. Cai, L. Shen, M. Yang, V. Ko, G. Han, and Y. Feng, Appl. Phys. Lett. **100**, 022408 (2012).

[158] T. Harada, I. Ohkubo, M. Lippmaa, Y. Sakurai, Y. Matsumoto, S. Muto, H. Koinuma, and M. Oshima, Phys. Rev. Lett. **109**, 076602 (2012).

[159] K. Xia, M. Zwierzycki, M. Talanana, P. J. Kelly, and G. E. W. Bauer, Phys. Rev. B **73**, 064420 (2006).

[160] S. A. Rishton, Y. Lu, R. A. Altman, A. C. Marley, X. P. Bian, C. Jahnes, R. Viswanathan, G. Xiao, W. J. Gallagher, and S. S. P. Parkin, Microelectron. Eng. **35**, 249 (1997).

[161] Z. W. Tan, J.-S. Wang, and C. K. Gan, Nano Lett. **11**, 214 (2011).

[162] L. Shen, T. Zhou, Z. Bai, M. Zeng, J. Q. Goh, Z.-M. Yuan, G. Han, B. Liu, and Y. P. Feng, Phys. Rev. B **85**, 064105 (2012).

[163] L. Shen, M. Zeng, S. Li, M. B. Sullivan, and Y. P. Feng, Phys. Rev. B **86**, 115419 (2012).

[164] L. Shen, M. Zeng, S.-W. Yang, C. Zhang, X. F. Wang, and Y. P. Feng, J. Am. Chem. Soc. **132**, 11481 (2010).

[165] Y. Z. Liu, A. N. Chiaramonti, D. K. Schreiber, H. Yang, S. S. P. Parkin, O. G. Heinonen, and A. K. Petford-Long, Phys. Rev. B **83**, 165413 (2011).

[166] J. Y. Bae, W. C. Lim, H. J. Kim, T. D. Lee, K. W. Kim, and T. W. Kim, J. Appl. Phys. **99**, 08T316 (2006).

[167] J. C. Read, J. J. Cha, W. F. Egelhoff, H. W. Tseng, P. Y. Huang, Y. Li, D. A. Muller, and R. A. Buhrman, Appl. Phys. Lett. **94**, 112504 (2009).

[168] D. A. Stewart, Nano Lett. **10**, 263 (2010).

[169] J. D. Burton, S. S. Jaswal, E. Y. Tsymbal, O. N. Mryasov, and O. G. Heinonen, Appl. Phys. Lett. **89**, 142507 (2006).

[170] Q. L. Ma, T. Kubota, S. Mizukami, X. M. Zhang, H. Naganuma, M. Oogane, Y. Ando, and T. Miyazaki, Appl. Phys. Lett. **101**, 032402 (2012).

[171] J. Winterlik, S. Chadov, A. Gupta, V. Alijani, T. Gasi, K. Filsinger, B. Balke, G. Fecher, C. Jenkins, F. Casper, J. Kubler, G.-D. Liu, L. Gao, S. S. P. Parkin, and C. Felser, Adv. Mater. **24**, 6283 (2012).

[172] A. Brataas, A. D. Kent, and H. Ohno, Nat. Mater. **11**, 372 (2012).

[173] S. Ikeda, K. Miura, H. Yamamoto, K. Mizunuma, H. Gan, M. Endo, S. Kanai, J. Hayakawa, F. Matsukura, and H. Ohno, Nat. Mater. **9**, 721 (2010).

[174] A. Lehnert, S. Dennler, P. Blonski, S. Rusponi, M. Etzkorn, G. Moulas, P. Bencok, P. Gambardella, H. Brune, and J. Hafner, Phys. Rev. B **82**, 094409 (2010).

[175] J. Dorantes-Davila, H. Dreysse, and G. M. Pastor, Phys. Rev. Lett. **91**, 197206 (2003).

[176] A. Alkauskas, P. Broqvist, F. Devynck, and A. Pasquarello, Phys. Rev. Lett. **101**, 106802 (2008).

[177] O. Wunnicke, N. Papanikolaou, R. Zeller, and P. H. Dederichs, Phys. Rev. B **65**, 064425 (2002).

[178] Y. Miura, H. Uchida, Y. Oba, K. Abe, and M. Shirai, Phys. Rev. B **78**, 064416 (2008).

[179] V. Heine, Proc. Phys. Soc. London **81**, 300 (1962); Surf. Sci. **2**, 1 (1964); Phys. Rev. **138**, A1689 (1965).

[180] P. Mavropoulos, N. Papanikolaou, and P. H. Dederichs, Phys. Rev. Lett. **85**, 1088 (2000).

[181] K. Nakamura, T. Akiyama, T. Ito, M. Weinert, and A. Freeman, Phys. Rev. B **81**, 220409 (2010).

[182] K. He, J. Chen, and Y. Feng, Appl. Phys. Lett. **99**, 072503 (2011).

[183] Z. Bai, L. Shen, Q. Wu, M. Zeng, J.-S. Wang, G. Han, and Y. P. Feng, Phys. Rev. B **87**, 014114 (2013).

[184] B. Hulsen, M. Scheffler, and P. Kratzer, Phys. Rev. Lett. **103**, 046802 (2009).

[185] S. J. Hashemifar, P. Kratzer, and M. Scheffler, Phys. Rev. Lett. **94**, 096402 (2005).

[186] W. Wang, E. Liu, M. Kodzuka, H. Sukegawa, M. Wojcik, E. Jedryka, G. Wu, K. Inomata, S. Mitani, and K. Hono, Phys. Rev. B **81**, 140402 (2010).

[187] C. M. Weinert and M. Scheffler, Phys. Rev. Lett. **58**, 1456 (1987).

[188] M. Scheffler and J. Dabrowski, Philosophical Magazine A **58**, 107 (1988).

[189] S. Ikeda, J. Hayakawa, Y. M. Lee, F. Matsukura, Y. Ohno, T. Hanyu, and H. Ohno, IEEE T. Eletron Dev. **54**, 991 (2007).

[190] Z. Wen, H. Sukegawa, S. Mitani, and K. Inomata, Appl. Phys. Lett. **98**, 242507 (2011).

[191] D.-S. Wang, R. Q. Wu, and A. J. Freeman, Phys. Rev. B **47**, 14932 (1993).

[192] K. Hotta, K. Nakamura, T. Akiyama, T. Ito, T. Oguchi, and A. J. Freeman, Phys. Rev. Lett. **110**, 267206 (2013).

[193] L. Shen, T. Zhou, R. Q. Wee, K. M. Cher, H. Y. Y. Ko, R. Niu, H. Gong, Z. Yuan, B. Liu, and Y. P. Feng, Adv. Mater. **25**, 1639 (2013).

[194] Z. Wen, H. Sukegawa, S. Kasai, M. Hayashi, S. Mitani, and K. Inomata, Appl Phys Express **5**, 3003 (2012).

[195] J. Neugebauer and M. Scheffler, Phys. Rev. B **46**, 16067 (1992).

[196] C. G. Duan, J. P. Velev, R. F. Sabirianov, Z. Zhu, J. Chu, S. S. Jaswal, and E. Y. Tsymbal, Phys. Rev. Lett. **101**, 137201 (2008).

[197] G. van der Laan, Journal of Physics: Condensed Matter **10**, 3239 (1998).

[198] Y. Taniguchi, Y. Miura, K. Abe, and M. Shirai, IEEE T. Magn. **44**, 2585 (2008).

[199] J. D. Burton and E. Y. Tsymbal, Phys. Rev. Lett. **107**, 166601 (2011).

[200] S. L. Dudarev, G. A. Botton, S. Y. Savrasov, C. J. Humphreys, and A. P. Sutton, Phys. Rev. B **57**, 1505 (1998).

[201] H. C. Kandpal, G. H. Fecher, and C. Felser, Journal of Physics D: Applied Physics **40**, 1507 (2007).

Theoretical Understanding and Material Design towards Next-generation Data Storage Devices

ZHAOQIANG BAI

NATIONAL UNIVERSITY OF SINGAPORE

2014